Numerical Study of a Fluidic Precessing Jet Flow

Xiao Chen

School of Mechanical Engineering

Faculty of Engineering, Mathematical and Computer Sciences

The University of Adelaide, Australia

A thesis submitted for the degree of Doctor of Philosophy in 2017.

Contents

Abstract

This thesis reports the structure of turbulent, unsteady, fluidic precessing jet (FPJ) flow within a suddenly expanding axisymmetric chamber and the mode switching phenomenon using finite volume Computational Fluid Dynamics (CFD) method. The reliability of these CFD methods in predicting both the velocity field and the scalar field has also been assessed. Although a number of experimental studies were reported, due to the challenges of measuring all relevant parameters in the flow-field simultaneously, the understanding of the structure of the FPJ flow is still incomplete. Moreover, the FPJ flow is bi-stable and it switches occasionally between the Precessing Jet (PJ) and the Axial Jet (AJ) modes, which is undesirable. However, the mode switching phenomenon has not been investigated yet. Computational Fluid Dynamics was chosen to address these research gaps. Since no systematic numerical study on the FPJ flow has been reported in literature, the reliability of CFD method in predicting this flow remains unknown. Increasing the understanding of the structure, the mode switching phenomenon and the feasibility of CFD models in predicting the FPJ flow will contribute to the development of industrially relevant design tools, which is the overall objective of this thesis.

The first aim of this research is to comprehensively assess the reliability of two-equation Unsteady Reynolds Averaged Navier-Stokes (URANS) models in predicting the velocity field of the FPJ flow. Five two-equation URANS models, namely the standard k-ε model, the modified k-ε (1.3) model, the modified k-ε (1.6) model, the Re-Normalisation Group (RNG) k-ε model and the Shear Stress Transport (SST) model, were employed to simulate the complex FPJ flow. The predicted phase-averaged velocity field within and in the emerging region of the nozzle, energy of total fluctuation and precession frequency of the FPJ flow were compared against the measured data. Both the RNG k-ε model the modified k-ε (1.6) model failed to predict the precession motion. All main features of the FPJ flow that observed from previous visualization studies were predicted with both the standard k-ε model and the SST model. Furthermore, reasonable quantitative agreement against the experimental result was achieved with both the standard k-ε model and the SST model, although the spreading

and velocity decay rate of the phase-averaged jet within the nozzle were under-predicted.

Secondly, the scalar field of the FPJ flow was simulated with both a two-equation URANS model and a Hybrid Large Eddy Simulation (LES) approach. Under the current numerical configurations, the jet downstream from the nozzle exit was predicted to be mainly distributed in the region near to the wall of the external confining cylinder with both the two approaches, while the measured jet was preferentially concentrated near to the centreline region. This may due to the over-predicted deflection angle of the emerging jet and the under-predicted mixing rate. In addition, the distribution range of the Probability Distribution Function (pdf) of the centreline concentration in the far field was predicted to be narrower than the measured jet. Although the results calculated with the Hybrid-LES approach agrees better with the measured data than that calculated with the SST model, it still did not reproduce the external scalar field of the FPJ flow well. This implies that the simulation of the scalar field of the FPJ flow is significantly more sensitive than is the velocity field.

The third aim of this work is to provide further details of the flow structure and develop a topological model of the FPJ flow, based on the critical point method, previous experimental observations and the numerical results of the CFD model. The unsteady SST model was chosen because it exhibited good qualitative agreement with the experimental result, which is essential for the critical point method. The predicted flow pattern at the surface of both the nozzle and the centre-body were compared against those deduced previously. The flow streamlines, velocity and vorticity cross-sectional contours within the FPJ nozzle were presented to provide further flow details for the development of the vortex skeleton. A vortex skeleton of the FPJ flow within and in the emerging field of the nozzle with six main vortex cores is identified for the first time. All the six vortex cores are deduced to be responsible collectively for the continuous precession.

The fourth aim of this study is to investigate the switching phenomenon and the change of flow structure during the mode switching process using the unsteady SST model. Three methods were employed to trigger the flow to switch from the AJ to the PJ modes, namely imposing a continuous axial perturbation onto part of the inflow, imposing a continuous swirling component to the inlet flow and adopting a slightly asymmetric initial flow field. Some asymmetry was found to be necessary to trigger the mode switching, while the switch time is inversely proportional to the extent of asymmetry. It was also found that the direc-

tion and frequency of the precession are both dependent on the direction and intensity of the imposed inlet swirling, respectively, which is consistent with previous experimental observations. The change to the vortex skeleton of the FPJ flow during the mode switching process is reported for the first time.

Statement of Originality

I certify that this work contains no material which has been accepted for the award of any other degree or diploma in my name in any university or other tertiary institution and, to the best of my knowledge and belief, contains no material previously published or written by another person, except where due reference has been made in the text. In addition, I certify that no part of this work will, in the future, be used in a submission in my name for any other degree or diploma in any university or other tertiary institution without the prior approval of the University of Adelaide and where applicable, any partner institution responsible for the joint award of this degree.

I give consent to this copy of my thesis when deposited in the University Library, being made available for loan and photocopying, subject to the provisions of the Copyright Act 1968.

The author acknowledges that copyright of published works contained within this thesis resides with the copyright holder(s) of those works.

I also give permission for the digital version of my thesis to be made available on the web, via the University's digital research repository, the Library Search and also through web search engines, unless permission has been granted by the University to restrict access for a period of time.

I acknowledge the support I have received for my research through the provision of an Australian Government Research Training Program Scholarship.

Xiao Chen

Acknowledgements

First and foremost, I must gratefully acknowledge my supervisor Professor Graham (Gus) Nathan for the great support of my PhD study. His patient guidance has greatly improved my research ability and writing skill. His accuracy and strict attitude has deepened my understanding of academic study.

I would also like to express my sincere gratitude to my co-supervisor Dr. Zhao Tian for his continuous support and guidance in every aspect of my research work, for his immense knowledge and rich experience in CFD. Thanks for his positive attitude and dry humour, which helped me to "survive" under the pressure of the PhD study.

Besides my supervisors, I would like to thank Associate Professor Richard Kelso for teaching me Critical Point theory, Dr Jordan Parham, Dr Chong Wong and Dr Soon-Kong Lee for their experimental data.

I am thankful to Mr Billy Constantine for providing computer hardware and network support. Thanks also to my schoolmates Dr Chenxi Li, Dr Gary Cai, Dr Yinli Liu, Dr Boyin Ding, Dr Zhiwei Sun, Dr Dahe Gu, Dr Tao Zhu, Dr Shi Zhao, Dr Yangkun Zhang, Dr Manabendra Saha, Dr Ashok Kaniyal, Dr Mehdi Jafarian, Dr Javad Farrokhi Derakshandeh, Dr Alfonso Chinnici, Dr Michael Evans, Dr Yunpeng Xue, Dr Yonglin Zhao, Dr Junwei Wu, Ms Xue Jin, Ms Jingjing Ye, Mr Long Sheng, Mr Houzhi Wang, Mr Chia Thong, Mr Difan Tang, Mr Zhao Lu, Mr Fantai Meng, Mr Elias Arcondoulis and Mr Karn Schumacher for their support and companionship during my PhD candidature.

Finally, a special acknowledgement to my family, Mr Yu Chen, Mrs Jing Xiao and Mrs Shuhan Wang for their enduring patience, endless support and encouragement.

List of Figures

List of Tables

List of Symbols

V	Control volume	48
τ_{ij}	Subgrid-scale stress	48
$\overline{S}_{ij}$	Large scale strain rate tensor	48
μ_{sgs}	LES SGS viscosity	49
l	Length scale of the unresolved eddies	49
ρ	Density	49
q_{sgs}	LES unresolved eddies velocity	49
Δ	Grid size	49
C_S	Smagorinsky constant	49
f_μ	LES wall damping function	49
l_{mix}	mixing length function	49
κ	LES constant	49
u	flow velocity at x direction	50
A_{pz}	area of the perturbation zone	52
A_{pipe}	cross-sectional area of the pipe inlet	52
v_r	radial component of the velocity	52
v_θ	tangential component of the velocity	52

Chapter 1

Introduction

1.1 Background

1.1.1 Hazard of oxides of Nitrogen (NO_x) emission

Nitrogen oxide (NO_2) and nitric oxide (NO) are the main components of NO_x, along with N_2O, N_2O_2, N_2O_3, N_2O_4 and N_2O_5 (US EPA 1999). Oxides of nitrogen are widely considered to be the main precursor of ozone (O_3) (Jhun et al. 2015). Although ozone in the stratosphere preserves the earth from ultraviolet radiation (Wespes et al. 2016), the "ground-level" ozone is detrimental to both human being health (US EPA 2010, WHO 2006) and ecological systems (UNEP & WHO 2011).

Ozone is harmful to lung function and lung tissues if breathed by a human being. The number of emergency department visits that due to the respiratory effects was found to be proportional to the concentration of the ozone in the "ground-level" (Lavigne et al. 2012). It was indicated that an increase of 10 parts per billion (ppb) in the "ground-level" O_3 concentration leads to an approximately 3% increase in the number of respiratory clinic visits (Pride et al. 2015). In addition, long-term exposure to ozone was reported to retard the well development children's lungs (Frischer et al. 1999).

Ozone is a typical greenhouse gas (GHG), along with CO_2, methane (CH_4), nitrous oxide (N_2O), hydro-fluorocarbons (HFC_s), per-fluorocarbons (PFC_s) and sulfur hexafluoride (SF_6) (US EPA 2010). A large proportion of the solar energy that enters the earth is radiated back to the outer space by the earth's surface. A fraction of this energy is absorbed by the greenhouse gases in the troposphere and keep the earth warm. However, an increase of greenhouse gases in the atmosphere would increase the Earth's temperature and lead to global warming (US EPA 2010).

The formation of acidic species in the atmosphere is associated with NO_x, together with

sulphur dioxide (SO_2). These species can be deposited to the ground of the earth in various ways, such as acid rain. The acid deposition can damage plants, leading to a reduction of the production of crop and changing of the soil characteristics (US EPA 2010). It was reported that the loss due to the acid deposition could be more than one billion US dollars every year (Townsend & Howarth 2010). The aquatic life may also be killed due to the acid deposition. Besides, the damage of the acid deposition to the plants causes a reduction of the carbon dioxide (CO_2) absorption, which will influence the whole ecological systems (US EPA 2010).

1.1.2 Emissions of NO_x by rotary kilns

The combustion of fossil fuels is a big contributor to NO_x emissions (Schultz et al. 2015). It is reported that rotary kilns produced 1.5% of the total NO_x emissions in the world in the year 1995 (Houghton 1996). Rotary kiln is widely used in the processing industry, such as the processing of lime, alumina, zinc, cement, etc. It provides an environment of sufficient temperature for the required chemical reactions and achieves relatively high efficiency. Figure 1.1 presents the main components of a typical rotary cement kiln. The long kiln can be more than 100 m long and its diameter is about 2 to 8 m, with a narrow inclined at a small angle to the horizontal (approximately 2°). The raw meal is supplied by the feeder at the higher end of the kiln and gradually moves to the lower end due to both the effect of gravity and the slow rotation of the kiln (approximately one round per minute). The calcining reaction occurs near to the middle of the kiln, where the temperature is about 800 °C. The clinkering reaction takes place in the region near to the burner, with a temperature of approximately 1400 °C (Nathan & Rapson 1995). The peak temperature of the flame within the kiln can reach 2000 °C and the mean temperature of the air that close to the burner is about 1400 °C, while the generation of thermal NO_x is strong because the flame temperature is well in excess of 1500 °C (Chigier 1981).

1.1.3 Gyro-Therm burner

Flame temperature, oxygen and the residence time of the gases within the high temperature region are the three main and interdependent factors that influence the productivity of NO_x (Parham 2000). The total volume of a flame produced by a fluidic precessing jet (FPJ) nozzle is relatively greater than that by a simple round jet nozzle, which leads to a higher

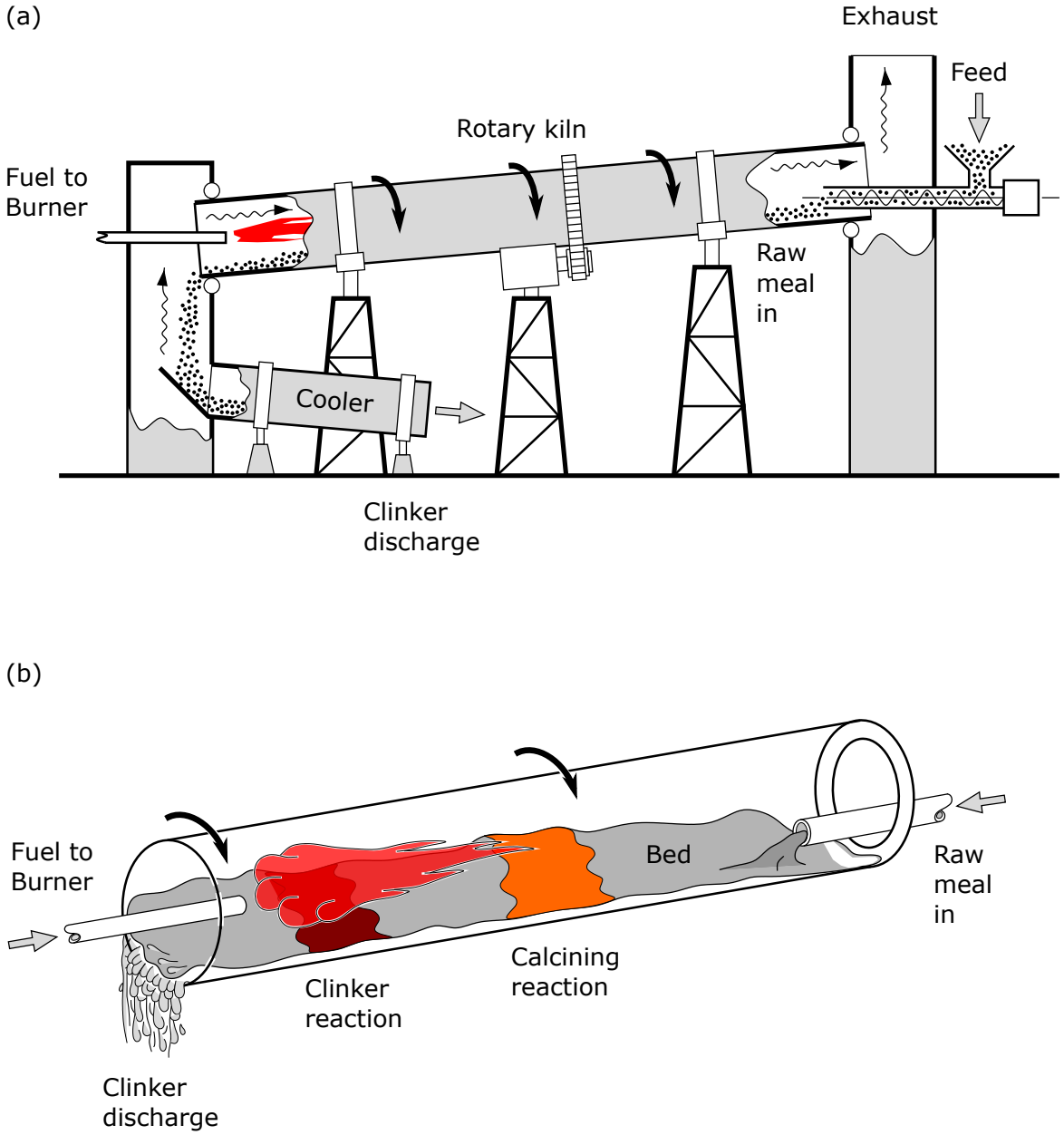

Figure 1.1: Sketch of a typical cement rotary kiln. (a) Main layout (Nobes 1997) and (b) detailed view of the reaction region (Nathan & Rapson 1995). Adapted from Lee (2009).

global residence time and a lower global mixing rate (Nathan et al. 2006). These cause an increase in the presence of soot and thus leads to an increase in the flame radiation. Hence the peak flame temperature will be decreased, which suppresses the generation of NO_x. The FPJ nozzle was adopted in the development of a gas-fired burner (Luxton & Nathan 1988, Luxton et al. 1991), which was reported to reduce the emissions of NO_x from rotary kilns by about 40% compared with conventional burners (Manias & Nathan 1994). It also offers the potential to reduce fuel consumption and improve product quality from rotary kilns (Manias

& Nathan 1993, 1994, Videgar 1997). This burner was further developed and produced by FCT Combustion Pty. Ltd. for industrial applications, known as “Gyro-Therm” burner, shown in Figure 1.2.

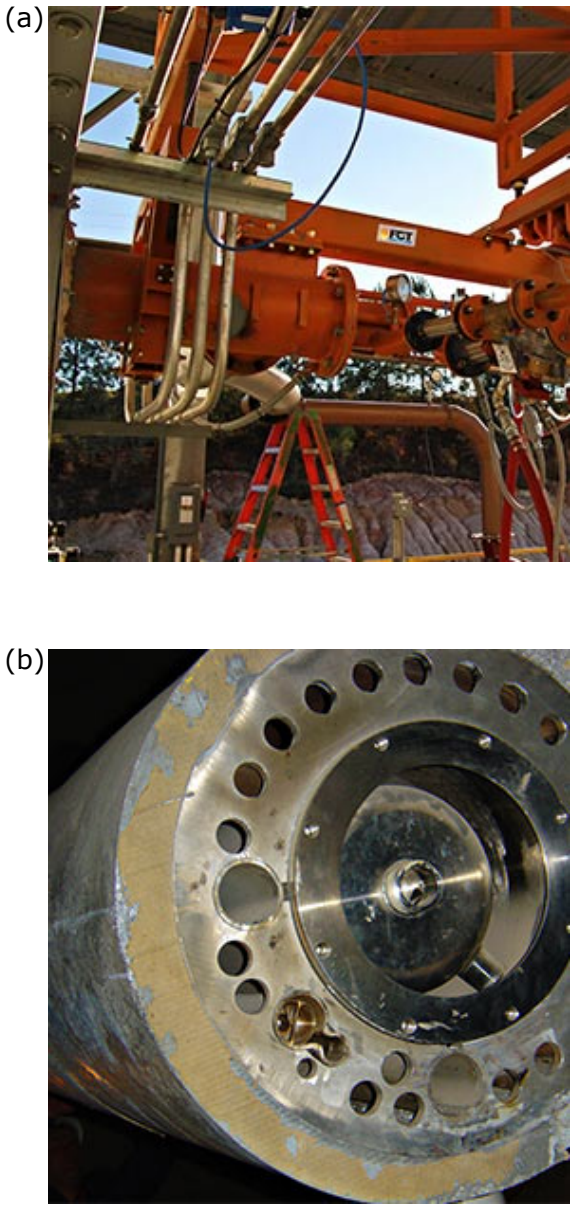

Figure 1.2: Images of a Gyro-Therm MK II kiln burner . (a) The burner and (b) the detailed view of the jet nozzle (FCT Combustion Pty. Ltd 2016).

In the early 1990’s, the “Gyro-Therm” burner was applied to the cement production for Adelaide Brighton Cement Ltd. (Nathan et al. 1990). It was then gradually applied to the alumina (Jenkins et al. 1995) and lime (Manias et al. 1996) production. Until 2009, nearly 30 “Gyro-Therm” burners are employed for the industrial applications in Australia, Europe and North America (Lee 2009).

1.1.4 Computational fluid dynamics

Computational fluid dynamics (CFD) is a simulation technique which is adopted to predict "the behaviour of an engineering product or physical situation under assumed or measured boundary conditions" (Löhner 2008). Computational fluid dynamics includes not only the disciplines of fluid dynamics and heat transfer, which are the engineering skills, but also mathematics and computer science. Besides, CFD is widely adopted in mechanical, chemical, civil engineering areas as research or design tools (Tu et al. 2008). The benefits of developing simulation techniques are:

- A validated CFD model is able to offer more insight than experiments can provide alone, since experiments cannot provide data for as many parameters or as many grid points as can be achieved from a simulation;
- A simulation can predict the performance of a new product or design before building the prototype, hence the number of experiments can be reduced with the use of models to make the money more effective (Löhner 2008).

The three main numerical techniques employed to simulate turbulent gas flows are Direct Numerical Simulations (DNS), Large Eddy Simulation (LES) and Reynolds-Averaged Navier-Stokes (RANS) models. Direct Numerical Simulations can solve problems by full Navier-Stokes equations directly. To directly solve the full Navier-Stokes equations, DNS simulations must fully resolve all length and time-scales of turbulence in a flow. This makes them very computationally intensive, which limits the range of problems to which they can be applied (Eaton et al. 1999). This limitation is of relevance to the simulation of precessing jet flows, where the time-scale of the precession is two orders of magnitude greater than that of the large-scale eddies in a steady jet (Abbas et al. 1993), which currently makes such a simulation impractical. Large Eddy Simulations solve a filtered form of the Navier-Stokes equations, in which resolve the larger scales of motion, but model the sub-grid-scale motions. On the other hand, RANS models solve only the ensemble-averaged form of the Navier-Stokes equations. However, when solved with time-dependence, termed unsteady RANS, or URANS, these models can compute recirculating flow fields whose scale is sufficiently large relative to that of the computational mesh (Guo et al. 2001). The differences between the three numerical approaches are shown in Figure 1.3.

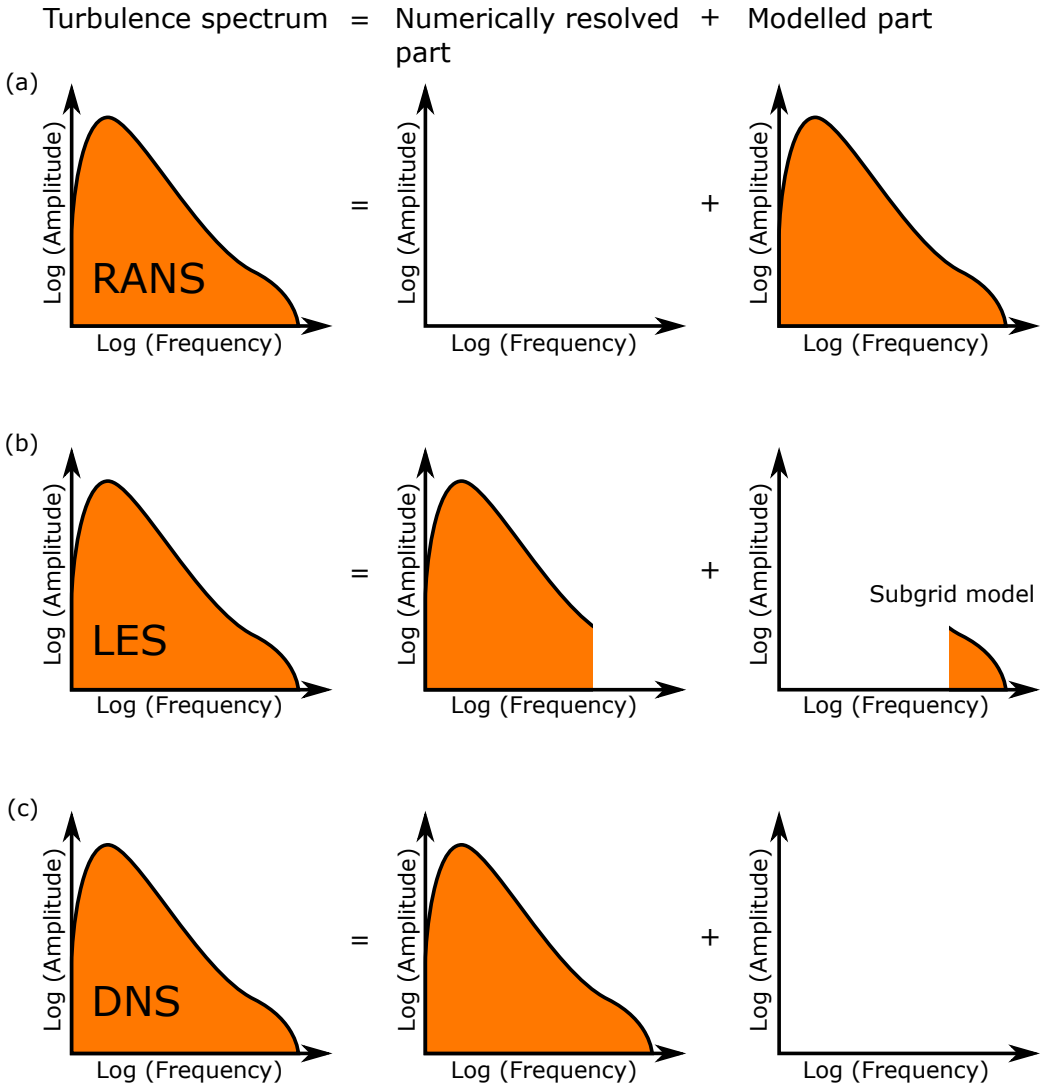

Figure 1.3: Diagram of numerical approaches. (a) Direct numerical simulations, (b) large eddy simulation and (c) Reynolds averaged Navier-Stokes models (Ruprecht et al. 2004).

1.2 Thesis outline

1.2.1 General objectives

A lot of work on the structure of the FPJ flow has been reported by the research group of the University of Adelaide (Kelso 2001, Lee 2009, Nathan et al. 1998, Wong et al. 2008), however, knowledge of the ensemble-averaged structure of the FPJ flow remains incomplete due to the challenge of measuring all relevant parameters in the flow-field simultaneously. Moreover, while much is now known about the precessing flow itself (Nathan et al. 1998, Wong 2004), a phenomenon within the nozzle that has received little attention to date is the bi-stable nature of the flow. It has been observed that the flow occasionally switches between

the dominant precessing jet (PJ) mode and the axial jet (AJ) mode (Hill et al. 1992, Nathan & Luxton 1992*a*). While geometric configurations have been identified where the fractional time spent in the AJ mode is negligible, nevertheless the phenomenon is undesirable and also remains of fundamental interest. However, the switching between the two modes is difficult to study by experiments because it is an intermittent and rare event that depends on the geometry. Hence, there is a need to employ numerical models for these investigations.

Furthermore, in addition to the scientific issue, is the industrial nozzle design. Since many industries cannot afford long and expensive computations, there is strong incentive to develop ever lower-cost modelling approaches, and hence a need for a more comprehensive understanding of the trade-off between computational cost and accuracy in a range of Unsteady Reynolds-Averaged Navier-Stokes (URANS) and LES approaches. Hence there is a need for a systematic investigation of the influence of the different modelling approaches using identical computational grids for a range of modelling approaches in an oscillating flow for which good experimental data are available. However, to date, there is no systematic assessment of the efficacy of both URANS models and LES approaches in modelling FPJ flows reported in the literature. That is, no suitable approach to modelling such flows has been identified. Hence the four main objectives of this investigation are:

1. to assess the potential of two-equation URANS models to model the unsteady, precessing flow within, and in the emerging field of the FPJ nozzle;

2. to assess the performance of both a Hybrid-LES approach and two-equation URANS model in predicting the scalar mixing of the FPJ flow;

3. to provide more details of the ensemble-averaged structure of the FPJ flow based on the data calculated with a validated numerical method and measured through previous experiments;

4. to provide new understanding of the mode switching phenomenon of the flow through the FPJ nozzle.

1.2.2 Dissertation structure

The main features of the FPJ flow is introduced in Chapter 2. It also reviews the previous experimental works on both the velocity and scalar field of the FPJ flow and the numerical

studies in predicting the related flows. Four knowledge gaps are identified and the detailed aims of this investigation are presented.

In Chapter 3, the methodology for this investigation to achieve the aims is described. The detailed geometric dimensions and generated meshes for three FPJ nozzles are presented, together with the numerical configurations. Three two-equation URANS models, i.e. the standard k-ε model, the Re-Normalisation Group (RNG) k-ε model and the Shear Stress Transport (SST) model are described. Moreover, the critical point theory, which is employed for the flow structure analysis is introduced.

In Chapter 4, the reliability of three two-equation URANS models are assessed, i.e. the standard k-ε model, the RNG k-ε model and the SST model, in predicting the velocity field of the FPJ flow within and in the emerging field of the nozzle. The predicted jet centreline velocity decay, the equivalent jet diameter, the precession frequency and the energy of total fluctuation are validated against the measured result (Wong 2004, Wong et al. 2003). The effect of the constant $C_{1\varepsilon}$ on the FPJ flow simulation is assessed. It is found that good qualitative and reasonable quantitative agreement against the measured results can be achieved with both the standard k-ε model and the SST model.

In Chapter 5, the feasibility of the SST model and the Hybrid-LES approach in predicting the scalar mixing of the FPJ flow downstream from the nozzle exit is assessed. The calculated nozzle centreline concentration, the probability distribution function (pdf) of the centreline concentration in the far field, the instantaneous and mean cross-sectional concentration contours are compared against the measured results (Parham 2000, Parham et al. 2005). Although the SST model is proved to be useful in predicting the velocity field of the FPJ flow, it fails to correctly predicted the concentration distribution in the external field under the current numerical configurations. The Hybrid-LES approach achieves relatively better agreement against the experimental data, however, it is still not able to reproduce the scalar field of the FPJ flow well.

In Chapter 6, the flow structure of an ensemble-averaged FPJ flow is analysed, based on the concepts of critical point theory, previous experimental data and the results predicted with the SST model. The predicted surface flow patterns are compared with the deduced results in previous works. A vortex skeleton of the FPJ flow within the nozzle, which is comprised of six vortex cores, is identified.

In Chapter 7, the phenomenon of "switching" between the two bi-stable Axial Jet (AJ) and Precessing Jet (PJ) flow modes in the FPJ nozzle is investigated using the SST model. Three methods to trigger the flow to switch from the AJ to the PJ modes are assessed. It is found that some asymmetry in either the inlet flow or the initial flow field is necessary to trigger the mode switching, with the time required to switch being dependent on the extent of the asymmetry. The changes of the vortex skeleton within the nozzle during the mode switching process are presented. In addition, during the switching process from the AJ to the PJ modes, both the spreading rate and the maximum axial velocity decay rate of the jet within the nozzle increase gradually, which is consistent with previous experimental observations.

In Chapter 8, all the findings from the chapters 4 to 7 is summarized and the conclusions of the whole work is drawn. It also provides suggestion for the future investigations.

1.3 Publications arised from this work

1. Chen, X., Tian, Z. F., and Nathan, G. J., 2017, "Assessment of the Reliability of Two-equation URANS Models in Predicting a Precessing Flow," Submitted to Journal of Fluids Engineering.

2. Chen, X., Tian, Z. F., and Nathan, G. J., 2017, "Numerical Investigation on the Scalar Mixing of a Fluidic Precessing Jet Flow," Submitted to Journal of Fluids Engineering.

3. Chen, X., Tian, Z. F., Kelso, R. M., and Nathan, G. J., 2017, "The Topology of a Precessing Flow Within a Suddenly Expanding Axisymmetric Chamber," Journal of Fluids Engineering, 139(7), pp. 071201-071201-071210.

4. Chen, X., Tian, Z. F., Kelso, R. M., and Nathan, G. J., 2017, "New Understanding of Mode Switching in the Fluidic Precessing Jet Flow," Journal of Fluids Engineering, 139(7), pp. 071102-071102-071110.

5. Chen, X., Tian, Z. F., and Nathan, G. J., 2012, "Numerical simulation of the flow within a fluidic precessing jet nozzle," Proc. Australasian Fluid Mechanics Conference (18th: 2012: Launceston, Tasmania).

6. Chen, X., Tian, Z. F., and Nathan, G. J., 2017, "Effect of turbulent Schmidt number on the scalar field simulation of a fluidic precessing jet flow," Proc. The 8th International

Conference on Computational Methods (ICCM2017: Guilin, Guangxi, China).

Chapter 2

Literature review

2.1 Fluidic precessing jet (FPJ) flow

The FPJ nozzle comprises an axisymmetric chamber with a large sudden expansion at the inlet (Figure 2.1). A centre body (CB) and a lip can be added slightly upstream from the nozzle exit to increase the probability of generating the precessing jet (Wong 2004). The inlet to the chamber can be fed either from a smooth contraction, a pipe or an orifice plate.

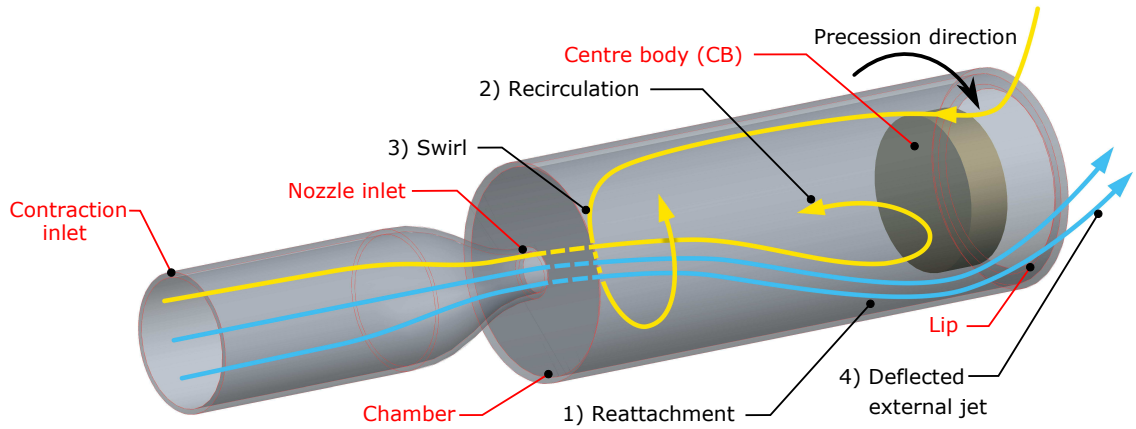

Figure 2.1: A schematic diagram of the fluidic precessing jet nozzle and flow.

The requirement of nozzle's geometry to achieve reliable precession has been reported previously (Nathan 1988). It was found that the precession motion of the jet within the nozzle chamber occurs if the ratio between the diameter of the nozzle chamber (D) and the nozzle inlet (d), namely expansion ratio, is greater than 5, while the ratio between the length of the chamber (L) and D is generally between 2.6 and 2.8. Besides, it was found that the Reynolds number (Re) at the FPJ nozzle inlet should be greater than 2×10^5 (Nathan et al. 1998). Here Reynolds number is defined as

$$Re = \frac{U_o \times d}{\nu} \quad , \tag{2.1}$$

where U_o is the bulk velocity at the nozzle inlet orifice and ν is the kinematic viscosity. In a

later study, it was reported that the critical expansion ratio for the precession motion to occur is 3.75, based on a parametric experimental work (Hill et al. 1995).

Four dominant features of the FPJ flow were summarised by Nathan et al. (1998). These features are also adopted as the qualitative criteria against whether or not a given calculated flow-field exhibits precession in the current work. The four flow features of FPJ flow, also shown in Figure 2.1, are:

- the reattaching jet flow is instantaneously asymmetric and the point of reattachment moves azimuthally around the wall of the chamber;
- a recirculating flow region is found diametrically opposite to the jets location;
- a region of swirling fluid is found at the upstream end of the chamber;
- the jet emerging from the chamber is aligned instantaneously at a large angle to the axis of the chamber (Nathan et al. 1998).

2.2 Velocity field within and in the emerging region of an FPJ nozzle

2.2.1 Phase-averaged measurement on the internal velocity field of the FPJ flow

Wong et al. (2003) reported the phase-averaged axial velocity contours through a series of cross-sectional planes within the FPJ nozzle, based on the experiment using a laser Doppler anemometry (LDA) system. It was found that both the spreading and the centre-line velocity decay of the phase-averaged FPJ flow within the nozzle are faster than that of a free turbulent jet, which was suggested to be due to the effect of the reversed flow. Moreover, the entrainment rate of the FPJ flow was found to be about 6.8 times greater than that of a round turbulent jet based on measurement of the phase-averaged jet in the emerging field (Wong et al. 2003).

2.2.2 The effect of nozzle configurations

Wong et al. (2004) assessed the influence of the nozzle configurations on the FPJ flow. Nine configurations of the FPJ nozzle were adopted, i.e. nozzles with three inlet (long pipe,

contraction and orifice) and two outlet configurations (centre body and lip), as shown in Figure 2.2. The probability of precession was found to be influenced by the inlet conditions. Configurations with sharp-edged orifice and long pipe inlet produce jet precession more easily than ones with smooth contraction inlet. For chamber-lip-centrebody configurations, the flow produced with orifice inlet FPJ nozzle has the highest turbulence intensity and lowest peak mean axial exit velocity, while the turbulence intensity is the lowest for the flow produced with pipe inlet FPJ nozzle. Besides, the flow produced with orifice inlet FPJ nozzle has the highest Strouhal number (S_t) while it is the lowest for the case with pipe inlet. Here S_t is defined as

$$S_t = \frac{f_p \times (D-d)}{2U_o} \quad , \tag{2.2}$$

where f_p is the precession frequency (Nathan et al. 1998).

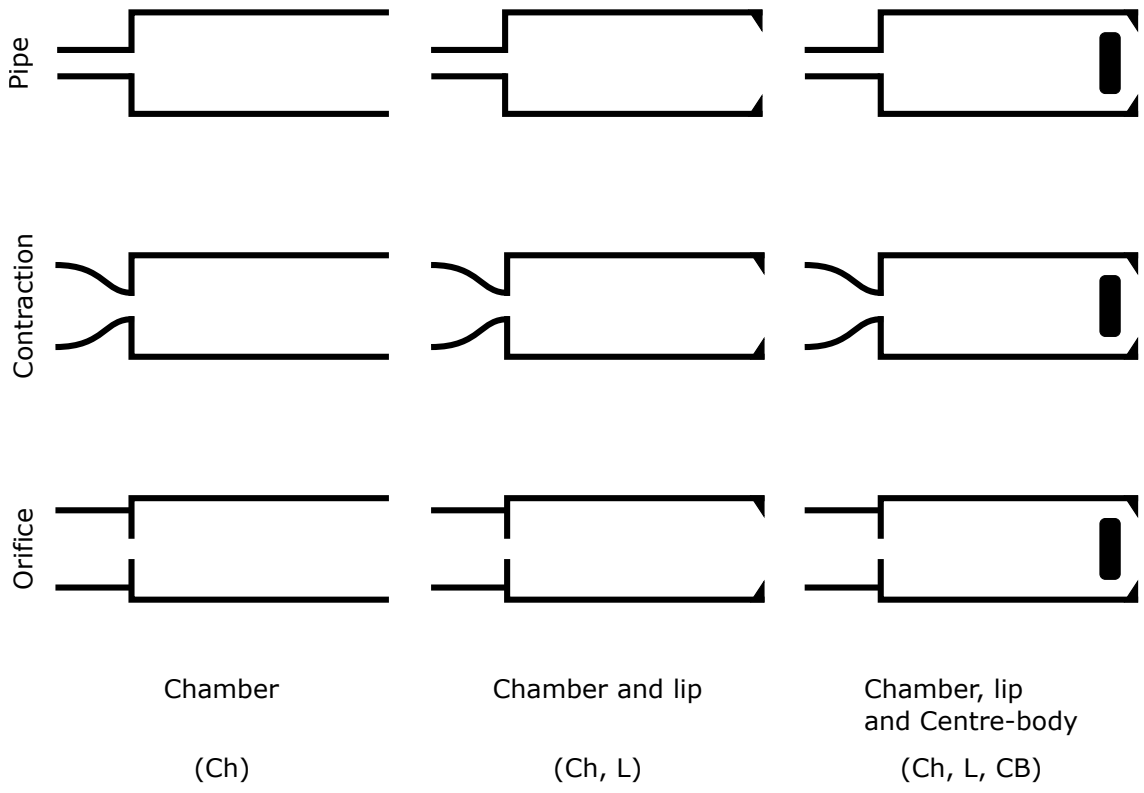

Figure 2.2: A schematic diagram of the configurations of the fluidic precessing jet nozzles. Adapted from Wong et al. (2004).

2.2.3 Precession frequency

Wong et al. (2008) measured the precession frequencies of the FPJ flows with Reynolds number in the range from 30,000 to 90,000 using a hot-wire probe in the emerging field.

The value of f_p varies from 3 Hz to 7.5 Hz as the increase of Re. This is consistent with the trend between precession frequency and Reynolds number that reported by Hill et al. (1995), who counted the precession frequency of the FPJ flow based on their visualisation investigation. The precession frequency of the jet was found to increase as the increase of the chamber length (Mi & Nathan 2000). Regarding the configurations of the inlet, Wong et al. (2004) found that the precession frequency of the flow produced with an orifice inlet nozzle is highest f_p, followed by the that with a contraction inlet and a pipe inlet nozzles. This is also consistent with the suggestion of Mi et al. (1999) that an increase of the momentum of the internal recirculated flow causes the precession frequency to increase.

2.2.4 Numerical simulation on the velocity field of an FPJ flow

To develop numerical models of the FPJ flow is a significant challenge, not only because of the large scale and unsteady nature of FPJ flows, but also because this flow combines several complex features, each of which is difficult to model, namely oscillations, swirl, flow separation and flow impingement (Nathan et al. 1998).

2.2.4.1 Two-equation URANS models

In the many two-equation URANS models, the standard k-ε model, the Re-Normalisation Group (RNG) k-ε model and the Shear Stress Transport (SST) model are widely used in modelling industrial flows (Versteeg & Malalasekera 2007). The general validity of the RNG k-ε model has been a matter of some controversy. It was developed to replace the empirical "constants" in the standard k-ε model with an analytical relationship developed from Re-normalisation Group theory and has been found to provide better performance than the standard k-ε model in some studies, such as in predicting three swirling flows (Escue & Cui 2010, Gupta & Kumar 2007, Orfanoudakis et al. 2005). However, the development of the RNG k-ε model is controversial (Nagano & Itazu 1997, Teodorovich 1994, Wang & Wu 1993). The SST model combines the strengths of the standard k-ε model and the k-ω model to offer some advantages over the standard k-ε model in near wall flows (Menter 1996, Menter et al. 2003, Tkatchenko et al. 2007), such as a rectangular jet in a cross flow (Tian et al. 2011) and a separating flow in a planar asymmetric diffuser (El-Behery & Hamed 2011). Nevertheless, the limitations of two-equation URANS models are also well known, which assumes the turbulent viscosity to be isotropic. Approaches to address these limita-

tions span two-equation URANS through to Large Eddy Simulation (LES) (Tian et al. 2007), which offer a trade-off between computational expense and accuracy.

2.2.4.2 Triple decomposition

For the FPJ flow in the current work, the instantaneous value of a given parameter can be decomposed following Hussain & Reynolds (1970), as follows:

$$\Phi(t) = \bar{\Phi} + \tilde{\Phi}(t) + \Phi' \quad . \tag{2.3}$$

Here $\bar{\Phi}$ is the mean value, $\tilde{\Phi}(t)$ is the periodic component and Φ' is the stochastic turbulent fluctuation relative to the periodic flow. The sum of the mean value and periodic component, i.e. $\langle\Phi\rangle(t) = \bar{\Phi} + \tilde{\Phi}(t)$, is defined as the ensemble-averaged component (Bosch & Rodi 1998). In the simulation, the ensemble-averaged component, which is related to the precession motion, is resolved while the turbulence component, which is superimposed on this periodic motion, is modelled using two-equation URANS models. Here, the phase-averaged flow-field was obtained by taking the average of the converged flow-fields at the same phase of the cycle.

2.2.4.3 Numerical approach in predicting the velocity field of similar flows

An unsteady k-ε model was adopted to simulate a related flow downstream from a long pipe inlet into a large chamber with a similar expansion ratio to the FPJ nozzle (Guo et al. 2001). They predicted flow streamline patterns that yield qualitative agreement with the related FPJ flow including the asymmetric reattachment of the jet, the recirculation zone and the swirling flow in the most upstream part of the nozzle. The calculated Strouhal number is nearly independent with the Reynolds number in the simulation, which is consistent with previous experimental works (Hill et al. 1995, Nathan et al. 1998). It was found that the time step is small enough to predict the oscillation frequency with reasonable accuracy if 180 time steps are allowed in each precession (Guo et al. 2001). However, the length-diameter ratio (L/D) of the downstream chamber is about 16, more than five times greater than that of the FPJ nozzle, at which distance the flow approaches being fully developed. This contrasts the exit flow from the FPJ nozzle, which spreads rapidly and generates a complex recirculation of external fluid back into the nozzle chamber. Besides, there is no direct comparison with measured data and only one turbulence model was employed in their work.

The reliability of both the unsteady k-ε model and the unsteady Reynolds Stress Model

(RSM) in predicting a swirling flow with very-large-scale oscillation, i.e. a Precessing Vortex Core (PVC), was assessed by Wegner et al. (2004). They found that both the two URANS models are able to predict the PVC phenomenon and can achieve good agreement with the measured mean axial velocities. The Strouhal number was found to be under-predicted with both the standard k-ε model and the RSM by 5%. Consistent with the work of Wegner et al. (2004), the unsteady k-ε model was able to capture large scale features of the time-averaged flow and to achieve good agreement with measured mean axial velocities in simulating another swirling flow with a PVC (Dunham et al. 2009).

2.2.4.4 The effect of the constant $C_{1\varepsilon}$

It was reported that both the spreading rate and the centreline velocity decay rate of the precessing jet within the nozzle are greater than that of a non-precessing unconfined jet and are close to a jet in a weak counter-flow (Wong et al. 2003). Some studies reported that the standard k-ε model over-predicts the spreading rate of an unconfined round jet (Morse 1977, Pope 1978). The constant $C_{1\varepsilon}$ in the turbulence dissipation rate (ε) equation of the standard k-ε model was modified from 1.44 to 1.6 in previous works to overcome this issue (Morse 1977, Pope 1978). However, how well the standard k-ε model predicts the spreading rate of an FPJ flow is unclear. Furthermore, the extent to which the rates of spread and decay correlate with a model predicts the occurrence of precession has not been reported previously.

2.2.5 The first aim: Assessment of two-equation URANS models in predicting the velocity field of a precessing jet flow

Before embarking on the study of both internal flow structure and mode switching phenomenon, it is necessary to assess the strengths and limitations of the two-equation URANS models, which saves a noticeable amount of computing time compared to LES approach, in predicting the velocity field of the FPJ flow. However, no systematic assessment of this approach is presently available. Hence the first aim of the present study is to assess the extent to which two-equation URANS models of the phase mean flow can reproduce known qualitative features and quantitative data of FPJ flow. The RNG k-ε model, the SST model, together with the k-ε model with the constant $C_{1\varepsilon}$ of 1.3 (the modified k-ε (1.3) model), 1.44 (the standard k-ε model) and 1.6 (the modified k-ε (1.6) model), were adopted for the

assessment.

2.3 Scalar field in the external region of an FPJ nozzle

2.3.1 The influence of the precession motion on the scalar mixing

Both the centre-line concentration decay rate and the spreading rate of the FPJ flow were found to be nearly twice that of the round jet from the experiment of Newbold (1998). Moreover, large-scale roller structures were found downstream from the exit of the FPJ nozzle, the size of which is about three times that of the round jet. This is consistent with the work of Nathan et al. (1997) that the precession motion of the jet causes a increase of the size of the largest scale of turbulent mixing. A systematic measurement of the scalar field of the FPJ flow downstream from the nozzle exit was reported by Parham (2000), who found that the centreline concentration decay rate of the FPJ flow in the emerging field of the nozzle exit is about four times greater than that of a free round jet (Becker et al. 1967), while it reduces suddenly at an "elbow point" in the near field and the decay rate is almost constant downstream from this point (Parham et al. 2005). In addition, the probability distribution function (pdf) of the jet centreline concentration of the FPJ flow was found to be broader than that of a pipe flow (Parham 2000).

2.3.2 The influence of the co-flow velocity and confinement on the scalar mixing

The scalar mixing of the FPJ flows with five co-flow velocities ranging from $4.31 \times 10^{-3}U_o$ to $24.5 \times 10^{-3}U_o$ and three diameters of confinement, i.e. $7.6D$, $10.3D$ and $12.9D$, were assessed in the experimental work of Parham (2000). It was found that an increase of the confinement diameter leads to an increase of the jet centreline concentration. Furthermore, the jet was found to be impinged on the wall of the confinement if its diameter is not sufficiently large, which has a significant effect on the instantaneous mixing in the region near to the impingement. Parham (2000) also found that the velocity ratio between the co-flow to the exit flow of the FPJ nozzle has no influence on the centreline concentration decay rate in the far field and has slight effect on the spreading rate of the jet and the pdf of the centreline jet concentration in the far field (Parham 2000).

2.3.3 Numerical simulation on the scalar field of an FPJ flow

2.3.3.1 A simplified prediction of scalar mixing of the FPJ flow

The standard k-ε model was employed to simulate both the velocity and scalar field of an FPJ flow (Smith et al. 2003). The two-dimensional fluid domain was divided into six regions, employing adjusted values of the constant $C_{1\varepsilon}$ in each region to match the measured centreline velocity within the FPJ nozzle and jet centreline concentration in the external field (Parham 2000). However, this work adopted a two-dimensional, steady state model, which is not able to predict the complex structure of the highly three-dimensional and unsteady FPJ flow (Wong 2004).

2.3.3.2 Hybrid-LES approach in predicting scalar mixing

Compared with the two-equation URANS models, the LES method has been more widely adopted in the scalar field simulations due to its superior performance. The velocity field and the scalar mixing of the flow in a coaxial jet mixer have been studied using three LES approaches and three URANS models.

Tkatchenko et al. (2007) found that, from their numerical study of the flow in a coaxial jet mixer, both the velocity and scalar field that predicted with the SST model are closer to the measured results than the standard k-ε model and the Reynolds Stress Model. The dynamic mixed LES approach achieves the best agreement against the experimental data and captures the most flow features (Tkatchenko et al. 2007).

LES approach was also adopted to simulate a flow in a high-swirl fuel injector (Cheng et al. 2012). Good agreement with the measured results was achieved in predicting the velocity at the injector exit, the concentration of the jet on a serious of cross-sectional planes and the probability density function (pdf) at a certain point downstream from the exit. To save the computing time, Hybrid-LES method was adopted in many researches (Abe & Ohtsuka 2010, Jakirlić et al. 2010). For Hybrid-LES approaches, the URANS model is generally employed in modelling the flow in the near wall region, while the flow in the other regions are solved with LES.

2.3.4 The second aim: Assessment of both the Hybrid-LES approach and a two-equation URANS model in predicting the scalar mixing of a precessing jet flow

LES method showed its superiority in scalar field modelling, however, its strengths and limitations in predicting the scalar field of the FPJ flow is still unknown, so do the two-equation URANS models. Hence the second aim of this thesis is to assess the reliability of both a Hybrid-LES approach and a two-equation URANS model in predicting the scalar mixing of the FPJ flow.

2.4 Flow structure

2.4.1 Structure of the FPJ flow

2.4.1.1 Instantaneous FPJ flow structure

A visualization study was conducted to reveal the instantaneous flow pattern of the FPJ flow (Nathan et al. 1998), shown in Figure 2.3. The swirl in the most upstream region, reattachment of the jet and the deflected leaving jet can be observed clearly through the reported image. Nathan et al. (1998) indicated that through their observation, the angle between the leaving jet and the nozzle axis varies approximately from 30° to 70°, showing a significant cycle to cycle variation of the FPJ flow.

Cafiero et al. (2014) measured a broad slice through the instantaneous flow structure of the precessing jet flow. The nozzle they adopted is similar to the work of Nathan et al. (1998), but excludes a lip at the exit of the chamber. Two helical structures were identified embedded within the jet near to the inlet plane, which was deduced to be caused by the swirling motion. These helical structures were also observed in the work of Ceglia et al. (2017), who investigated the structure of a precessing jet using tomographic PIV. The asymmetric entrainment was found to play an important role in the instantaneous large-scale coherent structures and the precession motion of the flow (Ceglia et al. 2017). However, due to the limitation of measurement area for both the two works, the reported instantaneous flow structures are not complete.

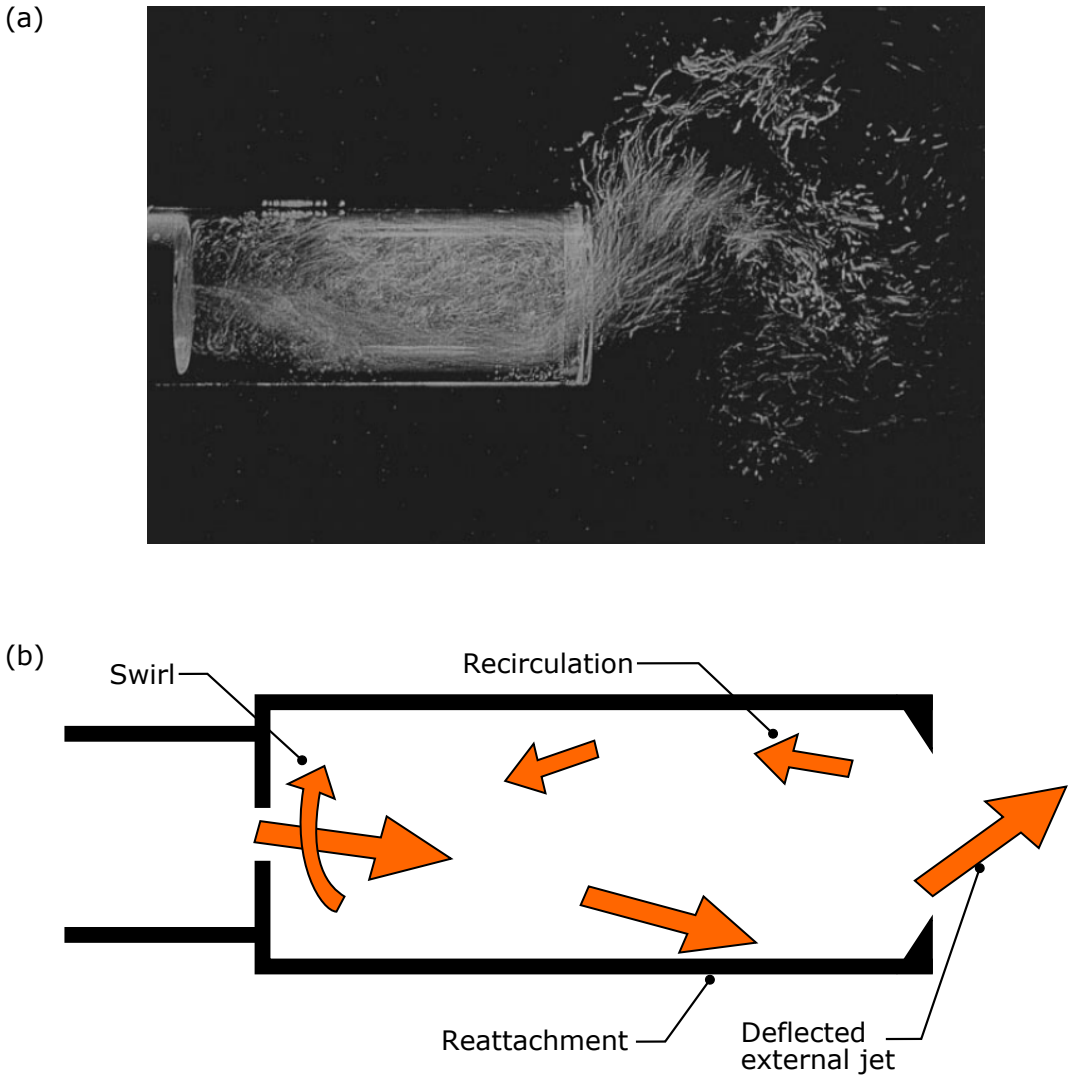

Figure 2.3: Visualization of an instantaneous FPJ flow obtained from Nathan et al. (1998) at *Re*=15,000. (a) The surface visualization flow pattern and (b) the interpreted flow pathlines. Adapted from Nathan et al. (1998).

2.4.1.2 Time-averaged FPJ flow structure

The time-averaged surface flow pattern were presented in the work of Nathan et al. (1998), using both the china-clay and oil-droplet methods. The time-averaged surface flow pattern on the downstream surface of the sudden expansion, shown in Figure 2.4, revealed a strong spiralling flow and provided further evidence of the upstream swirling flow (Nathan et al. 1998). Nathan et al. (1998) also identified three bifurcation lines in the time-smoothed surface flow pattern within the FPJ nozzle chamber from flow visualisation, shown in Figure 2.5. A negative bifurcation line was found to be located at about one-quarter of the chamber length from the inlet, upstream from which the flow exhibits a strong swirl. A positive bi-

furcation line was revealed in approximately the middle of the chamber, which was deduced to be related to the reattaching jet. In addition, a negative bifurcation line located near to the nozzle exit was found, which is related to the lip. These time-averaged surface flow patterns are useful for qualitative validation of a CFD model. However, the instantaneous surface flow pattern of the FPJ flow is still unclear.

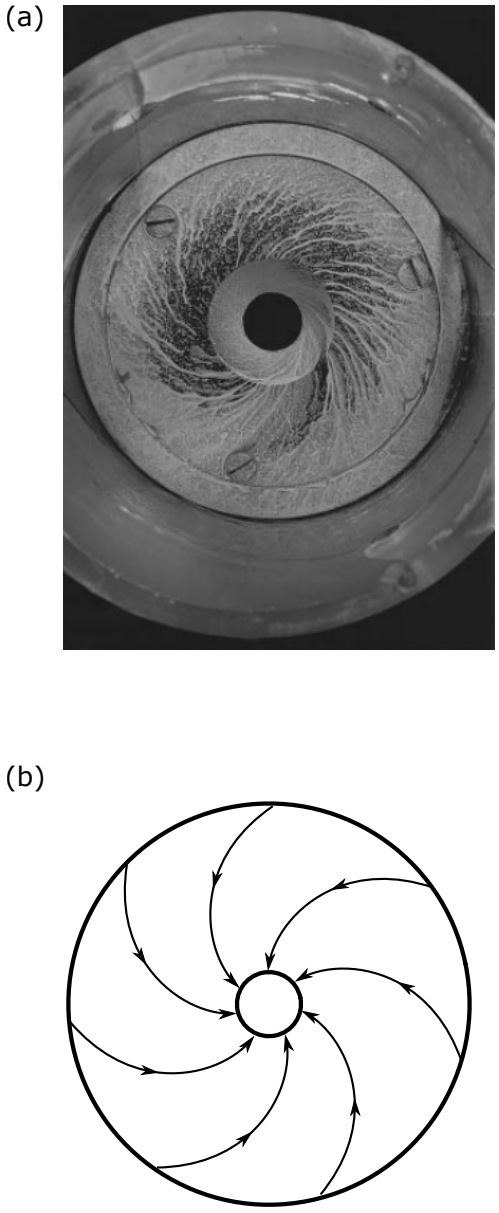

Figure 2.4: Visualization of the time-averaged flow pattern on the inlet base surface of an FPJ nozzle (Nathan et al. 1998). (a) The surface visualization flow pattern and (b) the interpreted flow pathlines. Adapted from Nathan et al. (1998).

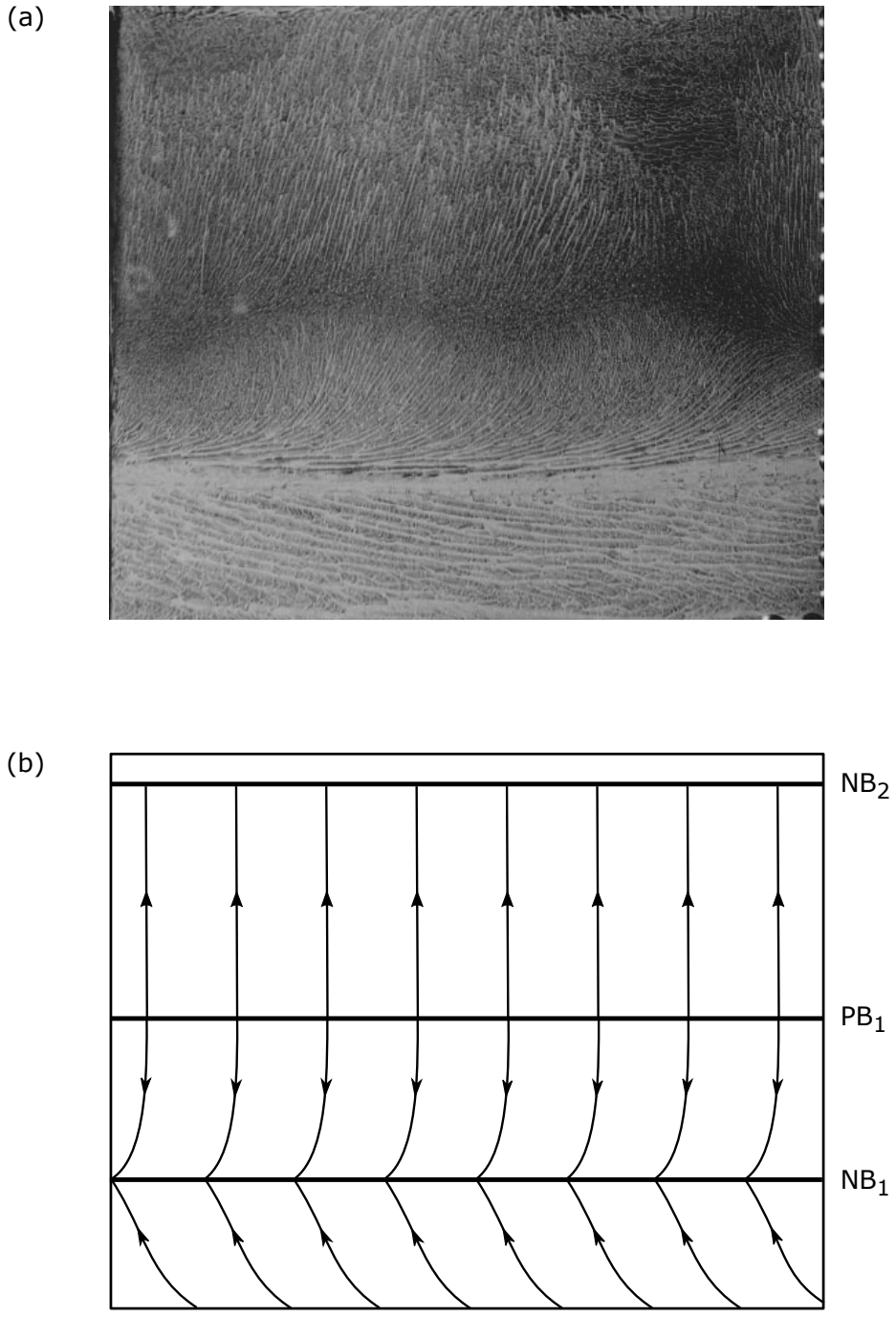

Figure 2.5: Visualization of the time-averaged flow pattern on the surface of an FPJ nozzle (Nathan et al. 1998). (a) The surface visualization flow pattern and (b) the interpreted flow pathlines. Note that NB is negative bifurcation and PB is positive bifurcation. Adapt from Nathan et al. (1998).

2.4.1.3 Phase-averaged FPJ flow structure

The phase-averaged velocity field of the FPJ flow within the nozzle has been measured by Wong et al. (2003), who adopted an FPJ nozzle (CH, L, CB) with a contraction inlet. Flow

streamlines (Figure 2.6) were reported based on the measured phase-averaged cross-sectional axial velocity contours of the FPJ flow within and in the emerging field of the nozzle, which is similar to the instantaneous flow pattern in the work of Nathan et al. (1998), although the adopted nozzles are not completely the same. Moreover, it showed that due to the squeezing by the centre body and the chamber wall, the cross section of the FPJ flow becomes kidney-shaped downstream from the nozzle exit. Although the phase-averaged structure of the flow within the nozzle is not complete, it can be adopted for qualitative validation of the CFD models in the current work.

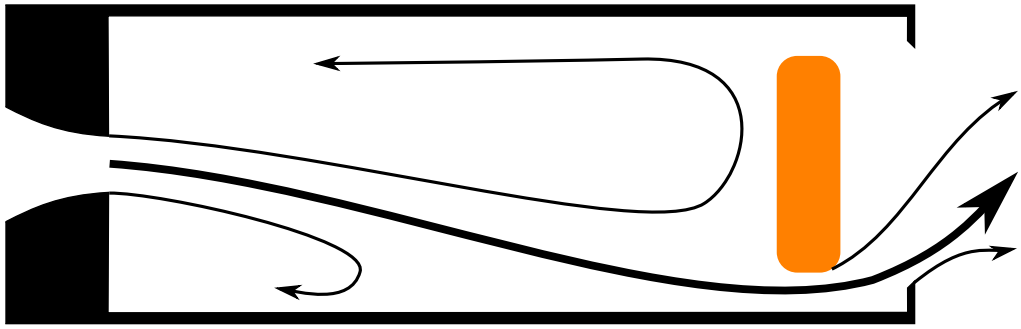

Figure 2.6: Streamlines of the FPJ flow that deduced based on the measured phase-averaged axial velocity. Adapted from Wong et al. (2004).

Wong et al. (2008) studied the external flow field of the FPJ flow using Particle Image Velocimetry (PIV), adopting a nozzle (CH, L, CB) with a contraction inlet. The streamlines on the downstream face of the centre body was deduced based on the surface flow visualization of a steady deflected jet from the FPJ nozzle, shown in Figure 2.7. Together with the measured vorticity field in the near field, they proposed a vortex pair that originates from the downstream face of the centre body and extends to infinity, shown in Figure 2.8a. An alternative structure of this vortex, which forms a loop downstream from the centre body (Figure 2.8b), was proposed by Wong (2004). However, the deduced structure of the FPJ flow downstream from the nozzle exit has not been validated.

Two edge vortex pairs were revealed based on the measured phase-averaged vorticity field and the deduced flow patterns on the downstream surface of the centre body. One edge vortex pair (Edge 1 vortex) is originated from the edge of downstream face of the centre body and extends to infinity, while the other pair (Edge 2 vortex) is originated from the edge of the lip surface, shown in Figure 2.9. However, due to experimental constraints, which prevented measurements from being obtained close to the nozzle exit, they were unable to

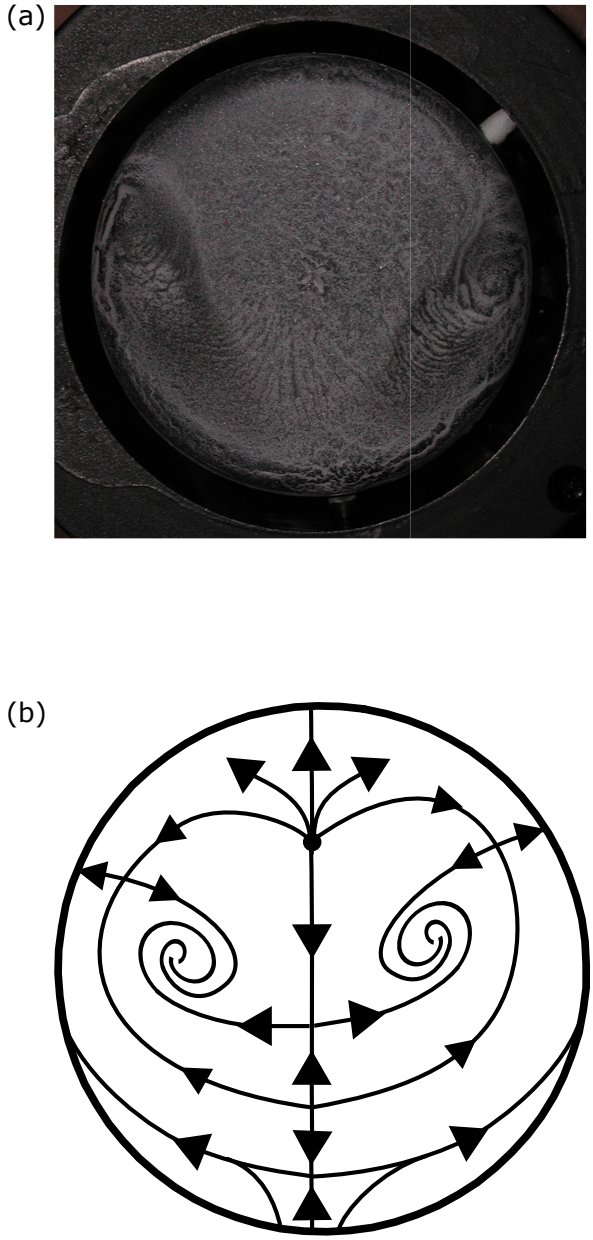

Figure 2.7: Visualization of the flow pattern on the downstream face of the centre body of a steady deflected jet nozzle (Wong et al. 2008). (a) The surface visualization flow pattern and (b) the interpreted flow pathlines. Adapted from Wong et al. (2008).

confirm all details of the flow-field in this region. Wong et al. (2008) therefore hypothesised the presence of a feature they termed the "Edge 3 vortex" (Figure 2.9), whose structure is yet to be confirmed. Therefore, there is a need to provide more information of the "Edge 3 vortex".

2.4.2 Structure of similar flows

Lee (2009) derived the flow structure for a closely related flow, i.e. oscillating-triangular-

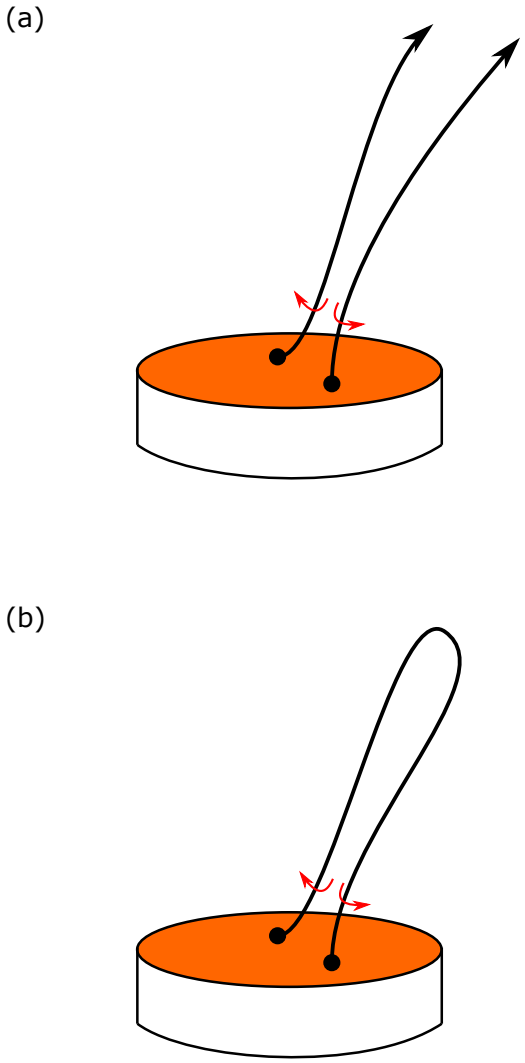

Figure 2.8: Two proposed skeletons of the vortex originated from the downstream face of the centre body. (a) Extending to infinity (Wong et al. 2008) and (b) forming a vortex loop (Wong 2004).

jet (OTJ). The ensemble-averaged nozzle surface flow field of the OTJ flow were deduced based on the visualization of the measured surface streak-lines of a stationary deflected triangular jet (SDTJ) and the pressure measurement on the wall of the nozzle, shown in Figure 2.10. The streamlines of the OTJ flow on a longitudinal cross-sectional plane were proposed, shown in Figure 2.11a. They also deduced the streamlines of the flow through an FPJ nozzle (Figure 2.11b), based on the phase-averaged axial velocity measurements by Wong et al. (2003). The vortex loop within the nozzle was found to be suppressed by the centre body. A vortex skeleton of the OTJ flow was then proposed based on the nozzle surface streak-lines, together with the ensemble-averaged velocity and vorticity field that measured

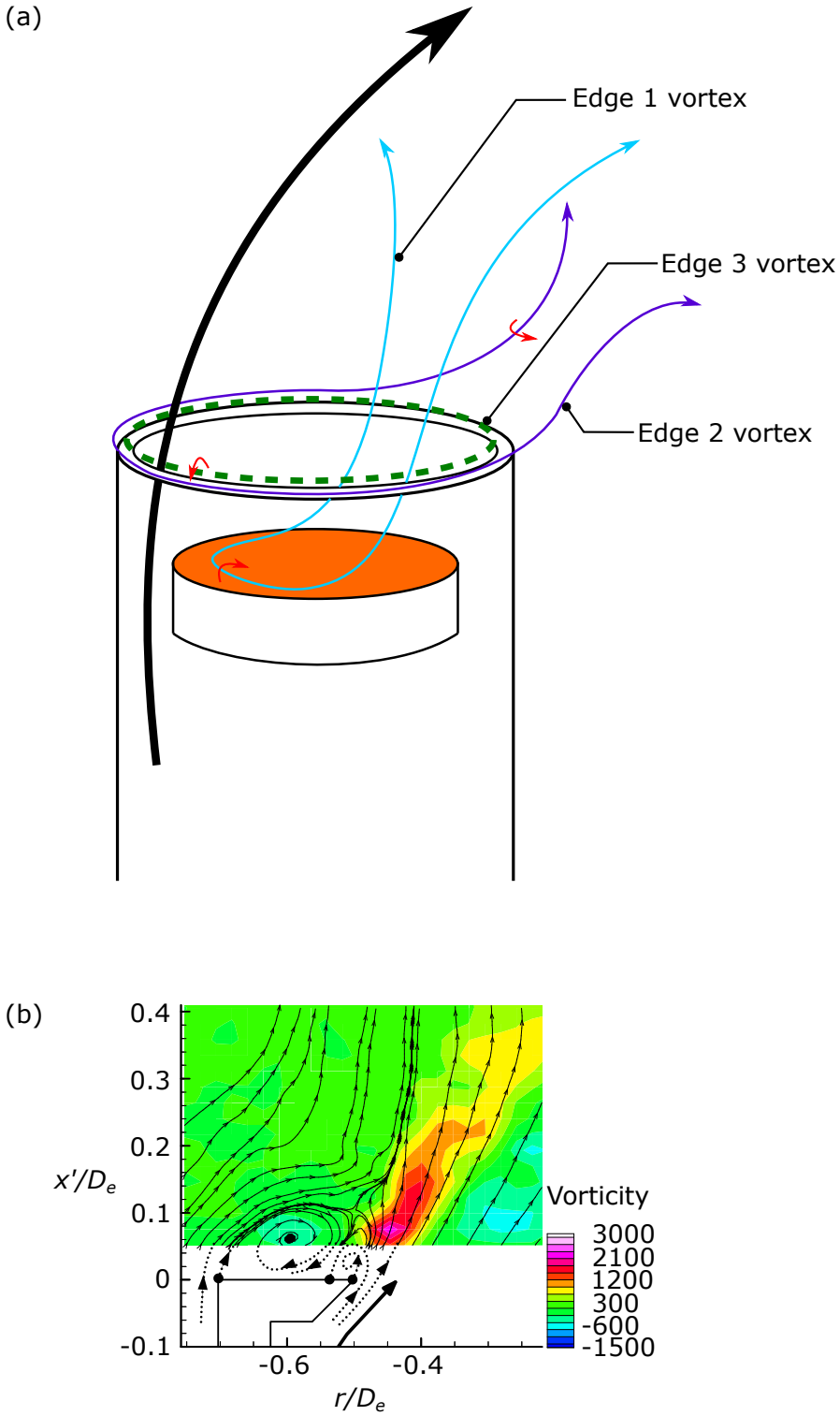

Figure 2.9: The structure of the three edge vortices downstream from the centre body (Wong et al. 2008). (a) the vortex skeleton of the three edge vortices and (b) the streamlines in the near field of the nozzle exit. Note that the dotted lines indicate the deduced Edge 3 vortex. Adopted from Wong et al. (2008)

using PIV. Three vortex cores were found to be embedded within the primary jet in the near region downstream from the inlet base and were deduced to be merged at about $x = 1.175D$. These three longitudinal vortex were also found in a simulation of the OTJ flow using LES approach (Xu et al. 2011). The calculated precession frequency was reported to be over-predicted by 14%, compared with the measured result (England et al. 2010). In addition, an unsteady k-ε model was employed to simulate a related flow downstream from a long pipe inlet into a large chamber with a similar expansion ratio to the FPJ nozzle (Guo et al. 2001). The predicted flow streamline patterns yield qualitative agreement with the related FPJ flow including the asymmetric reattachment of the jet, the recirculation zone and the swirling flow in the most upstream region of the nozzle. However, the OTJ nozzle comprises a triangular inlet orifice instead of a circular orifice for the FPJ nozzle, and the length-diameter ratio of the downstream chamber in the simulation of Guo et al. (2001) is about five times greater than that of the FPJ nozzle, the detailed flow structure of the FPJ flow is still unclear.

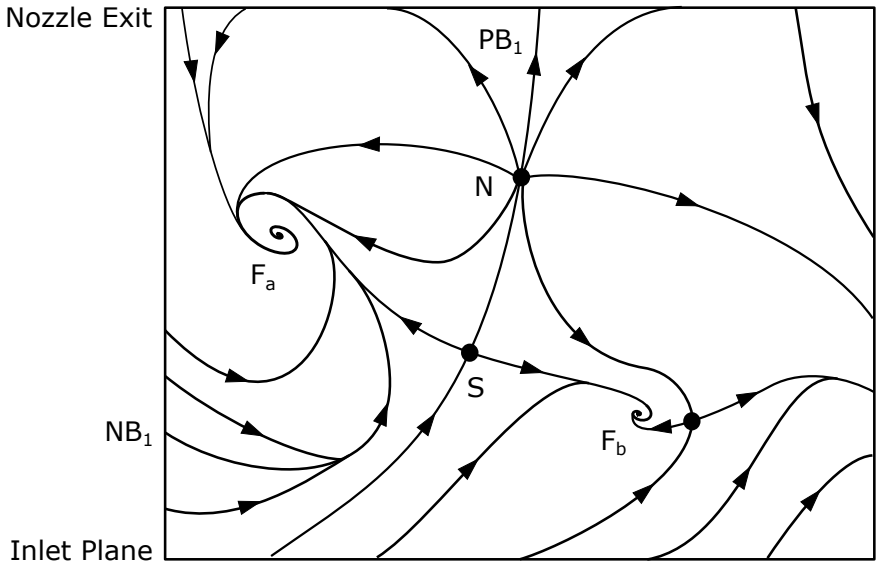

Figure 2.10: The deduced surface flow pattern of the OTJ nozzle. Adapted from Lee (2009).

2.4.3 Critical point theory

Knowledge of the flow structure is useful to explain the mechanism of the flow. For example, the structure of a round jet in cross-flow has been studied by Kelso et al. (1996). Three mechanisms that cause the vertical vortices in the wake were derived from the flow visualisations and measurements. Similarly, Perry & Hornung (1984) proposed a method to identify mechanisms that are responsible for flow behaviour from vortex skeleton model.

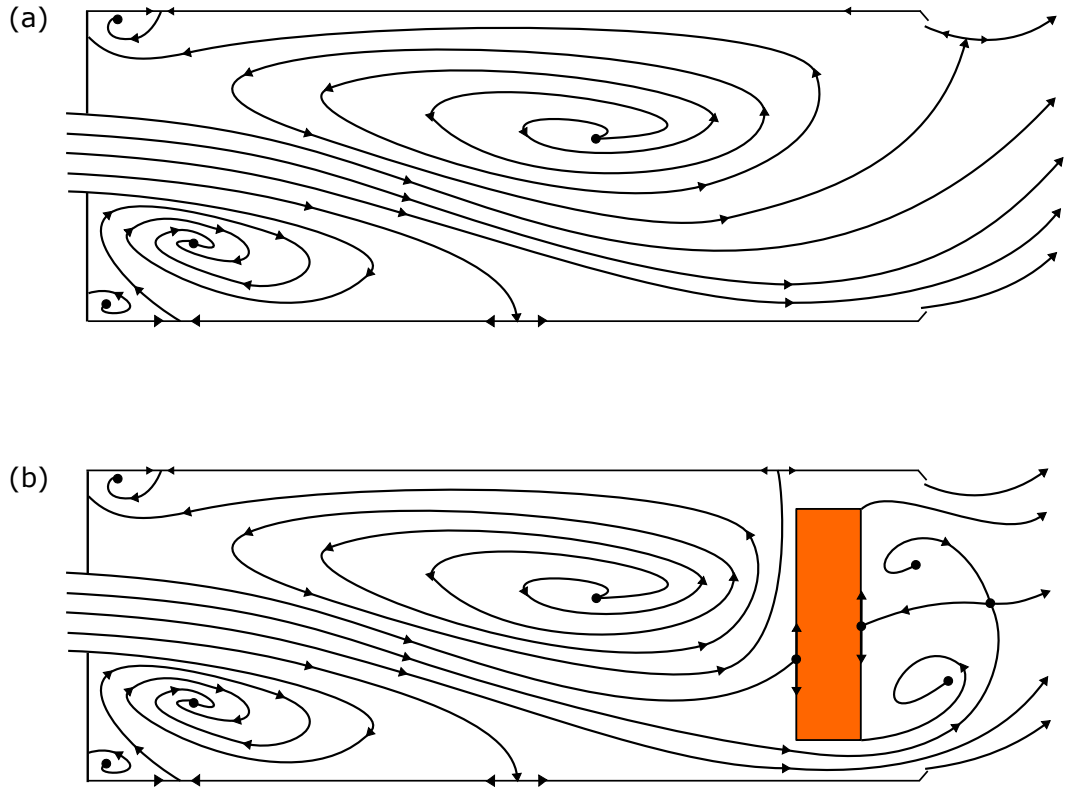

Figure 2.11: The deduced streamlines on the cross-sectional plane of (a) the OTJ nozzle and (b) the FPJ nozzle. Adapted from Lee (2009).

The "critical point theory" concept, which has been reported by Perry & Chong (1993) to be efficient at describing complex three dimensional flow patterns, has also been employed in several studies on the FPJ flow structure (Kelso 2001, Lee 2009, Wong et al. 2008) and other flows (Kelso et al. 1996, Kelso & Smits 1995, Perry & Chong 1993).

A critical point is defined as the point in the flow field where the streamline slope is indeterminate and the velocity is zero (Perry et al. 1980). The flow patterns around the critical point can be determined based on the asymptotical solution of the Navier-Stokes and continuity equations, while the remaining flow field can be deduced according to the locations and types of the critical points (Perry et al. 1980). Figure 2.12 presents the three types of flow patterns in the vicinity of the critical point, i.e. nodes, foci and saddle points, which have been detailed in the work of Perry & Chong (1987). The concepts of critical point theory were employed in a number of works (Lee 2009, Lee & Lanspeary n.d., Nathan et al. 1998, Wong et al. 2008, Wong 2004) for the flow pattern analysis and vortex skeleton development of an FPJ flow. This work will also adopted this concepts for the analysis of the flow structure.

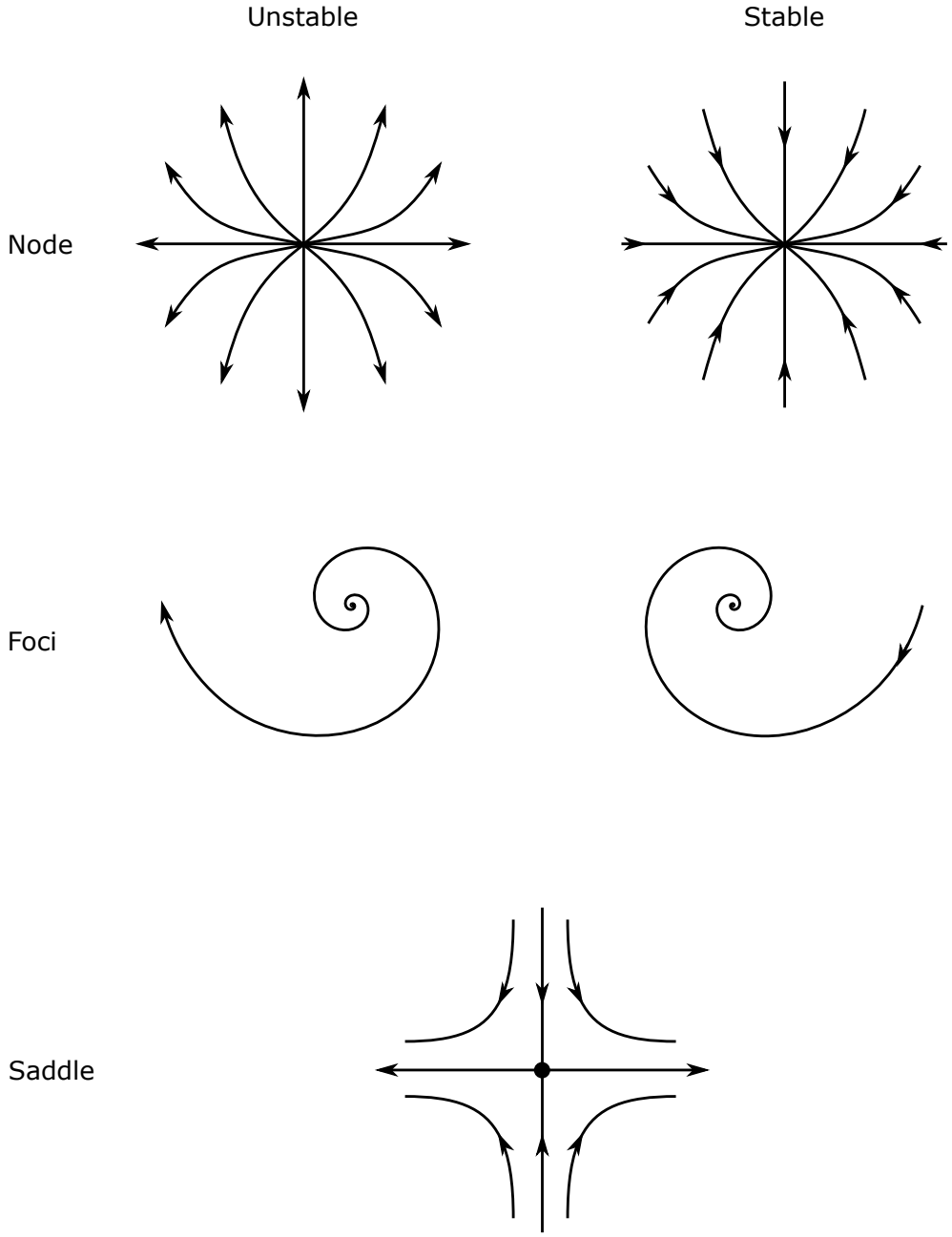

Figure 2.12: A schematic diagram of the three types of the flow patterns in the vicinity of the critical point, i.e. nodes, foci and saddle points.

It is noted that critical point theory requires first and foremost the complete agreement between the model and experiment of all of the qualitative features of the ensemble-averaged flow. It does not require perfect quantitative agreement of the velocity field, since some quantitative differences would result only in a change in the position of the critical points, which does not influence the structure of the vortex skeleton. Nevertheless, reasonable quantitative agreement between the experiments and the model is needed to ensure confidence in

the model.

2.4.4 The third aim: develop a topological structure of the ensemble-averaged FPJ flow

The instantaneous flow pattern in the work of Nathan et al. (1998) only revealed the general structure of the FPJ flow. Similarly, many important details of the instantaneous flow structure have not been assessed by Cafiero et al. (2014), such as the vortex cores and the surface flow patterns. Nathan et al. (1998) presented the flow pattern on the nozzle surface. However, this visualisation study revealed only the time-smoothed results, so that the instantaneous surface streamlines remained unmeasured. While a lot of experimental data are available (Wong et al. 2008, 2003), it is incomplete and the structure is too complex to allow a complete skeleton of the ensemble-averaged flow to be deduced without access to further information. The vortex skeleton proposed by Lee (2009) was derived from measurements of a stationary deflected triangular jet, rather than from those of an unsteady jet, so that the reliability of this model also remains to be confirmed. Furthermore, since the geometry adopted in the work of Lee (2009) is not identical to the FPJ nozzle, this deduction may not be representative of the FPJ flow. Hence the third aim of this investigation is to develop a topological structure of the ensemble-averaged FPJ flow based on critical point theory, the previous measured results of our group (Lee 2009, Lee & Lanspeary n.d., Nathan et al. 1998, Wong et al. 2008, Wong 2004) and the flow predicted with a numerical model.

2.5 Mode switching

2.5.1 Bi-stable flows

A bi-stable flow is a flow that switches spontaneously between two relatively stable flow modes. Two flow modes of the flow downstream from a periodically plunging airfoil, i.e. the vortex street is deflected up and down, were revealed based on the Laser Doppler Velocimetry (LDV) measurements and the underwater flow visualisation (Jones et al. 1998). It was found that the flow switched between the two modes randomly and the relatively small perturbations was suggested to trigger the mode switching. This bi-stable flow was also studied by Heathcote & Gursul (2007) using both LDV and PIV measurement. It was found that, instead of switching randomly, the mode switching is quasi-periodic and the switching

period is relative to the stiffness of the airfoil, the plunge frequency and the plunge amplitude. Moreover, they reported the vorticity field during the mode switching process and the visualisation of the flow in both the two modes.

The flow between two identical circular cylinders was found to be bi-stable if the ratio of the distance of the cylinders to the cylinder diameter is in the range between approximately 0.1 to 1 (Bearman & Wadcock 1973, Kim 1988). It was observed from the flow visualisation that the flow downstream from the gap between the two cylinders biased towards each cylinder intermittently (Bearman & Wadcock 1973). Kim (1988) indicated that this mode switching is randomly and the time-scale for the mode switching is much larger than that of the vortex shedding. The mode switching phenomenon was found to be ceased if a plate was placed appropriately in the middle of the two cylinders, which then led to either a stable symmetric or asymmetric flow field (Kim 1988). The flow visualization during the mode switching process was reported in the work of Mahbub Alam et al. (2003). The wake downstream from the cylinder, which the flow is biased to, is narrower and the frequency of the vortex shedding is higher than that of the other wake. An intermediate flow mode, in which the downstream flow does not bias, was also observed during the mode switching process, although its duration is relatively shorter than the other two modes.

2.5.2 The bi-stable FPJ flow

The bi-stability phenomenon of the jet through the FPJ nozzle was indicated by Nathan & Luxton (1992*a*) and Nathan & Luxton (1992*b*). The two flow modes, i.e. the precessing jet (PJ) mode and the axial jet (AJ) mode were identified by Hill et al. (1992). The main features of the flow in the PJ mode were described in the work of Nathan et al. (1998), as stated in Section 2.1. Instead of reattaching to the wall of the chamber, the flow in the AJ mode is almost axisymmetric (Nathan et al. 1998), as shown in Figure 2.13. It is reported that the FPJ flow is highly intermittent and randomly switches between the two flow modes (Hill 1992). The precession direction of the flow was also found to change randomly through a nozzle surface flow visualisation (Nathan & Luxton 1992*a*). The PJ mode is dominant and the probability that the flow is in this mode was found to be of approximately 95%, while this probability is relative to the ratio of the nozzle length to nozzle diameter (L/D) (Nathan et al. 1998). It was also found that an increase in the Reynolds number of the flow through

the nozzle inlet leads to an increase in the probability of precession (Hill 1992).

(a)

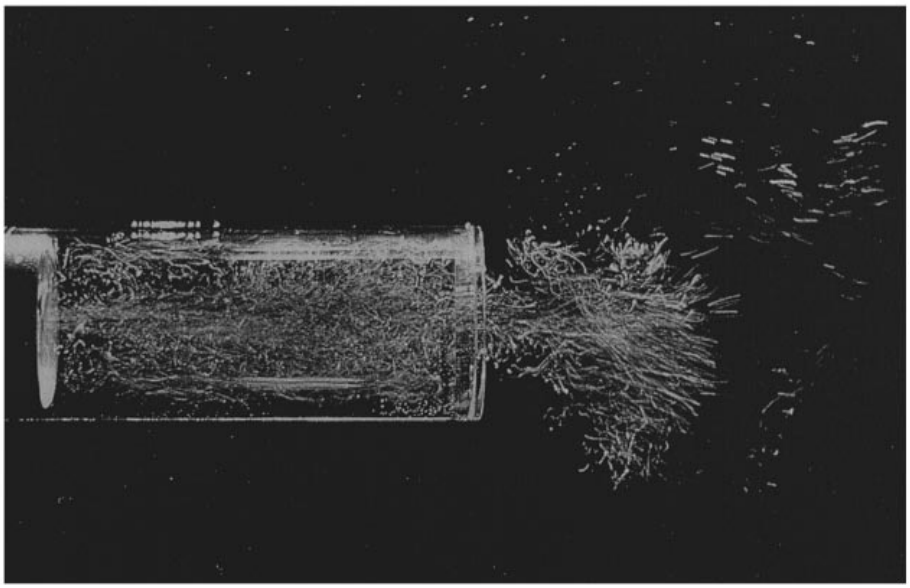

(b)

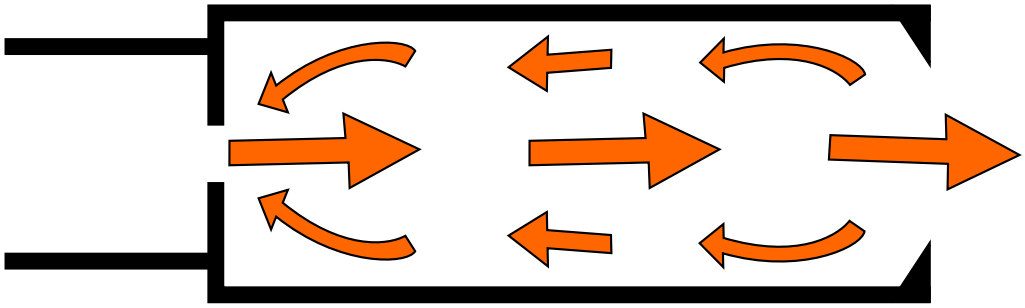

Figure 2.13: Visualization of the flow (in the AJ mode) through an FPJ nozzle that obtained from Nathan et al. (1998). (a) The surface visualization flow pattern and (b) the interpreted flow pathlines. Adapted from Nathan et al. (1998).

Swirl vanes were installed upstream from the nozzle inlet to avoid the change of the precession direction (Nathan 1988). The direction of the precession was found to be always opposite to the direction of the swirl vanes. Nathan (1988) also employ the swirl vanes to control the direction of the precession. It was found that the swirl vanes can alter the direction of the precession in a short time, which is equivalent to approximately five precession cycles (Nathan 1988).

2.5.3 The mechanism of the mode switching phenomenon of the FPJ flow

Kelso (2001) proposed that the strong stream-wise vortex embedded within the primary jet, which is caused by the imbalanced vorticity in the reattachment area, trigger the jet to switch from the AJ to the PJ modes. The nozzle surface flow pattern and the vortex skeleton of the FPJ flow have also been proposed. The main difference between the nozzle surface flow pattern of Kelso (2001) and Lee (2009) is that there are two foci in either side of the reattachment point in Lee's model, while there is no foci in Kelso's representation. However, this work did not consider the role of the centre body nor the reverse flow interacting with the back wall and generating an asymmetric swirl, which has strong angular momentum. In addition, no data are available with which to assess the validity or completeness of Kelso's proposition. The mechanism of the mode switching phenomenon was also deduced from a visualisation study of FPJ flow (Nathan et al. 1998), based on the time-averaged nozzle surface flow patterns and the images of the instantaneous flows in both the AJ and the PJ modes. The instantaneous asymmetries at the scale of the local jet entering the chamber were suggested to be responsible for inducing the flow to switch from a symmetrical initial flow to the asymmetrical precessing flow mode. Consistent with Nathan et al. (1998), the asymmetric entrainment of the jet within the nozzle chamber is deduced to be a driving force of the precession motion in an experimental work of Cafiero et al. (2014). They also indicated that the behaviour of the FPJ flow is closer to that of a swirling jet than to a steady round jet in the near field. However, to date no validation for these proposed mechanisms is available.

2.5.4 The fourth aim: provide increased understanding of the mechanism by which the flow switches from the AJ to the PJ modes

All the proposed models have not been confirmed, therefore there is a need for further investigation of the mechanisms of the mode switching. Moreover, although the structure of the FPJ flow in the PJ mode has been assessed in a few of studies (Cafiero et al. 2014, Nathan et al. 1998, Wong et al. 2008), no previous report is available of the change of the flow structure during the mode switching process. Hence the fourth aim of this work is to develop a topological model of the flow structures during the mode switching process to

provide increased understanding of the mechanism by which the flow switches from the AJ to the PJ modes. It also aims to identify the flow features that are responsible for the mode switching in the FPJ nozzle.

Chapter 3

Numerical Methodology

3.1 Geometric configuration of the FPJ nozzles

The geometric configuration of the present nozzle models were chosen to match exactly the configuration adopted in previous experiments (Parham 2000, Wong 2004), which report detailed phase-averaged data of the flow field within the FPJ nozzle and time-averaged scalar data in the external flow field. These measurements were undertaken using LDA, PIV and PLIF techniques.

The software CREO 2.0 and ANSYS/Design Modeler 16.5 were used to generate the geometrical configuration of the FPJ nozzles. Figure 3.1 presents the dimensions of the FPJ nozzles with three inlet conditions, i.e. contraction, pipe and orifice inlets, which are employed for the assessment of the URANS models in predicting the velocity field of the FPJ flow (Chapter 4), investigation of the FPJ flow structure (Chapter 6) and the mode switching phenomenon (Chapter 7). The profile of the smooth contraction (Figure 3.1a) at the inlet to the device is described by a 5th order polynomial, based on Morel's criterion (Morel 1975), with an area-based contraction ratio of 10.03:1 also following the experimental device (Wong 2004). The distance between the inlet to the contraction and the inlet to the chamber is 2.05D, here D is the diameter of the nozzle chamber, i.e. 80 mm. The geometries of the FPJ nozzles with pipe and orifice inlet are similar to that with contraction inlet, shown in Figure 3.1b and c, respectively. The dimensions of the computational domains downstream from the nozzles (Figure 3.1d) are identical for these three configurations, which are an order of magnitude larger than the nozzles themselves in both the axial and radial directions, with a diameter of 1032 mm and length of 1000 mm. These three geometries are referred to as "Geometry V".

Figure 3.2 presents the dimensions of the FPJ nozzle for the reliability assessment of both the two-equation URANS model and a Hybrid-LES approach in predicting the scalar mixing

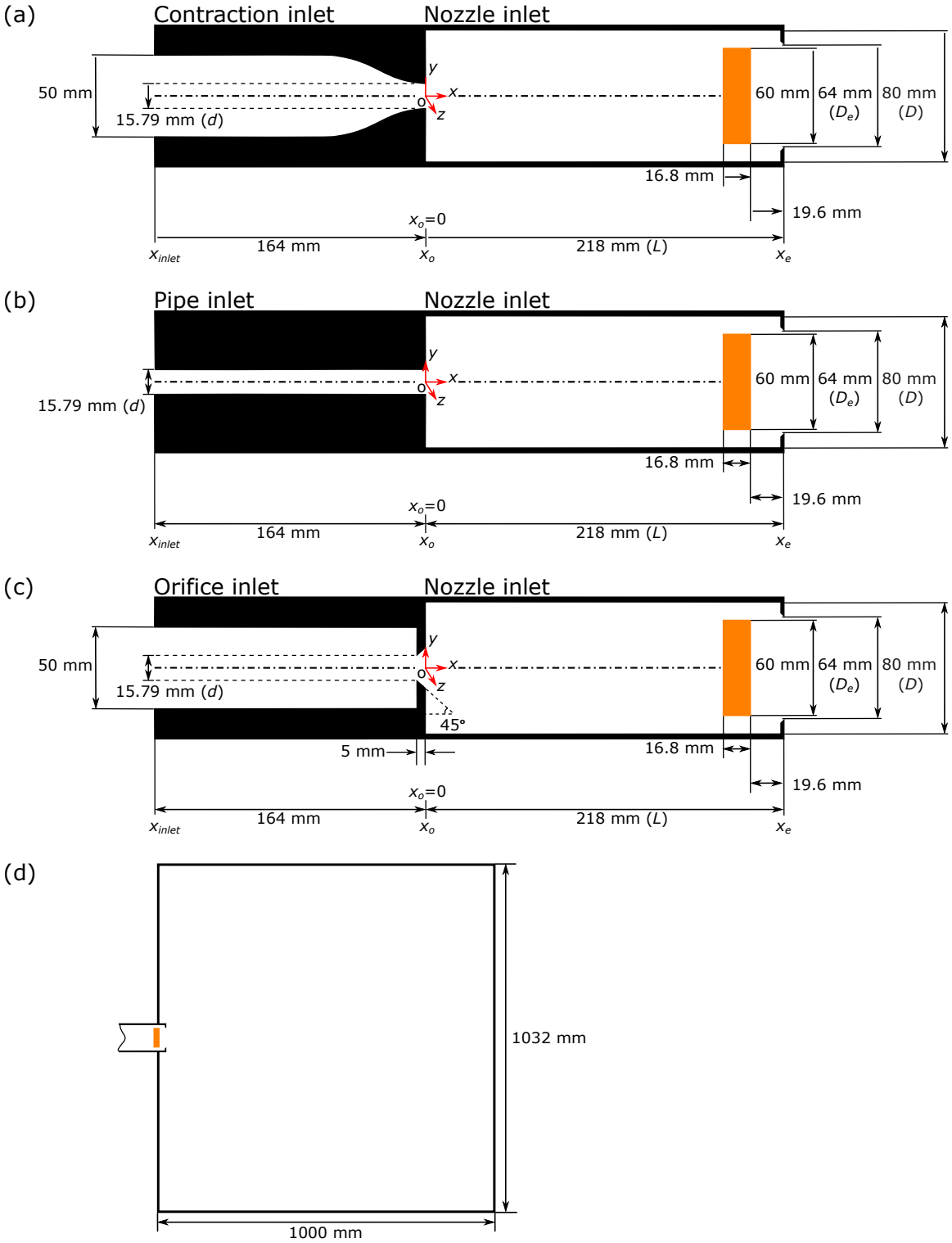

Figure 3.1: The geometries and dimensions of the fluidic precessing jet nozzles (Geometry V) adopted for the reliability assessment of the two-equation URANS models in predicting the internal velocity field, the investigation of the FPJ flow structure and the mode switching phenomenon.

of the FPJ flow (Chapter 5), which is identical to the that adopted in the work of Parham (2000). This geometry is referred to as "Geometry S". Different from the Geometry V with a contraction inlet, the diameter of the contraction is identical to that of the FPJ nozzle for the Geometry S. Moreover, the ratio of the length of the computational fluid domain outside the nozzle to the nozzle diameter for the Geometry S is much larger than that of the Geometry V.

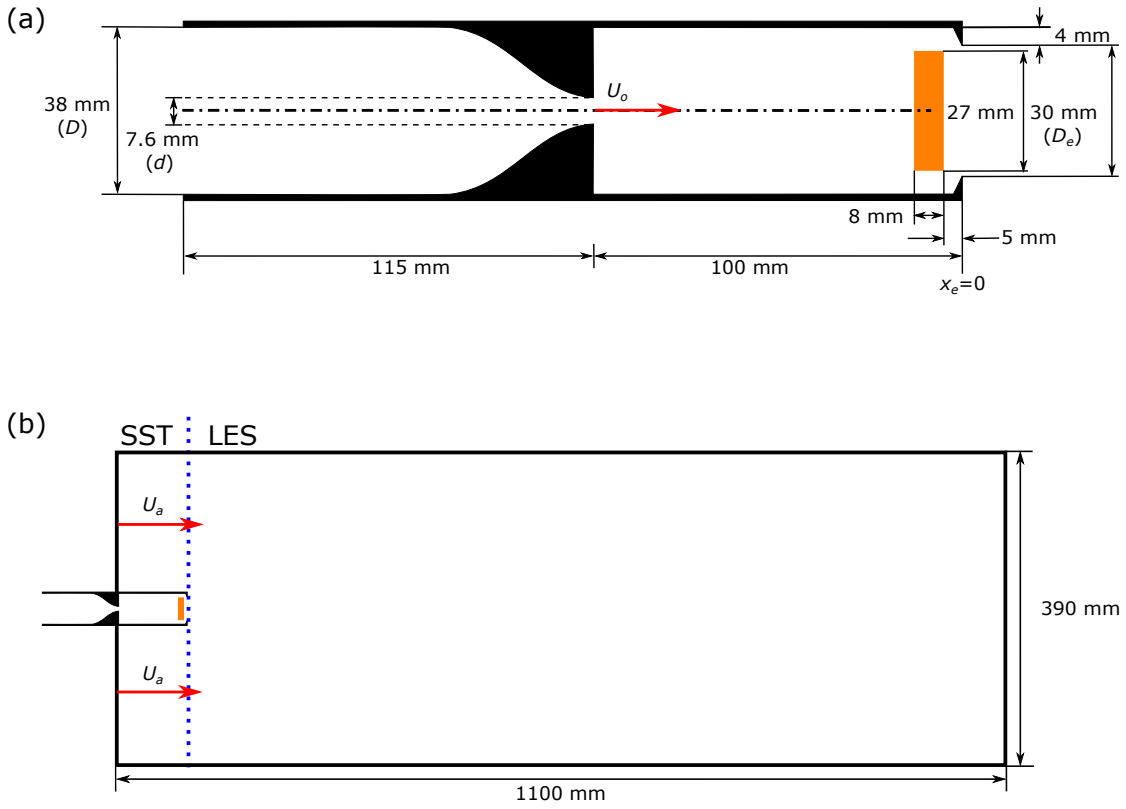

Figure 3.2: The geometries and dimensions of the fluidic precessing jet nozzles (Geometry S) adopted for the reliability assessment of a Hybrid-LES approach and the SST model in predicting the external scalar field.

3.2 Mesh generation

The software ANSYS/ICEM CFD 16.5 was employed for mesh generation. Figure 3.3 shows the structured mesh with 5.5 million nodes employed for Geometry V, here shows only the mesh for the case adopting FPJ nozzle with a contraction inlet as an example. Mesh quality near to the wall of the nozzle chamber was ensured by using the O-girds method, shown in Figure 3.3c. The maximum y^+ value for the nozzle chamber is less than 2, while the mean value of y^+ is less than 1.

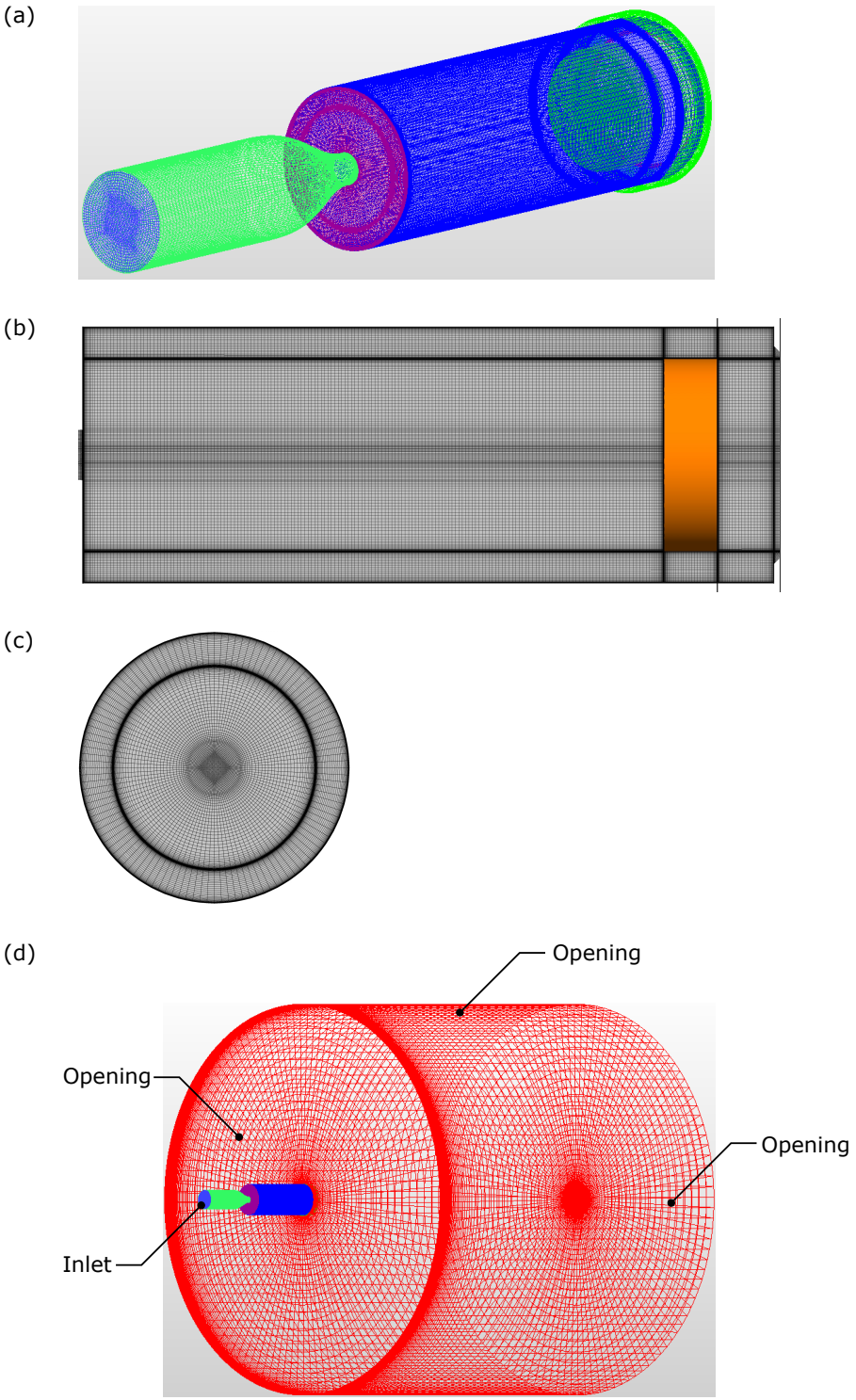

Figure 3.3: Mesh and boundary type for the FPJ nozzle (Geometry V) with a contraction inlet.

Figure 3.4 presents the details of the mesh with 8.6 million nodes for Geometry S. Similar to the mesh of Geometry V, both the structured mesh and O-grid method were adopted to ensure the mesh quality, especially in the near wall region, which makes the y^+ value to

be less than 1 (Figure 3.4b). The sensitivity of the meshes was assessed and is reported in Chapter 4 and 5.

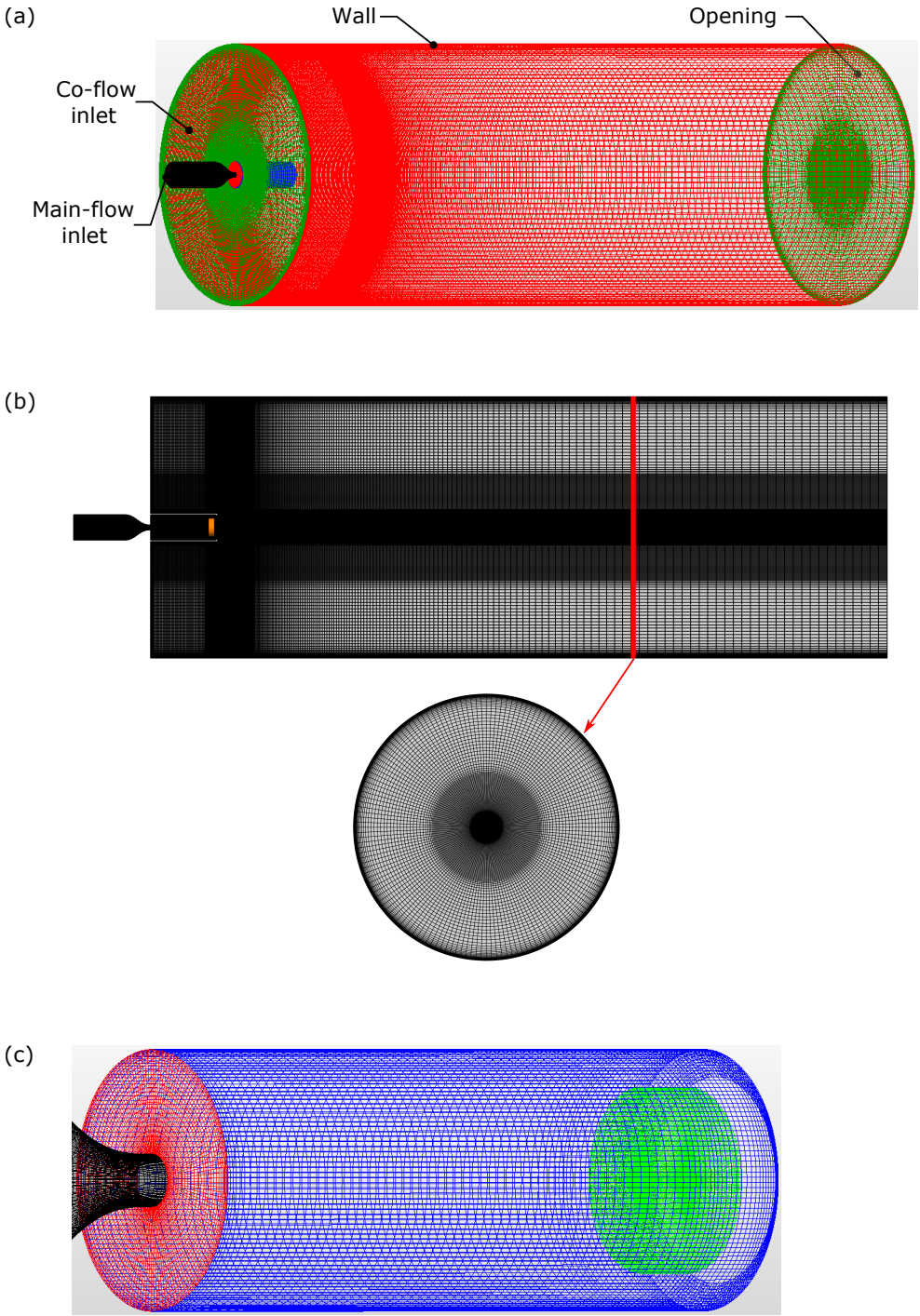

Figure 3.4: Mesh and boundary type for the FPJ nozzle (Geometry S).

3.3 Numerical configurations

Table 3.1 presents the numerical configurations of the simulations for the assessment of the two-equation URANS models in predicting the velocity field of the FPJ flow (Chapter 4), the structure of the FPJ flow (Chapter 6) and the mode switching phenomenon (Chapter 7). As both the standard k-ε model and the SST model were found to reasonably reproduce the velocity field of the FPJ flow (reported in Chapter 4), the SST model was chosen for the investigations of the flow structure and the flow mode switching phenomenon due to its superior performance in predicting wall bounded flows than the standard k-ε model (Versteeg & Malalasekera 2007). The bulk velocity at the inlet orifice of the FPJ nozzle (U_o) is 78.7 m/s for all the three configurations. Hence the velocities at the contraction, pipe and contraction inlet (U_{inlet}) are 7.81 m/s, 78.7 m/s and 6.7 m/s, respectively. The working fluid is air at 25 °C and 1 atm. A free-pressure boundary condition was chosen for the boundaries of the large computational domain downstream from the FPJ nozzle (shown in red in Figure 3.3d) with a relative pressure to ambient of 0 Pa, consistent with the experiments being performed in an unconfined environment. The adopted convective scheme is high resolution. For all the three cases reported herein, the root mean square (r.m.s) of the residuals was all less than 5×10^{-5}. The time-step in these simulations was taken to be 1/667th of the measured mean period of each precession cycle (0.13 seconds), corresponding to 0.0002 seconds. This provides about 18 time-steps in each 10° of precession. The model was allowed to run for some 27 seconds of flow time to converge to a solution that is independent of the initial condition and the data was then recorded from the subsequent 5 precession cycles. All the three simulations were conducted using a Dell PowerEdge R 815 Rack Mount Server. The wall clock time of a typical simulation is about 7 days using 16 cores.

Table 3.2 presents the numerical configurations of the simulations for the assessment of the both the SST model and the Hybrid-LES approach in predicting the external scalar field of the FPJ flow (Chapter 5). Here the SST model was chosen to keep consistent with the investigations of the internal flow structure (Chapter 6) and the mode switching phenomenon of the FPJ flow (Chapter 7). Water at 25 °C was employed as the material of the main-flow that ejected into the FPJ nozzle. A new material was defined for the co-flow, although its properties are identical to that of the main-flow. The velocity of the main-flow is 0.35 m/s

Table 3.1: Numerical configurations for the simulations adopting Geometry V.

Parameters		Details
Inlet velocity (U_{inlet})	Contraction inlet	7.81 m/s
	Pipe inlet	78.7 m/s
	Orifice inlet	6.7 m/s
Working fluid		Air at 25 °C and 1 atm
Time step		2×10^{-4} s
Convective scheme		High resolution
Transient Scheme		Second order backward Euler
Residual target (r.m.s)		5×10^{-5}
Total data		5 precession cycles
Wall clock time of each simulation		7 days

at the contraction inlet (U_i) and is 8.8 m/s at the nozzle inlet (U_o). The co-flow velocities at the confinement inlet (U_a) are 0.038 m/s, 0.06 m/s and 0.11 m/s for the assessments using the SST model, while it is 0.06 m/s for the Hybrid-LES approach. The minimum root mean square of the residuals for the convergence was set to 5×10^{-5}. The time-step was 0.001 s for the simulation using the SST model and 0.0001 s for the Hybrid-LES approach, corresponding to approximately 1/170th and 1/1700th of the period of each precession cycle. For the Hybrid-LES approach, LES was adopted to solve the flow downstream from the nozzle exit, while the SST model was employed for the other region, shown in Figure 3.2.

Table 3.2: Numerical configurations for the simulations adopting Geometry S.

Parameters	Details	
	SST	Hybrid-LES
Main flow inlet velocity (m/s)	0.35	
Co-flow inlet velocity (m/s)	0.038, 0.06, 0.11	0.06
Working fluid	Water at 25 °C	
Time step (s)	1×10^{-3}	1×10^{-4}
Convective scheme	High resolution	
Transient scheme	Second order backward Euler	
Residual target (r.m.s)	5×10^{-5}	
Total data	10 precession cycles	
Wall clock time of each simulation (days)	7	120

3.4 Mathematical approach

3.4.1 General conservation equations

The CFD calculation in the current work is based on two conservation laws of physics, namely mass and momentum conservation. The governing equations, also called Navier-Stokes equations, for an instantaneous flow are as follow:

1. The continuity equation

$$\frac{\partial \rho}{\partial t} + \nabla \cdot (\rho U) = 0 \quad ; \tag{3.1}$$

2. The momentum equation

$$\frac{\partial (\rho U)}{\partial t} + \nabla \cdot (\rho U \otimes U) = -\nabla p + \nabla \cdot \tau + S_M \quad , \tag{3.2}$$

where S_M is the momentum source and the stress tensor τ is

$$\tau = \mu \left[\nabla U + (\nabla U)^T - \frac{2}{3} \delta \nabla \cdot U \right] \quad ; \tag{3.3}$$

3.4.2 Two-equation URANS turbulence models

An averaging approach is introduced to simplify the original governing equations, which divides a quantity into an average component and a fluctuating component. Thus the Un-

steady Reynolds-Averaged Navier-Stokes equations are:

$$\frac{\partial \rho}{\partial t} + \frac{\partial}{\partial x_j}\left(\rho U_j\right) = 0 \quad , \tag{3.4}$$

and

$$\frac{\partial \rho U_i}{\partial t} + \frac{\partial}{\partial x_j}\left(\rho U_i U_j\right) = -\frac{\partial p}{\partial x_j} + \frac{\partial}{\partial x_j}\left(\tau_{ij} - \rho\overline{u_i u_j}\right) + S_M \tag{3.5}$$

The Reynolds stresses $\rho\overline{u_i u_j}$ here are unknown and can be assumed to be related to mean velocity gradients by using Boussinesq hypothesis:

$$-\rho\overline{\mu_i \mu_j} = \mu_t\left(\frac{\partial U_i}{\partial x_j} + \frac{\partial U_j}{\partial x_i}\right) - \frac{2}{3}\delta_{ij}\left(\rho k + \mu_t \frac{\partial U_k}{\partial x_k}\right) \quad , \tag{3.6}$$

where μ_t is the eddy viscosity. Hence the momentum equation for the two-euqation URANS models can be obtained by substituting the above equation into equation 3.5:

$$\frac{\partial \rho U_i}{\partial t} + \frac{\partial}{\partial x_j}\left(\rho U_i U_j\right) = -\frac{\partial p}{\partial x_i} + \frac{\partial}{x_j}\left[\mu_{eff}\left(\frac{\partial U_i}{\partial x_j} + \frac{\partial U_j}{\partial x_i}\right)\right] + S_M \quad , \tag{3.7}$$

where μ_{eff} is the effective viscosity, defined as the sum of the molecular viscosity μ and the turbulent viscosity (μ_t):

$$\mu_{eff} = \mu + \mu_t. \tag{3.8}$$

To model the turbulent viscosity, three types of two-equation URANS turbulence models were adopted and compared in their capacity to predict the unsteady FPJ flow.

3.4.2.1 The standard k-ε and modified k-ε models

For the standard k-ε model, the transport equations for the turbulent kinetic energy k and the rate of turbulence dissipation ε are:

$$\frac{\partial(\rho k)}{\partial t} + \frac{\partial}{\partial x_j}(\rho U_j k) = \frac{\partial}{\partial x_j}\left[\left(\mu + \frac{\mu_t}{\sigma_k}\right)\frac{\partial k}{\partial x_j}\right] + P_k - \rho\varepsilon \tag{3.9}$$

and

$$\frac{\partial(\rho\varepsilon)}{\partial t} + \frac{\partial}{\partial x_j}(\rho U_j \varepsilon) = \frac{\partial}{\partial x_j}\left[\left(\mu + \frac{\mu_t}{\sigma_\varepsilon}\right)\frac{\partial \varepsilon}{\partial x_j}\right] + C_{1\varepsilon}\frac{\varepsilon}{k}P_k - C_{2\varepsilon}\rho\frac{\varepsilon^2}{k} \quad , \tag{3.10}$$

where ρ is the density of the fluid, μ is the air dynamic viscosity and the turbulence viscosity (μ_t) is calculated as:

$$\mu_t = \rho C_\mu \frac{k^2}{\varepsilon} \quad . \tag{3.11}$$

The turbulence production due to viscous forces P_k is modelled using:

$$P_k = \mu_t\left(\frac{\partial U_i}{\partial x_j} + \frac{\partial U_j}{\partial x_i}\right)\frac{\partial U_i}{\partial x_j} - \frac{2}{3}\frac{\partial U_k}{\partial x_k}\left(3\mu_t\frac{\partial U_k}{\partial x_k} + \rho k\right) \quad . \tag{3.12}$$

The value of the five empirical constants: $C_\mu, \sigma_k, \sigma_\varepsilon, C_{1\varepsilon}$ and $C_{2\varepsilon}$ in the standard k-ε model are listed in Table 3.3.

Table 3.3: Values of empirical constants in the standard k-ε model (Versteeg & Malalasekera 2007).

Constants	C_μ	σ_k	σ_ε	$C_{1\varepsilon}$	$C_{2\varepsilon}$
Standard k-ε model	0.09	1.00	1.30	1.44	1.92
Modified k-ε model (1.3)	0.09	1.00	1.30	1.30	1.92
Modified k-ε model (1.6)	0.09	1.00	1.30	1.60	1.92

3.4.2.2 The RNG k-ε model

The transport equations for k and ε in the RNG k-ε model are given as follows:

$$\frac{\partial(\rho k)}{\partial t} + \frac{\partial}{\partial x_j}(\rho U_j k) = \frac{\partial}{\partial x_j}\left[\left(\mu + \frac{\mu_t}{\sigma_{kRNG}}\right)\frac{\partial k}{\partial x_j}\right] + P_k - \rho\varepsilon \tag{3.13}$$

and

$$\frac{\partial(\rho\varepsilon)}{\partial t} + \frac{\partial}{\partial x_j}(\rho U_j \varepsilon) = \frac{\partial}{\partial x_j}\left[\left(\mu + \frac{\mu_t}{\sigma_{\varepsilon RNG}}\right)\frac{\partial \varepsilon}{\partial x_j}\right] + C_{1\varepsilon RNG}\frac{\varepsilon}{k}P_k - C_{2\varepsilon RNG}\rho\frac{\varepsilon^2}{k} \quad . \tag{3.14}$$

Different from the standard k-ε model, the constant $C_{1\varepsilon}$ is replaced by $C_{1\varepsilon RNG}$:

$$C_{1\varepsilon RNG} = 1.42 - f_\eta \quad , \tag{3.15}$$

where

$$f_\eta = \frac{\eta\left(1 - \frac{\eta}{4.38}\right)}{1 + \beta_{RNG}\eta^3} \quad , \tag{3.16}$$

$$\eta = \sqrt{\frac{P_k}{\rho\varepsilon C_{\mu RNG}}} \tag{3.17}$$

and where β_{RNG} is 0.012.

The values of the other constants are listed in Table 3.4 (Versteeg & Malalasekera 2007).

Table 3.4: Values of empirical constants in the RNG k-ε model (Versteeg & Malalasekera 2007).

Constants	$C_{\mu RNG}$	σ_{kRNG}	$\sigma_{\varepsilon RNG}$	$C_{2\varepsilon RNG}$
RNG k-ε model	0.0845	0.7179	0.7179	1.68

3.4.2.3 The SST model

The SST model, developed by Menter (1992), is a hybrid between the standard k-ε model, which it employs in the flow region faraway from wall, and the k-ω model, which is employed in the near-wall region. This is because the standard k-ε model is more robust in the regions away from the near wall, although its performance in the near-wall region is not satisfactory, while the k-ω model, performs well in the near-wall region, but requires an assumed free stream value of turbulent frequency, ω, that influences the simulation result (Menter 1992, Versteeg & Malalasekera 2007). The transport equations of k and ω in the k-ω model are shown in Equation 3.18 and 3.19, while $\omega = \varepsilon/k$. The values of the empirical constants in the k-ω model are listed in Table 3.5.

$$\frac{\partial(\rho k)}{\partial t} + \frac{\partial}{\partial x_j}(\rho U_j k) = \frac{\partial}{\partial x_j}\left[\left(\mu + \frac{\mu_t}{\sigma_{k1}}\right)\frac{\partial k}{\partial x_j}\right] + P_k - \beta'\rho k\omega \tag{3.18}$$

and

$$\frac{\partial(\rho \omega)}{\partial t} + \frac{\partial}{\partial x_j}(\rho U_j \omega) = \frac{\partial}{\partial x_j}\left[\left(\mu + \frac{\mu_t}{\sigma_{\omega}}\right)\frac{\partial \omega}{\partial x_j}\right] + \alpha\frac{\omega}{k}P_k - \beta\rho\omega^2 \tag{3.19}$$

Table 3.5: Values of empirical constants in the present k-ω model (Versteeg & Malalasekera 2007).

Constants	β'	α	β	σ_{k1}	σ_{ω}
k-ω model	0.09	5/9	0.075	2	2

In the SST model, the k-equation (Equation 3.20) is the same as in k-ω model, while the ε-equation is similar to the ω-equation in the k-ω model, with the substitution $\varepsilon = k\omega$. The transformed equations of k and ω are shown below:

$$\frac{\partial(\rho k)}{\partial t} + \frac{\partial}{\partial x_j}(\rho U_j k) = \frac{\partial}{\partial x_j}\left[\left(\mu + \frac{\mu_t}{\sigma_{k2}}\right)\frac{\partial k}{\partial x_j}\right] + P_k - \beta'\rho k\omega \tag{3.20}$$

and

$$\frac{\partial(\rho \omega)}{\partial t} + \frac{\partial}{\partial x_j}(\rho U_j \omega) = \frac{\partial}{\partial x_j}\left[\left(\mu + \frac{\mu_t}{\sigma_{\omega 1}}\right)\frac{\partial \omega}{\partial x_j}\right] + 2\rho\frac{1}{\sigma_{\omega 1}\omega}\frac{\partial k}{\partial x_j}\frac{\partial \omega}{\partial x_j} + \alpha_1\frac{\omega}{k}P_k - \beta_1\rho\omega^2 \tag{3.21}$$

The k and ω equations in the SST model are obtained by adding the transformed k-ε equations (Equation 3.20 and 3.21) multiplied by a function 1-F_1 to the k-ω model equations (Equation 3.18 and 3.19) multiplied by a function F_1:

$$\frac{\partial(\rho k)}{\partial t} + \frac{\partial}{\partial x_j}(\rho U_j k) = \frac{\partial}{\partial x_j}\left[\left(\mu + \frac{\mu_t}{\sigma_{k2}}\right)\frac{\partial k}{\partial x_j}\right] + P_k - \beta'\rho k\omega \tag{3.22}$$

and

$$\begin{aligned}\frac{\partial(\rho\omega)}{\partial t}+\frac{\partial}{\partial x_j}(\rho U_j\omega) =& \frac{\partial}{\partial x_j}\left[\left(\mu+\frac{\mu_t}{\sigma_{\omega 1}}\right)\frac{\partial\omega}{\partial x_j}\right] \\ &+(1-F_1)2\rho\frac{1}{\sigma_{\omega 1}\omega}\frac{\partial k}{\partial x_j}\frac{\partial\omega}{\partial x_j}+\alpha_1\frac{\omega}{k}P_k-\beta_1\rho\omega^2 \quad ,\end{aligned} \tag{3.23}$$

where

$$F_1 = tanh\left(arg_1^4\right) \tag{3.24}$$

and where

$$arg_1 = min\left(max\left(\frac{\sqrt{k}}{\beta'\omega y},\frac{500\nu}{y^2\omega}\right),\frac{4\rho k}{CD_{k\omega}\sigma_{\omega 1}y^2}\right) \tag{3.25}$$

and

$$CD_{k\omega} = max\left(2\rho\frac{1}{\sigma_{\omega 1}\omega}\frac{\partial k}{\partial x_j}\frac{\partial\omega}{\partial x_j},1.0\times10^{-10}\right) \tag{3.26}$$

Different from the standard k-ε and k-ω model, the turbulent viscosity is given as:

$$\mu_t = \frac{\alpha\rho k}{max(\alpha\omega,SF_2)} \quad , \tag{3.27}$$

where S=$\sqrt{2S_{ij}S_{ij}}$ and

$$F_2 = tanh(arg_2^3) \tag{3.28}$$

with

$$arg_2 = max\left(\frac{2\sqrt{k}}{\beta'\omega y},\frac{500\nu}{y^2\omega}\right) \quad . \tag{3.29}$$

The value of the constants employed in the SST model are listed in Table 3.6 (Versteeg & Malalasekera 2007).

Table 3.6: Values of empirical constants in the SST model (Versteeg & Malalasekera 2007).

Constants	β'	α	α_1	β_1	σ_{k2}	$\sigma_{\omega 1}$
SST model	0.09	5/9	0.44	0.0828	1	1/0.856

To address the limitation of the eddy-viscosity models in poor prediction of the influence of streamline curvature and system rotation (Smirnov & Menter 2009), the correction to on the production term P_k of Shur et al. (2000) was adopted. The new $P_{k\text{-}c}$ is defined as:

$$P_{k\text{-}c} = P_k \cdot f_r \quad , \tag{3.30}$$

where

$$f_r = max(0, 1 + C_{scale}(\tilde{f}_r - 1)) \tag{3.31}$$

and

$$\tilde{f}_r = max(min(f_{rotation}, 1.25), 0) \quad . \tag{3.32}$$

The function $f_{rotation}$ is given as:

$$f_{rotation} = (1 + c_{r1}) \frac{2r^*}{1 + r^*} \left[1 - c_{r3} tan^{-1}(c_{r2}\tilde{r})\right] - c_{r1} \quad , \tag{3.33}$$

where

$$r^* = \frac{s}{\Omega} \tag{3.34}$$

and

$$\tilde{r} = 2\Omega_{jk} S_{jk} \left[\frac{DS_{ij}}{Dt} + (\varepsilon_{imn} S_{jn} + \varepsilon_{jmn} S_{in}) \Omega_m^{rot} \right] \frac{1}{\Omega D^3} \quad . \tag{3.35}$$

Here

$$S_{ij} = \frac{1}{2} \left(\frac{\partial u_i}{\partial x_j} + \frac{\partial u_j}{\partial x_i} \right) \quad , \tag{3.36}$$

$$\Omega_{ij} = \frac{1}{2} \left[\left(\frac{\partial u_i}{\partial x_j} - \frac{\partial u_j}{\partial x_i} \right) + 2\varepsilon_{mji} \Omega_m^{rot} \right] \quad , \tag{3.37}$$

$$S^2 = 2S_{ij} S_{ij} \quad , \tag{3.38}$$

$$\Omega^2 = 2\Omega_{ij} \Omega_{ij} \quad , \tag{3.39}$$

and

$$D^2 = max\left(S^2, 0.09\omega^2\right) \quad . \tag{3.40}$$

Here $\frac{DS_{ij}}{Dt}$ are the components of the Lagrangian derivative of the strain rate tensor, while the constant C_{r1}, C_{r2}, C_{r3} are equal to 1, 2 and 1, respectively. The scale coefficient C_{scale} is set to 1 in this study.

3.4.3 Large Eddy Simulation

Different from the URANS models, the time-dependent Navier-Stokes equations are filtered spatially based on the grid spacing for an LES approach. The relatively larger eddies are computed, while the smaller eddies are filtered out and their effects on the resolved flow are captured by a subgrid-scale (SGS) model (Versteeg & Malalasekera 2007).

According to ANSYS Academic Research (2015), a quantity ϕ can be expressed as the sum of the filtered variable ($\bar{\phi}(x)$) and the unresolved part (ϕ'):

$$\phi = \bar{\phi}(x) + \phi' \quad . \tag{3.41}$$

The filtered variable is defined as:

$$\bar{\phi}(x) = \int_{FD} \phi(x') G(x;x') dx' \quad , \tag{3.42}$$

here FD is the fluid domain and G is the filter function, defined as:

$$G(x;x') = \begin{cases} 1/V, & \text{if } x' \in V \\ 0, & \text{otherwise} \end{cases} \quad , \tag{3.43}$$

where V is the control volume. Hence the following equation can be obtained by discretizing the fluid domain into finite volumes implicitly:

$$\overline{\phi}(x) = \frac{1}{V} \int_V \phi\left(x'\right) dx', x' \in V \quad . \tag{3.44}$$

Thus the filtered continuity equation is identical to Equation :

$$\frac{\partial \rho}{\partial t} + \nabla \cdot (\rho U) = 0 \quad , \tag{3.45}$$

while the filtered momentum equation is:

$$\frac{\partial}{\partial t}\left(\overline{\rho}\overline{U}_i\right) + \frac{\partial}{\partial x_j}\left(\overline{\rho}\overline{U}_i\overline{U}_j\right) = -\frac{\partial \overline{p}}{x_i} + \frac{\partial}{\partial x_j}\left[\mu\left(\frac{\partial \overline{U}_i}{\partial x_j} + \frac{\partial \overline{U}_j}{\partial x_i}\right)\right] + \frac{\partial \tau_{ij}}{\partial x_j} \quad , \tag{3.46}$$

where τ_{ij} is the subgrid-scale stress and is defined as:

$$\tau_{ij} = -\overline{\rho U_i U_j} + \overline{\rho}\overline{U}_i\overline{U}_j \quad . \tag{3.47}$$

Here the subgrid-scale stress can be associated with the large scale strain rate tensor ($\overline{S}_{ij}$) using an eddy viscosity approach:

$$\tau_{ij} - \frac{1}{3}\delta_{ij}\tau_{kk} = 2\mu_{sgs}\overline{S}_{ij} \quad , \tag{3.48}$$

where

$$\overline{S}_{ij} = \frac{1}{2}\left(\frac{\partial \overline{U}_i}{\partial x_j} + \frac{\partial \overline{U}_j}{\partial x_i}\right) \quad . \tag{3.49}$$

The Smagorinsky model (Smagorinsky 1963) is employed to estimate the SGS viscosity (μ_{sgs}), which can be related to the length scale of the unresolved eddies (l), density of the fluid (ρ) and the velocity of the unresolved eddies (q_{sgs}):

$$\mu_{sgs} \propto \rho l q_{sgs} \quad . \tag{3.50}$$

The velocity of the unresolved eddies can be related to filtered velocity by using the Prandtl mixing length model:

$$q_{sgs} = \Delta \left|\overline{S}\right| \quad , \tag{3.51}$$

where $\left|\overline{S}\right|$ is:

$$\left|\overline{S}\right| = \left(2\overline{S}_{ij}\overline{S}_{ij}\right)^{\frac{1}{2}} \quad , \tag{3.52}$$

and Δ is the grid size. Hence the SGS viscosity can be expressed as:

$$\mu_{sgs} = \rho \left(C_S \Delta\right)^2 \left|\overline{S}\right| \quad , \tag{3.53}$$

where C_S is the Smagorinsky constant and adopts a value of 0.1 for the current work.

In the near wall region, the wall damping for the SGS viscosity can be calculated as:

$$\mu_{sgs} = \rho min\left(l_{mix}, f_\mu C_S \Delta\right)^2 \left|\overline{S}\right| \quad . \tag{3.54}$$

The damping function f_μ is 1 and the mixing length function l_{mix} is:

$$l_{mix} = \kappa \cdot y_{wall} \quad , \tag{3.55}$$

where the value of the constant κ is 0.4 and y_{wall} is the wall distance.

3.5 Phase averaging method

Following the experimental investigation (Wong 2004), a monitor point (MP1 in Figure 3.5) in the flow was chosen to assess the time-varying oscillations of the flow at r=30 mm and x_o=209.2 mm. The phase-averaged flow field was calculated using Matlab in phase-bins of 36 time-space steps in each precession cycle, corresponding to 10° of spatial domain to match exactly the criteria reported from the experiments (Wong 2004). The detailed processing procedures used in this study are as follow:

1. Plot the axial velocity (u) at point MP1 (shown in Figure 3.5) as a function of time and determine the start and end time of each precession cycle based on the peak value of u;

2. Export the axial velocity (u) on a series of cross-sectional planes within and in the near field of the FPJ nozzle from the start time of the first cycle to the end time of the last cycle;

3. Divide the phase of each cycle into 36 time-intervals, each corresponding to a ten-degree span of phase angles, to total 360 for the whole cycle;

4. Take the average of the velocity data binned with each ten-degree arc of the precession cycle, which results in 36 velocity values corresponding to the 36 ten-degree-range;

5. "Rotate" the coordinate of the nodes in the other phase-bins to match the nodes in phase-bin 1. Employ the interpolation method to estimate the axial velocity if the location of the "rotated" nodes does not match that in phase-bin 1;

6. Take the average of u to obtain the phase-averaged flow field.

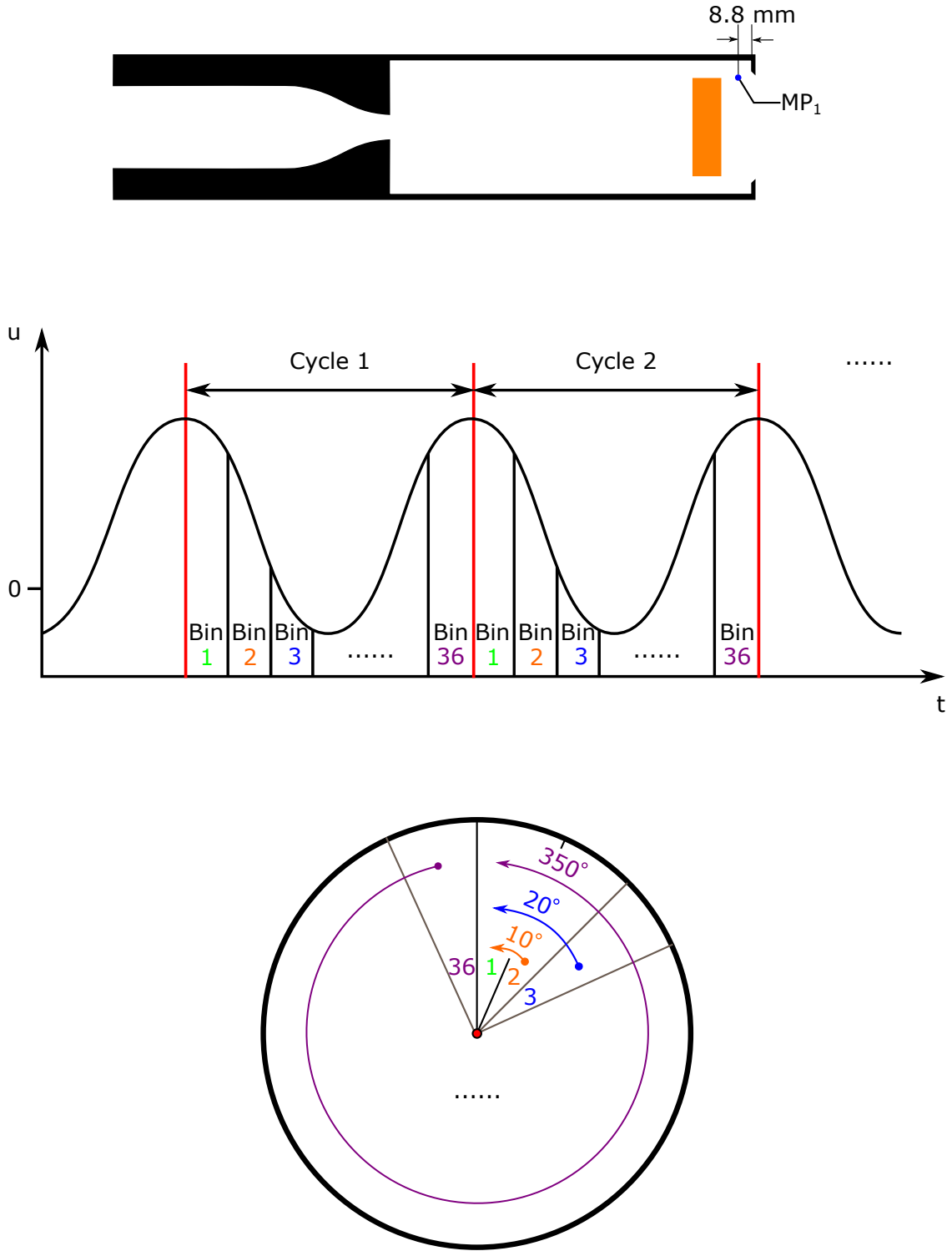

Figure 3.5: A schematic diagram of the phase-averaging method.

3.6 Methods to trigger mode switching

Three methods to trigger the flow to switch from the AJ to the PJ modes were assessed to study the mode switching phenomenon of the FPJ flow (Chapter 7) and are described below.

Note that, to simulate the FPJ flow (Chapter 4, 5 and 6), the next step after triggering the mode switching would then be employed for any of the three methods below of reverting to a symmetrical inlet flow with the FPJ flow-field for the initial flow.

3.6.1 Approach A: continuous axial perturbation

The first method (Approach A) chosen to switch the flow from the AJ to the PJ modes was to impose a random axial perturbation to part of the inlet flow. The FPJ nozzle with a pipe inlet was adopted in this section (Figure 3.1b). The first step in this process is to establish the axisymmetric AJ mode by employing an axisymmetric inflow. This AJ flow was then employed as the initial flow field for the second step. Continuous random perturbations with intensity in the ranges from 0% to 5%, 0% to 15%, 0% to 25%, 0% to 50%, 0% to 100% and 0% to 200% were then imposed on one part of the inflow at the pipe inlet (x_{inlet}) until such time as flow switched modes to the FPJ flow. Here the perturbation intensity is defined as the ratio between the maximum imposed perturbation and the bulk velocity at x_{inlet}. As shown in Figure 3.6, the area of the adopted perturbation zone (A_{pz}) was $A_{pipe}/8$, $A_{pipe}/4$, $A_{pipe}/2$ and A_{pipe}, where A_{pipe} is the cross-sectional area of the inflow at x_{inlet}.

3.6.2 Approach B: continuous tangential velocity component

The second method (Approach B) employed to switch the flow from the AJ to the PJ modes was that of imposing a continuous tangential velocity component to the inflow until such time as flow has switched modes to the FPJ flow. The FPJ nozzle with a contraction inlet was adopted for this assessment (Figure 3.1a) together with the same AJ flow initial flow field as in Approach A. A cylindrical coordinate system was employed and the radial component (v_r) at the contraction inlet was set to zero, while the tangential component (v_θ) was systematically varied to be a constant fraction (0%, 20%, 30% or 40%) of the axial component, shown in Figure 3.7.

3.6.3 Approach C: slightly asymmetric initial flow field

The third method (Approach C) employed to trigger the mode switching was to adopt a slightly asymmetric initial flow field. The FPJ nozzle with a contraction inlet was employed here. Unlike the first two methods, the flow at the contraction inlet (x_{inlet}) is axisymmetric, so that it is only the initial flow-field that is asymmetric. Three slightly asymmetric flows

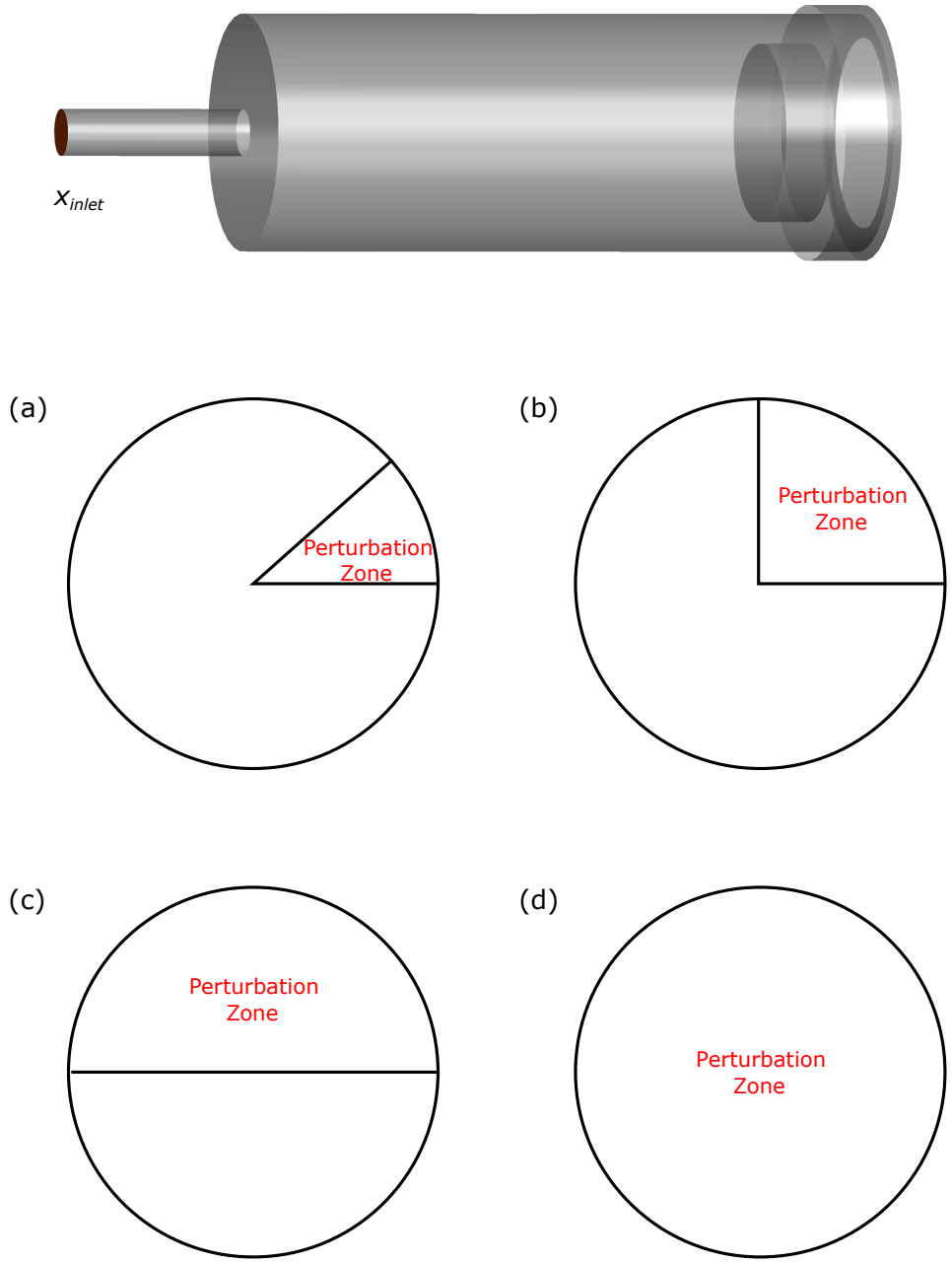

Figure 3.6: Sketch of the alternative perturbation zones within the inflows at the pipe inlet (x_i) that were used to initiate precession, i.e. A_{pz}/A_{pipe}= (a) 1/8, (b) 1/4, (c) 1/2 and (d) 1. Note that A_{pz} is the area of the perturbation zone and A_{pipe} is the area of the pipe inlet.

from the result of one case in Approach B were adopted here as the initial flow field and one case in this approach was adopted as an example to present the flow structure during the mode switching process.

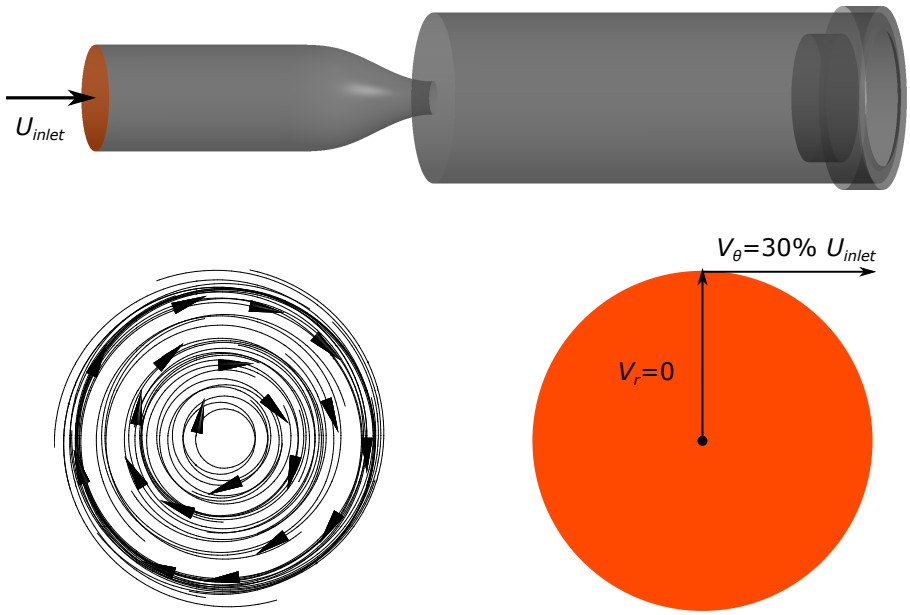

Figure 3.7: The streamlines on the contraction inlet with an imposed tangential velocity of 30% of the U_{inlet}.

Chapter 4

Assessment of the reliability of two-equation URANS models in predicting a precessing flow

Statement of Authorship

Title of Paper	Assessment of the reliability of two-equation URANS models in predicting a precessing flow
Publication Status	☐ Published ☐ Accepted for Publication ☑ Submitted for Publication ☐ Unpublished and Unsubmitted w ork w ritten in manuscript style
Publication Details	Chen, X., Tian, Z. F., and Nathan, G. J., 2017, "Assessment of the reliability of two-equation URANS models in predicting a precessing flow," Submitted to Journal of Fluids Engineering.

Principal Author

Name of Principal Author (Candidate)	Xiao Chen
Contribution to the Paper	Conducted literature review, developed CFD model, performed data processing and analysis, and wrote manuscript.
Overall percentage (%)	65
Certification:	This paper reports on original research I conducted during the period of my Higher Degree by Research candidature and is not subject to any obligations or contractual agreements with a third party that would constrain its inclusion in this thesis. I am the primary author of this paper.
Signature	Date 31.05.2017

Co-Author Contributions

By signing the Statement of Authorship, each author certifies that:

i. the candidate's stated contribution to the publication is accurate (as detailed above);

ii. permission is granted for the candidate in include the publication in the thesis; and

iii. the sum of all co-author contributions is equal to 100% less the candidate's stated contribution.

Name of Co-Author	Zhao Tian
Contribution to the Paper	Supervised CFD model developing, helped in data interpreting and edit manuscript.
Signature	Date 31/05/17

Name of Co-Author	Graham Nathan
Contribution to the Paper	Supervised development of work, helped in data interpreting and edit manuscript.
Signature	Date 31/5/17

Please cut and paste additional co-author panels here as required.

Assessment of the reliability of two-equation URANS models in predicting a precessing flow

Xiao Chen, Zhao F. Tian, Graham J. Nathan*

School of Mechanical Engineering

Centre for Energy Technology (CET)

The University of Adelaide

Adelaide, South Australia, 5005

Australia

*Corresponding author. Email: graham.nathan@adelaide.edu.au.

Abstract

A systematic numerical study and comprehensive validation against experimental data of the complex flow through a suddenly expanding axisymmetric chamber is reported. To assess the strengths and limitations of unsteady Reynolds-Averaged Navier-Stokes (URANS) models in predicting the velocity field of this flow, five types of URANS models, namely the standard k-ε model, the modified k-ε (1.6) model, the modified k-ε (1.3) model, the Re-Normalisation Group (RNG) k-ε model and the Shear Stress Transport (SST) model were adopted. Good agreement with the flow features and reasonable agreement with the measured phase-averaged velocity field, energy of total fluctuation and precession frequency can be achieved with both the standard k-ε and the Shear Stress Transport (SST) models. The degree of accuracy in predicting the rate of both spreading and velocity decay of the jet was found to greatly influence the prediction of the precession motion.

1 Introduction

The fluidic precessing jet (FPJ) nozzle, which was first proposed by Nathan and Luxton [1], has been widely investigated [2] because it offers the potential to reduce NO_x emissions, reduce fuel consumption and improve product quality from rotary kilns [3, 4, 5]. These data and understanding form the basis on which current FPJ nozzle designs are based. However, because each rotary kiln is typically different, it is desirable to employ numerical models such as Computational Fluid Dynamics (CFD) models to optimise the design of the flow and mixing field for each and every application. For industrial design tools, it is desirable for such designs to be performed with two-equation URANS turbulence models, owing to

the very large computation cost associated with modelling firstly the very large physical scale of these devices, which are typically of the order 100 m in length [2], and, secondly, with the unsteady nature of the FPJ flows that requires transient modelling. The overall aim of the present investigation is therefore to assess the potential of two-equation URANS models to model the unsteady, precessing flow in, and from, the FPJ nozzle.

The FPJ nozzle comprises an axisymmetric chamber with a large sudden expansion at the inlet and a lip at the exit, together with a centre body (CB), to increase the probability of generating the precession motion. The inlet to the chamber can be fed either from a smooth contraction, a pipe or an orifice plate. Nathan et al. [6] have summarised four dominant features of the FPJ flow, as described below. These flow features are also adopted as the qualitative criteria against which we assess whether or not the precession motion has been predicted in the current work. These features of FPJ flow, also shown in Figure 1, are [6]:

1. an unsteady and asymmetrical reattachment of the flow onto the wall after entering into the chamber;

2. a recirculating flow region diametrically opposite to the reattaching jet;

3. a swirling flow in the most upstream part of the nozzle chamber;

4. a deflected external jet emerging from the exit of the nozzle.

To develop reliable models of this flow is a significant challenge, not only because of the large scale and unsteady nature of FPJ flows, but also because this flow combines several complex features, each of which is difficult to model, namely oscillations, swirl, flow separation and flow impingement [6]. In the many

two-equation RANS models, the standard k-ε model, the Re-Normalisation Group (RNG) k-ε model and the Shear Stress Transport (SST) model are widely used in modelling industrial flows. The general validity of the RNG k-ε model has been a matter of some controversy. It was developed to replace the empirical constants in the standard k-ε model with an analytical relationship developed from Re-normalisation Group theory and has been found to provide better performance than the standard k-ε model in some studies, such as in simulating three swirling flows [7, 8, 9]. However, the development of the RNG k-ε model is still controversial [10, 11, 12]. The SST model combines the strengths of the standard k-ε model and the k-ω model and to offer some advantages over the standard k-ε model in near wall flows [13, 14, 15], such as a rectangular jet in cross flow [16] and a separating flow in a planar asymmetric diffuser [17]. Nevertheless, the limitations of RANS models are also well known, especially in conditions where departures of the instantaneous flow from the mean flow becomes significant [10]. Approaches to address these limitations span URANS through to Large Eddy Simulation (LES) [18], which offer a trade-off between computational expense and accuracy. Before embarking on the more expensive LES approach, it is desirable to assess the strengths and limitations of the two-equation URANS approaches. However, no systematic assessment of this approach is presently available.

Guo et al. [19] used an unsteady formulation of the standard k-ε model, which predicts the ensemble-averaged flow and assumes that the turbulent viscosity is isotropic, to simulate the related flow downstream from a long pipe inlet into a large chamber with a similar expansion ratio to the FPJ nozzle. They predicted flow streamline patterns that yield qualitative agreement with the related FPJ flow including the asymmetric reattachment of the jet, the recirculation zone and the

swirling flow in the most upstream part of the nozzle. The effects of both the Reynolds number and the expansion ratio on the Strouhal number have been compared with experimental results of the FPJ nozzle [19, 20, 6]. However, the length-diameter ratio (*L/D*) of the downstream chamber is about 16, more than five times greater than that of the FPJ nozzle, at which distance the flow approaches being fully developed. This contrasts the exit flow from the FPJ nozzle, which spreads rapidly and generates a complex recirculation of external fluid back into the nozzle chamber.

The structure of the ensemble-averaged FPJ flow was studied by Chen et al. [21] using the unsteady SST model. Six vortex cores were identified and the vortex skeleton of the flow was reported based on both the previous experimental observations [6, 22, 23] and the simulation. Chen et al. [24] investigated the mode switching phenomenon of the FPJ flow using the unsteady SST model. They found that a certain extent of asymmetries, either in the inflow or the initial flow field, were necessary to trigger the flow to switch from the Axial Jet mode to the Precessing Jet mode and the switch time was inversely proportional to the intensity of the asymmetry. Some preliminary validation against previous experimental results were reported [21, 24] The predicted the precession frequency, the axial centreline velocity and the equivalent diameter of the phase-averaged jet were compared against the measured data [21]. Both the rates of spread and centreline velocity decay of the phase-averaged precessing jet were found to be under-predicted with the SST model. However, the validation of the SST approach is not complete and the reliability of other two-equation URANS models in predicting the FPJ flow is still unknown.

According to Wong et al. [25], both the spreading rate and the centreline ve-

locity decay rate of the precessing jet within the nozzle are greater than that of a non-precessing unconfined jet and more closely match that of a jet in a weak counter-flow. However, the extent to which these rates of spread and decay correlate with whether or not a model predicts the occurrence of precession has not been reported previously. Many studies reported that the standard k-ε model over-predicts the spreading rate of an unconfined round jet. According to the studies of Morse [26] and Pope [27], the constant $C_{1\varepsilon}$ in the turbulence dissipation rate (ε) equation of the standard k-ε model can be modified from 1.44 to 1.6 in the current work to overcome this issue in predicting a free jet. This revised model is termed the modified k-ε (1.6) model. To investigate on the effect of internal jet's spreading rate and centreline velocity decay in predicting the FPJ flow, three values of $C_{1\varepsilon}$, i.e. 1.3 (the modified k-ε (1.3) model), 1.44 (the standard k-ε model) and 1.6 (the modified k-ε (1.6) model) were adopted in this study to generate three jets with different spreading rate and centreline decay rate within the chamber.

In light of the above gaps in previous work, the aim of the present study is to assess the extent to which two-equation URANS models of the phase mean flow can reproduce known qualitative features and quantitative data of FPJ flow. In addition, it aims to provide new insight into the nature of this complex flow.

2 Numerical approach

The geometric configuration of the present nozzle was chosen to match exactly the configuration used in previous experiment [28, 25], which report detailed phase-averaged data of the flow-field within the FPJ nozzle and in the near-field of the emerging jet. These measurements were undertaken using both laser Doppler

anemometry (LDA) and particle image velocimetry (PIV) techniques.

2.1 Geometry and simulation conditions

The software CREO 2.0 and ANSYS/Design Modeler 16.5 was used to generate the geometrical configuration of the FPJ nozzle, shown in Figure 2. The profile of the smooth contraction at the inlet to the device is described by a 5th order polynomial, based on Morel's criterion [29], with an area-based contraction ratio of 10.03:1 also following the experimental device [28]. The computational domain outside of the nozzle is an order of magnitude larger than the nozzle itself in both the axial and radial directions, with a diameter of 1032 mm and length of 1000 mm. The distance between the contraction's inlet and the inlet to the chamber is $2.05D$, here D is the diameter of the nozzle chamber, i.e. 80 mm.

The software ANSYS/ICEM CFD 16.5 was employed to generate the mesh. Mesh quality near to the wall of the chamber was ensured by using the "O-girds" method. Figure 3 shows the structured mesh with the 5.5 million nodes employed for all cases reported here, which was developed based on a grid independent test [24].

The bulk mean velocity of the flow at the inlet of the FPJ nozzle (u_i) is 78.7 m/s and the working fluid is air at 25 $^{\circ}C$ and 1 atm. A free-pressure boundary condition was chosen for the other boundaries of the computational domain (shown in red in Figure 3a) with a relative pressure to ambient of 0 Pa, consistent with the experiments being performed in an unconfined environment. The adopted convective scheme is high resolution. A monitor point (MP1), at r=30 mm and x=207.2 mm, was chosen to determine the precession frequency, which was identical to the

measurement [25]. Another monitor point (MP2) located near to the exit of the FPJ nozzle was chosen to identify the start and end time of each precession cycle, which follows the measurement of Wong [25]. The phase of each cycle was then divided into 36 time-intervals, each corresponding to a ten-degree span of phase angles, to total 360° for the whole cycle. Taking the average of the velocity data binned with each ten-degree arc of the precession cycle results in 36 velocity values corresponding to the 36 ten-degree-range, which present the phase-averaged velocity field.

For all cases reported herein, the root mean square (r.m.s) of the residuals was all less than 5×10^{-5}. The time-step in these simulations was taken to be 1/667th of the measured mean period of each precession cycle, i.e. 0.13 seconds, corresponding to 0.0002 seconds. This provides about 18 time-steps in each 10° of precession. The model was allowed to run for some 27 seconds of flow time to converge to a solution that is independent of the initial condition and the data was then recorded from the subsequent 5 precession cycles. All simulations were conducted using a Dell PowerEdge R 815 Rack Mount Server. The wall clock time of a typical simulation is about 7 days using 16 cores.

2.2 URANS Turbulence Models

Three types of two-equation URANS turbulence models were compared in their capacity to predict the unsteady FPJ flow.

2.2.1 The standard k-ε and modified k-ε models

For the standard k-ε model, the transport equations for the turbulent kinetic energy k and the rate of turbulence dissipation ε are:

$$\frac{\partial(\rho k)}{\partial t}+\frac{\partial}{\partial x_j}(\rho U_j k)=\frac{\partial}{\partial x_j}\left[\left(\mu+\frac{\mu_t}{\sigma_k}\right)\frac{\partial k}{\partial x_j}\right]+P_k-\rho\varepsilon \tag{1}$$

and

$$\frac{\partial(\rho \varepsilon)}{\partial t}+\frac{\partial}{\partial x_j}(\rho U_j \varepsilon)=\frac{\partial}{\partial x_j}\left[\left(\mu+\frac{\mu_t}{\sigma_\varepsilon}\right)\frac{\partial \varepsilon}{\partial x_j}\right]+C_{1\varepsilon}\frac{\varepsilon}{k}P_k-C_{2\varepsilon}\rho\frac{\varepsilon^2}{k} \quad , \tag{2}$$

where ρ is the density of the fluid, μ is the air dynamic viscosity and μ_t is the turbulence viscosity, defined as:

$$\mu_t=\rho C_\mu \frac{k^2}{\varepsilon} \quad . \tag{3}$$

The turbulence production due to viscous forces P_k was modelled using:

$$P_k=\mu_t\left(\frac{\partial U_i}{\partial x_j}+\frac{\partial U_j}{\partial x_i}\right)\frac{\partial U_i}{\partial x_j}-\frac{2}{3}\frac{\partial U_k}{\partial x_k}\left(3\mu_t\frac{\partial U_k}{\partial x_k}+\rho k\right) \quad . \tag{4}$$

The value of the five empirical constants: $C_\mu, \sigma_k, \sigma_\varepsilon, C_{1\varepsilon}$ and $C_{2\varepsilon}$ in the standard k-ε model are listed in Table 1.

2.2.2 The RNG k-ε model

The transport equations for k and ε in the RNG k-ε model are given as follows:

$$\frac{\partial(\rho k)}{\partial t}+\frac{\partial}{\partial x_j}(\rho U_j k)=\frac{\partial}{\partial x_j}\left[\left(\mu+\frac{\mu_t}{\sigma_{kRNG}}\right)\frac{\partial k}{\partial x_j}\right]+P_k-\rho\varepsilon \tag{5}$$

and

$$\begin{aligned}\frac{\partial(\rho\varepsilon)}{\partial t}+\frac{\partial}{\partial x_j}(\rho U_j\varepsilon)=&\frac{\partial}{\partial x_j}\left[\left(\mu+\frac{\mu_t}{\sigma_{\varepsilon RNG}}\right)\frac{\partial\varepsilon}{\partial x_j}\right]\\&+C_{1\varepsilon RNG}\frac{\varepsilon}{k}P_k-C_{2\varepsilon RNG}\rho\frac{\varepsilon^2}{k}\quad .\end{aligned} \tag{6}$$

Different from the standard k-ε model, the constant $C_{1\varepsilon}$ is replaced by $C_{1\varepsilon RNG}$:

$$C_{1\varepsilon RNG}=1.42-f_\eta\quad , \tag{7}$$

where

$$f_\eta=\frac{\eta\left(1-\frac{\eta}{4.38}\right)}{1+\beta_{RNG}\eta^3}\quad , \tag{8}$$

$$\eta=\sqrt{\frac{P_k}{\rho C_{\mu RNG}\varepsilon}} \tag{9}$$

and where β_{RNG} is 0.012. The values of the other constants are listed in Table 2 [30].

2.2.3 The SST model

The SST model, developed by Menter [31], is a hybrid between the standard k-ε model, which it employs in the flow region faraway from wall, and the k-ω model, which is employed in the near-wall region. This is because the standard k-ε model is more robust in the regions away from the near wall, although its performance in the near-wall region is not satisfactory, while the k-ω model, performs well in the near-wall region, but requires an assumed free stream value of turbulent frequency, ω, that influences the simulation result [30, 31]. The transport equations of k and ω in the k-ω model are shown in Equation 10 and 11, while $\omega = \varepsilon/k$. The values of the empirical constants in the k-ω model are listed in Table 3.

$$\frac{\partial(\rho k)}{\partial t} + \frac{\partial}{\partial x_j}(\rho U_j k) = \frac{\partial}{\partial x_j}\left[\left(\mu + \frac{\mu_t}{\sigma_{k1}}\right)\frac{\partial k}{\partial x_j}\right] + P_k - \beta'\rho k\omega \qquad (10)$$

and

$$\frac{\partial(\rho \omega)}{\partial t} + \frac{\partial}{\partial x_j}(\rho U_j \omega) = \frac{\partial}{\partial x_j}\left[\left(\mu + \frac{\mu_t}{\sigma_{\omega}}\right)\frac{\partial \omega}{\partial x_j}\right] + \alpha\frac{\omega}{k}P_k - \beta\rho\omega^2 \quad . \qquad (11)$$

In the SST model, the k-equation (Equation 12) is the same as in k-ω model, while the ε-equation is similar to the ω-equation in the k-ω model, with the substitution $\varepsilon = k\omega$. The transformed equations of k and ω are shown below:

$$\frac{\partial(\rho k)}{\partial t} + \frac{\partial}{\partial x_j}(\rho U_j k) = \frac{\partial}{\partial x_j}\left[\left(\mu + \frac{\mu_t}{\sigma_{k2}}\right)\frac{\partial k}{\partial x_j}\right] + P_k - \beta'\rho k\omega \qquad (12)$$

and

$$\frac{\partial(\rho\omega)}{\partial t}+\frac{\partial}{\partial x_j}(\rho U_j\omega)=\frac{\partial}{\partial x_j}\left[\left(\mu+\frac{\mu_t}{\sigma_{\omega1}}\right)\frac{\partial\omega}{\partial x_j}\right]+2\rho\frac{1}{\sigma_{\omega1}\omega}\frac{\partial k}{\partial x_j}\frac{\partial\omega}{\partial x_j} + \alpha_1\frac{\omega}{k}P_k-\beta_1\rho\omega^2 \quad . \tag{13}$$

The k and ω equations in the SST model are obtained by adding the transformed k-ε equations (Equation 12 and 13) multiplied by a function 1-F_1 to the k-ω model equations (Equation 10 and 11) multiplied by a function F_1:

$$\frac{\partial(\rho k)}{\partial t}+\frac{\partial}{\partial x_j}(\rho U_j k)=\frac{\partial}{\partial x_j}\left[\left(\mu+\frac{\mu_t}{\sigma_{k2}}\right)\frac{\partial k}{\partial x_j}\right]+P_k-\beta'\rho k\omega \tag{14}$$

and

$$\frac{\partial(\rho\omega)}{\partial t}+\frac{\partial}{\partial x_j}(\rho U_j\omega)=\frac{\partial}{\partial x_j}\left[\left(\mu+\frac{\mu_t}{\sigma_{\omega1}}\right)\frac{\partial\omega}{\partial x_j}\right] + (1-F_1)2\rho\frac{1}{\sigma_{\omega1}\omega}\frac{\partial k}{\partial x_j}\frac{\partial\omega}{\partial x_j} + \alpha_1\frac{\omega}{k}P_k-\beta_1\rho\omega^2 \quad , \tag{15}$$

where

$$F_1=tanh\left(arg_1^4\right) \tag{16}$$

and where

$$arg_1=min\left(max\left(\frac{\sqrt{k}}{\beta'\omega y},\frac{500\nu}{y^2\omega}\right),\frac{4\rho k}{CD_{k\omega}\sigma_{\omega1}y^2}\right) \tag{17}$$

and

$$CD_{k\omega} = max\left(2\rho\frac{1}{\sigma_{\omega 1}\omega}\frac{\partial k}{\partial x_j}\frac{\partial \omega}{\partial x_j}, 1.0\times 10^{-10}\right) \quad . \tag{18}$$

Different from the standard k-ε and k-ω model, the turbulent viscosity is given as:

$$\mu_t = \frac{\alpha\rho k}{max(\alpha\omega, SF_2)} \quad , \tag{19}$$

where S=$\sqrt{2S_{ij}S_{ij}}$ and

$$F_2 = tanh(arg_2^3) \tag{20}$$

with

$$arg_2 = max\left(\frac{2\sqrt{k}}{\beta'\omega y}, \frac{500\nu}{y^2\omega}\right) \quad . \tag{21}$$

The value of the constants employed in the SST model are listed in Table 4 [30].

To address address the limitation of the eddy-viscosity models in poor prediction of the influence of streamline curvature and system rotation [32], the correction to on the production term P_k of Shur et al. [33] was adopted. The new $P_{k\text{-}c}$ is defined as:

$$P_{k\text{-}c} = P_k \cdot f_r \quad , \tag{22}$$

where

$$f_r = max(0, 1 + C_{scale}(\tilde{f}_r - 1)) \tag{23}$$

and

$$\tilde{f}_r = max(min(f_{rotation}, 1.25), 0) \tag{24}$$

The function $f_{rotation}$ is given as:

$$f_{rotation} = (1 + c_{r1}) \frac{2r^*}{1 + r^*} \left[1 - c_{r3} tan^{-1}(c_{r2}\tilde{r})\right] - c_{r1} \quad , \tag{25}$$

where

$$r^* = \frac{s}{\Omega} \tag{26}$$

and

$$\tilde{r} = 2\Omega_{jk} S_{jk} \left[\frac{DS_{ij}}{Dt} + (\varepsilon_{imn} S_{jn} + \varepsilon_{jmn} S_{in})\Omega_m^{rot}\right] \frac{1}{\Omega D^3} \quad . \tag{27}$$

Here

$$S_{ij} = \frac{1}{2}\left(\frac{\partial u_i}{\partial x_j} + \frac{\partial u_j}{\partial x_i}\right) \quad , \tag{28}$$

$$\Omega_{ij} = \frac{1}{2}\left[\left(\frac{\partial u_i}{\partial x_j} - \frac{\partial u_j}{\partial x_i}\right) + 2\varepsilon_{mji}\Omega_m^{rot}\right] \quad , \tag{29}$$

$$S^2 = 2S_{ij}S_{ij} \quad , \tag{30}$$

$$\Omega^2 = 2\Omega_{ij}\Omega_{ij} \quad , \tag{31}$$

and

$$D^2 = max\left(S^2, 0.09\omega^2\right) \quad . \tag{32}$$

Here DS_{ij}/Dt are the components of the Lagrangian derivative of the strain rate tensor, while the constant C_{r1}, C_{r2}, C_{r3} are equal to 1, 2 and 1, respectively. The scale coefficient C_{scale} is set to 1 in this study.

2.3 Triple decomposition

For this FPJ flow, the instantaneous value of a given parameter can be decomposed following Hussain and Reynolds [34], as follows:

$$\Phi(t) = \bar{\Phi} + \tilde{\Phi}(t) + \Phi' \quad . \tag{33}$$

Here $\bar{\Phi}$ is the mean value, $\tilde{\Phi}(t)$ is the periodic component and Φ' is the stochastic turbulent fluctuation relative to the periodic flow. The sum of the mean value and periodic part, i.e. $\langle\Phi\rangle(t) = \bar{\Phi} + \tilde{\Phi}(t)$, is defined as the ensemble-averaged component [35]. In the simulation, the ensemble-averaged component, which is related to the precession motion, is resolved while the turbulence component, which is superimposed on this periodic motion, is modelled using two-equation URANS models. Here, the phase-averaged flow-field was obtained by taking the average of the converged flow-fields at the same phase of the cycle.

3 Results and discussion

3.1 Cycle-independence study

Figure 4 shows how changes to the number of cycles of precession over which the data are calculated influences the axial evolution of the calculated normalized phase-averaged equivalent diameter (d_{eq}) of the precessing for 5, 10 and 15 precession cycles. Following the work of Wong [25], the cross-sectional area of the jet is defined by enclosed area of the half-maximum velocity contour. The data were calculated using the standard k-ε model and 5.5 million grids. It can be seen that the results have converged after 5 cycles of precession. This is consistent with the previous observation that the cycle-to-cycle variations tend to become vanishingly small in the simulation using two-equation URANS model [36]. Further evidence for this can be found in the observation that the direction of precession was never observed to change during a simulation, which differs from experimental result [6]. This result in Figure 4 justifies the choice adopted for all subsequent two-equation URANS calculations to limit the analysis to averaging over just 5 precession cycles, which moderates the computing load.

3.2 Simulation of the FPJ flow using two-equation URANS models

Figure 5 (a-c) presents volumetric visualisations of the streamlines of the FPJ flow within the chamber, as calculated with the three types of two-equation URANS models, i.e. the standard k-ε model, the RNG k-ε model and the SST model. It can be seen that all four key qualitative features of the FPJ flow have been

successfully predicted with both the standard k-ε model (Figure 5a) and the SST model (Figure 5b). However, as shown in Figure 5c, the RNG k-ε model does not reproduce either the asymmetric reattachment (Feature 1), or the deflected emerging jet flow (Feature 4). In contrast to the experimental measurements, the jet within the chamber is predicted with RNG k-ε model to impinge onto the centre body, rather than to reattach to the internal wall of the chamber. In addition, the flow emerging from the exit from the nozzle chamber is predicted to leave at a much shallower angle than measured experimentally. This relatively poor performance of the RNG k-ε model for the FPJ flow contrasts its relatively good performance in simulating some swirling flows [37].

An explanation for the relative success and failure of the above models in predicting the qualitative features of the flow identified in Figure 5 can be found in Figure 6, which presents the corresponding axial evolutions of the d_{eq} of the phase-averaged jet with axial distance. It can be seen that the RNG k-ε model under-predicts the rate at which the diameter of the jet within the chamber grows in the region upstream from the centre body, i.e. in the region $x/d<11.5$. However, for the case in which the modelled length of the nozzle chamber is extended to the non-physical value L_c=240 mm, shown in Figure 5d, the increased length allows the jet to spread to a sufficient width within the chamber for precession to be calculated to occur. For this case, the jet is also calculated to precess. Taken together, these results show that the success or failure of the adopted two-equation URANS models to reproduce the key qualitative features of the flow-field is dependent primarily on the accuracy with which they reproduce the spreading rate of the jet within the chamber. We also note that, because of the failure of the RNG k-ε model to reproduce the precession motion reliably, the results from it have

also been excluded from the subsequent figures and discussions.

Figure 6 also reveals a complex trend in the relative accuracies predicted for the axial evolution of normalized d_{eq} of the phase-averaged jet through the chamber. The standard k-ε under-predicts d_{eq} in the region upstream from the centre body, $5<x/d<11.5$, which is consistent with the simulation with the SST model [21]. The under-prediction of the standard k-ε model here is in contrast to its over-prediction of spreading rate in an unconfined, round jet [27, 38]. The standard k-ε model also stands out from the two models in greatly over-predicting the spreading rate of the phase-averaged jet between the centre body and the nozzle exit plane, $11.5<x/d<13.8$, while the SST model showed a greatly reduced spreading rate in these locations, like the experiments [21, 25]. For both of the two turbulence models, the largest difference between the measured and calculated values of the normalized d_{eq} within the nozzle chamber occurs at x/d=7.03, where the difference is 16.7% and 24.3% for the SST [21] and the standard k-ε models, respectively. In the internal field, the average difference between the normalized measured and predicted value of d_{eq} for the SST [21] and standard k-ε models are 12.4% and 14.6%, while they are 16.0% and 38.7% in the emerging field, i.e. $x/d>13.8$.

Figure 7 presents the phase-averaged axial velocity contours of the cross-sectional plane at x/d=8.93 obtained both experimentally [28] and numerically using the SST model and the standard k-ε model. It can be seen that the cross-sectional area of the jet as predicted with both the SST model and the standard k-ε model, shown in red, is less than the experimental results. The experimental results reveal that the jet fully attaches to the chamber wall, while the simulations of both the SST model and standard k-ε model predict the jet to be only interact-

ing weakly with the wall. Compared with the flow predicted with the standard k-ε model, the jet calculated with the SST model is slightly closer to the chamber wall. This is consistent with the trend that the spreading rate calculated with the SST model is greater than that calculated with the standard k-ε model (Figure 6).

Figure 8 presents the measured and calculated phase-averaged axial velocity contours of the transverse plane at x'/D_e=16. The jet's half-width contour is depicted by the red line in these figures. The contours predicted with the standard k-ε and SST models have a similar shape and size to the measured values.

Figure 9 presents the measured [25] and predicted inverse velocity decay along the centreline of the local, phase-averaged jet on its trajectory through the nozzle chamber for the standard k-ε model and the SST model [21]. It can be seen that both the SST and the standard k-ε models predict a longer potential core than the measured value. More specifically, the length of the potential core predicted with these two turbulence models is about $x/d \approx 5$, which is the same as that of a steady jet, while the measured jet velocity begins to decay at approximately $x/d \approx 3$. These trends are consistent with those of the predicted spreading rates, described above. However, these trends contrast those for a round free jet, where the standard k-ε model is reported to over-predict the velocity decay rate. In contrast, the decay rate has been under-predicted with the standard k-ε model for the precessing jet flow within the nozzle chamber. That is, as discussed above, the constants of the standard k-ε model do not adequately account for the influence of either the chamber or the surrounding swirling flow in the upstream region of the chamber.

Figure 9 also shows that, in the external field, the centreline velocity of the jet is perhaps predicted better with the standard k-ε model than the SST model [21],

although a definitive comparison is difficult owing to the scatter in the measured data. The calculated trends are consistent with those of the spreading rate (Figure 6) although the agreement with the measured data differs somewhat. This can be explained by the shape of the cross section of the jet being far from round, which makes it difficult to characterise with these two simplified measures.

Figure 10a presents the normalized time mean axial velocity profile at x'/D_e=0.16 that measured [28] and predicted with the standard k-ε model and the SST model [24]. Similar to the SST model, correct trend of the mean axial velocity was predicted with the standard k-ε model. It can be seen that the calculated average deflected angle of the exit jet to the axis of the chamber is close to the experimental result according to the Figure 10a.

Figure 10b presents a comparison between the calculated and measured total fluctuation energy (E_f) at x'/D_e=0.16, which is the sum of the periodic ($\tilde{E}$) and the turbulent fluctuation (E') [25, 21]. The periodic fluctuation, which was calculated based on the predicted root mean square (RMS) velocities in each direction, represents the effect of the precession motion. Similar to the SST model, the total fluctuation energy was over-predicted with the standard k-ε model.

Figure 11 presents the distribution of F_1 (in Equation 16), which determines whether the k-ε or k-ω model dominates in the results of the SST model at a particular location, in five cross-sectional planes within the nozzle. The function F_1 yields low values in the central region of the chamber and values close to unity near to the wall. This implies that the k-ε model dominates in the central region. Hence, similar to the standard k-ε model, the under-prediction of the spreading rate in the FPJ model can be attributed to the non-universal nature of the constants in the SST model.

Figure 12 presents the energy spectrum at monitor point MP_2, which is obtained by fast Fourier transform (FFT). The precession frequency (f_p) is then calculated from the peak frequency of this spectrum. The calculated value of f_p, shown in Table 5, as predicted with the standard k-ε is 8.5 Hz, which is higher than both the measured value and that predicted with the SST model [21]. Table 5 also presents the diameter of the phase-averaged jet at x/d=8.93. It can be seen that there is no correlation between the predicted diameter of the jet within the chamber and the frequency. This is unlike the case found in experiments by [39], in which the pipe jet inlet, which also has the lowest initial spreading rate within the chamber, has the lowest Strouhal number, while the orifice jet, which has the largest internal spreading rate, also has the highest Strouhal number. This is due to other differences between the two modelling approaches.

3.3 Further investigation on the effect of the spreading and centreline decay rate of the predicted jet on calculated FPJ flow

Figure 13 presents the iso-surface of the predicted instantaneous turbulence kinetic energy, k, at 200 m^2/s^2 within the nozzle chamber as predicted with three different values of the constant $C_{1\varepsilon}$, i.e. $C_{1\varepsilon}$=1.3, $C_{1\varepsilon}$=1.44 and $C_{1\varepsilon}$=1.6, corresponding to the modified k-ε (1.3), the standard k-ε and the modified k-ε (1.6) models, respectively. Since $C_{1\varepsilon}$ is in the production term in ε equation (Equation 2), the magnitude of ε is expected to increase with an increase in $C_{1\varepsilon}$. Similarly, an increase in ε is expected to decrease the magnitude of k because the '$-\rho\varepsilon$' term in Equation 1 reduces k. This trend is confirmed in Figure 13, which shows

that the largest areas of the iso-surface of k is predicted to occur with the modified k-ε (1.3) model, while the smallest is predicted to occur with the modified k-ε (1.6) model. This shows that the calculated spreading rate of the jet within the chamber is influenced by the constant $C_{1\varepsilon}$.

Figure 14 compares the axial evolution of the normalized value of d_{eq} of the phase-averaged jet as predicted with the three k-ε models. As expected, the modified k-ε (1.3) model generates the greatest spreading rate, while the modified k-ε (1.6) generates the lowest. The average differences between the measured and predicted values of the normalized value of d_{eq} within the nozzle chamber are 10.6%, 14.6% and 22.8% for the modified k-ε (1.3), the standard k-ε and the modified k-ε (1.6) models, respectively. The greatest difference between the measurements and predictions for both the modified k-ε (1.3) and the standard k-ε models occur at x/d=7.03, which are 24.3% and 20.4%, while it occurs at x/d=8.93 for the modified k-ε (1.6) model, which is 51.0%. In the emerging field, all three models over-predict d_{eq} by a factor that is greatest for the modified k-ε (1.3) model, where the average difference from the measured value of 46.9%.

Figure 15 presents the inverse centreline velocity decay of the phase-averaged jet predicted with the modified k-ε (1.3), the standard k-ε and the modified k-ε (1.6) models, respectively. This shows that the modified k-ε (1.3) model gives the best prediction of the initial decay of the centreline velocity of the local jet within the chamber, but then over-predicts the decay rate in the region $8.93<x/d<17$. Because of the decrease in the predicted turbulent kinetic energy, the modified k-ε (1.6) model under-predicts the centreline velocity decay of the phase averaged jet within the nozzle chamber. The constants shown in Table 1 were derived for canonical flows in a uniform pressure field and cease to be constant in regions

where the pressure gradient varies through the flow field. The complex geometry of the chamber generates an adverse pressure gradient around the entering jet to increase its initial spreading rate, while the presence of centre body introduces a radial contraction and a circumferential spreading as the jet passes around it, together with strong pressure gradients downstream from it. No single set of constants for any of the URANS models is applicable in the presence of such strong and complex pressure gradients.

Figure 16 shows the instantaneous streamlines predicted with the three k-ε models. The four key flow features of the precession motion have been reproduced with both the standard k-ε model and the modified k-ε (1.3) model. However, with the modified k-ε (1.6) model, as with the RNG k-ε model, the jet is calculated to impinge directly onto the centre body instead of reattaching to the internal wall of the nozzle chamber. Hence, the key qualitative features of the precession motion are reproduced with the two-equation URANS models where the constants in the model are chosen to yield sufficiently good agreement with the measured values of the mean rates of spread and decay of the phase-averaged jet within the chamber.

4 Conclusion

The key findings of the paper are as follows:

The four key qualitative features of the FPJ flow can be reproduced with the adopted two-equation URANS models, provided that the constants are chosen so that the typical rates of spread and decay of the phase-averaged jet within the chamber match the actual values sufficiently closely. This shows that the two-equation URANS models yield good qualitative agreement with both the phase-

averaged flows measured experimentally and the key instantaneous features observed from flow visualisation.

The rates of spread and decay of the phase-averaged jet within the upstream part of the chamber are predicted most accurately with the modified k-ε (1.3) model, while the rates of spread and decay of the emerging jet are better predicted with the standard k-ε model. Both the standard k-ε model and the SST model also have the best overall performance in predicting the FPJ flow among the five two-equation URANS models assessed in the current work. This implies that the pressure gradients within the chamber are too strong and complex for a single set of constants to reliably reproduce all regions of the flow through it.

There is a strong correlation between the extent to which any of the adopted two-equation URANS models reproduce the four qualitative features associated with the FPJ flow and the extent to which they reproduce the phase-averaged rate of spread and decay of the local jet within the chamber. This highlights the importance of reproducing these features as a requisite to reasonable modelling of the FPJ flow.

No obvious advantage is found in the use of the SST model over the k-ε type models. This implies that the flow-field within the FPJ chamber is dominated by the effects of confinement and inertia, while the role of the boundary-layer is less significant.

Similar to the SST model, the standard k-ε model demonstrates the capability to reproduce the mean value and periodic components of the FPJ flow, which is important to both the industrial design of kiln burners and the investigation of the external scalar field of the FPJ flow.

5 Acknowledgment

The first author acknowledges the support of the Divisional Scholarship of the faculty of ECMS, the University of Adelaide. The authors were supported by the Australian Research Council through Grant DP150102230.

References

[1] Nathan, G. J., and Luxton, R. E., 1988. Controlling the motion of a fluid jet.

[2] Nathan, G. J., Mi, J., Alwahabi, Z. T., Newbold, G. J. R., and Nobes, D. S., 2006. "Impacts of a jet's exit flow pattern on mixing and combustion performance". *Progress in Energy and Combustion Science,* **32**(5-6), pp. 496–538.

[3] Manias, C. G., and Nathan, G. J., 1993. "The precessing jet gas burner: a low nox burner providing process efficiency and product quality improvements". *World Cement,* **24**(3), pp. 4–11.

[4] Manias, C. G., and Nathan, G. J., 1994. "Low nox clinker production". *World Cement,* **25**(5), pp. 54–56.

[5] Videgar, R., 1997. "Gyro-therm technology solves burner problems: The application of new gyro-therm burner technology in the durkee plant". *World Cement,* **28**, pp. 39–45.

[6] Nathan, G. J., Hill, S. J., and Luxton, R. E., 1998. "An axisymmetric 'fluidic'nozzle to generate jet precession". *Journal of Fluid Mechanics,* **370**(1), pp. 347–380.

[7] Escue, A., and Cui, J., 2010. "Comparison of turbulence models in simulating swirling pipe flows". *Applied Mathematical Modelling,* **34**(10), pp. 2840–2849.

[8] Gupta, A., and Kumar, R., 2007. "Three-dimensional turbulent swirling flow in a cylinder: Experiments and computations". *International Journal of Heat and Fluid Flow,* **28**(2), pp. 249–261.

[9] Orfanoudakis, N., Hatziapostolou, A., Krallis, K., Mastorakos, E., Sardi, K., Pavlou, D., and Vlachakis, N., 2005. "Design, evaluation measurements and modelling of a small swirl stabilised laboratory burner". *IFRF Web Journal*(200510).

[10] Teodorovich, E., 1994. "On the yakhot—orszag theory of turbulence". *Fluid dynamics,* **29**(6), pp. 770–779.

[11] Wang, X. H., and Wu, F., 1993. "One modification to the yakhot-orszag calculation in the renormalization-group theory of turbulence". *Physical Review E,* **48**(1), p. R37.

[12] Nagano, Y., and Itazu, Y., 1997. "Renormalization group theory for turbulence: Assessment of the yakhot-orszag-smith theory". *Fluid Dynamics Research,* **20**(1), pp. 157–172.

[13] Menter, F., 1996. "A comparison of some recent eddy-viscosity turbulence models". *Journal of Fluids Engineering,* **118**(3), pp. 514–519.

[14] Menter, F., Kuntz, M., and Langtry, R., 2003. "Ten years of industrial experience with the sst turbulence model". *Turbulence, Heat and Mass Transfer,* **4**, pp. 625–632.

[15] Tkatchenko, I., Kornev, N., Jahnke, S., Steffen, G., and Hassel, E., 2007. "Performances of les and rans models for simulation of complex flows in a coaxial jet mixer". *Flow, Turbulence and Combustion,* **78**(2), pp. 111–127.

[16] Tian, Z. F., Witt, P. J., Yang, W., and Schwarz, M. P., 2011. "Numerical simulation and validation of gas-particle rectangular jets in crossflow". *Computers & Chemical Engineering,* **35**(4), pp. 595–605.

[17] El-Behery, S. M., and Hamed, M. H., 2011. "A comparative study of turbulence models performance for separating flow in a planar asymmetric diffuser". *Computers & Fluids,* **44**(1), pp. 248–257.

[18] Tian, Z. F., Tu, J. Y., Yeoh, G. H., and Yuen, R. K. K., 2007. "Numerical studies of indoor airflow and particle dispersion by large eddy simulation". *Building and Environment,* **42**(10), pp. 3483–3492.

[19] Guo, B., Langrish, T., and Fletcher, D., 2001. "Numerical simulation of unsteady turbulent flow in axisymmetric sudden expansions". *ASME J. Fluids Eng.,* **123**, p. 574.

[20] Hill, S., Nathan, G., and Luxton, R., 1995. "Precession in axisymmetric confined jets". In 12th Australiasian Fluid Mechanics Conference, p. 135–138.

[21] Chen, X., Tian, Z. F., Kelso, R. M., and Nathan, G. J., 2017. "The topology of a precessing flow within a suddenly expanding axisymmetric

chamber". *Journal of Fluids Engineering,* **139**(7), pp. 071201–071201–10. 10.1115/1.4035950.

[22] Wong, C., Nathan, G., and Kelso, R., 2008. "The naturally oscillating flow emerging from a fluidic precessing jet nozzle". *Journal of Fluid Mechanics,* **606**(1), pp. 153–188.

[23] Lee, S., 2009. "Study of a naturally oscillating triangular-jet flow". Thesis.

[24] Chen, X., Tian, Z. F., Kelso, R. M., and Nathan, G. J., 2017. "New understanding of mode switching in the fluidic precessing jet flow". *Journal of Fluids Engineering,* **139**(7), pp. 071102–071102–10. 10.1115/1.4036151.

[25] Wong, C. Y., Lanspeary, P. V., Nathan, G. J., Kelso, R. M., and O'Doherty, T., 2003. "Phase-averaged velocity in a fluidic precessing jet nozzle and in its near external field". *Experimental Thermal and Fluid Science,* **27**(5), pp. 515–524.

[26] Morse, A., 1977. "Axisymmetric turbulent shear flows with and without swirl". Thesis.

[27] Pope, S., 1978. "An explanation of the turbulent round-jet/plane-jet anomaly". *AIAA Journal,* **16**(3), pp. 279–281.

[28] Wong, C. Y., 2004. "The flow within and in the near external field of a fluidic precessing jet nozzle". Thesis.

[29] Morel, T., 1975. "Comprehensive design of axisymmetric wind tunnel contractions". *Journal of Fluids Engineering,* **97**(2), pp. 225–233.

[30] Versteeg, H., and Malalasekera, W., 2007. *An introduction to computational fluid dynamics: the finite volume method*. Prentice Hall.

[31] Menter, F. R., 1992. "Performance of popular turbulence model for attached and separated adverse pressure gradient flows". *AIAA Journal,* **30**(8), pp. 2066–2072.

[32] Smirnov, P. E., and Menter, F. R., 2009. "Sensitization of the sst turbulence model to rotation and curvature by applying the spalart–shur correction term". *Journal of Turbomachinery,* **131**(4), pp. 041010–041010. 10.1115/1.3070573.

[33] Shur, M. L., Strelets, M. K., Travin, A. K., and Spalart, P. R., 2000. "Turbulence modeling in rotating and curved channels: Assessing the spalart-shur correction". *AIAA Journal,* **38**(5), pp. 784–792.

[34] Hussain, A. K. M. F., and Reynolds, W. C., 1970. "The mechanics of an organized wave in turbulent shear flow". *Journal of Fluid Mechanics,* **41**(02), pp. 241–258.

[35] Bosch, G., and Rodi, W., 1998. "Simulation of vortex shedding past a square cylinder with different turbulence models". *International journal for numerical methods in fluids,* **28**(4), pp. 601–616.

[36] Chen, X., Tian, Z., and Nathan, G., 2012. "Numerical simulation of the flow within a fluidic precessing jet nozzle". In Australasian Fluid Mechanics Conference (18th: 2012: Launceston, Tasmania).

[37] Fan, J., Qian, L., Ma, Y., Sun, P., and Cen, K., 2001. "Computational modeling of pulverized coal combustion processes in tangentially fired furnaces". *Chemical Engineering Journal,* **81**(1–3), pp. 261–269.

[38] Rodi, W., 1980. "Turbulent models and their application in hydraulics—a state of the art review". *International Association for Hydraulics Research, Delft*.

[39] Wong, C. Y., Nathan, G. J., and O'Doherty, T., 2004. "The effect of initial conditions on the exit flow from a fluidic precessing jet nozzle". *Experiments in Fluids,* **36**(1), pp. 70–81.

Tables and figures

Table 1: Values of empirical constants in the standard k-ε model [30].

Constants	C_μ	σ_k	σ_ε	$C_{1\varepsilon}$	$C_{2\varepsilon}$
Standard k-ε model	0.09	1.00	1.30	1.44	1.92
Modified k-ε model (1.3)	0.09	1.00	1.30	1.30	1.92
Modified k-ε model (1.6)	0.09	1.00	1.30	1.60	1.92

Table 2: Values of empirical constants in the RNG k-ε model [30].

Constants	$C_{\mu RNG}$	σ_{kRNG}	$\sigma_{\varepsilon RNG}$	$C_{2\varepsilon RNG}$
RNG k-ε model	0.0845	0.7179	0.7179	1.68

Table 3: Values of empirical constants in the present k-ω model [30].

Constants	β'	α	β	σ_{k1}	σ_ω
k-ω model	0.09	5/9	0.075	2	2

Table 4: Values of empirical constants in the SST model [30].

Constants	β'	α	α_1	β_1	σ_{k2}	$\sigma_{\omega 1}$
SST model	0.09	5/9	0.44	0.0828	1	1/0.856

Table 5: The measured [28] and predicted values of the precession frequency and equivalent diameter of the phase-averaged jet at x/d=8.93.

	f_p (Hz)	d_{eq} at x/d=8.93
Measured	7.5	0.044
k-ε model	8.5	0.036
SST model	6.3 [21]	0.038

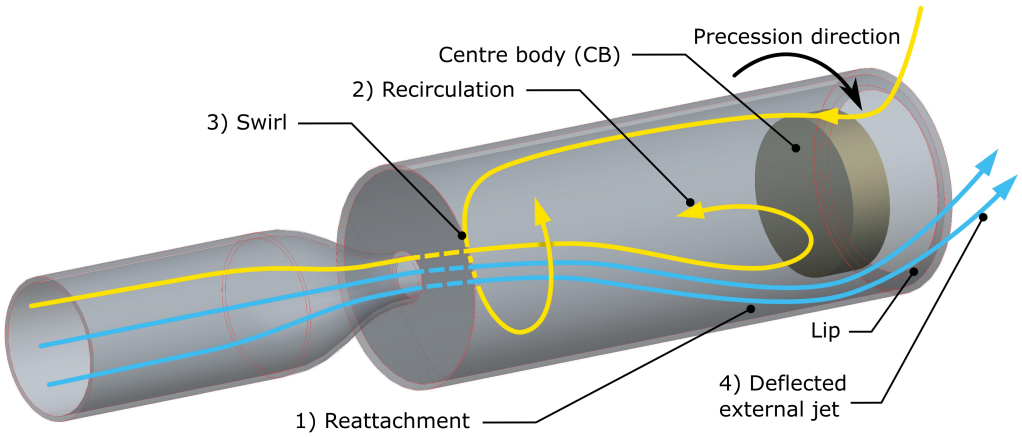

Figure 1: A schematic diagram of the fluidic precessing jet nozzle and flow.

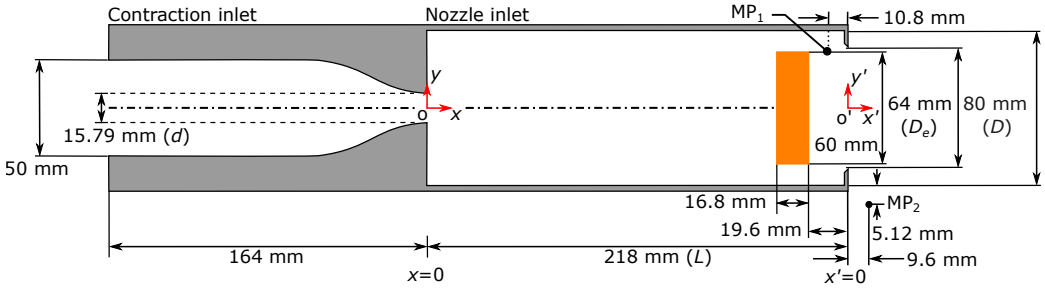

Figure 2: The dimensions of the fluidic precessing jet nozzle modelled here, based on the configuration investigated experimentally by [25], where d, D and D_e are the diameters of the nozzle's inlet, nozzle chamber and nozzle's exit, respectively, L is the length of the FPJ nozzle.

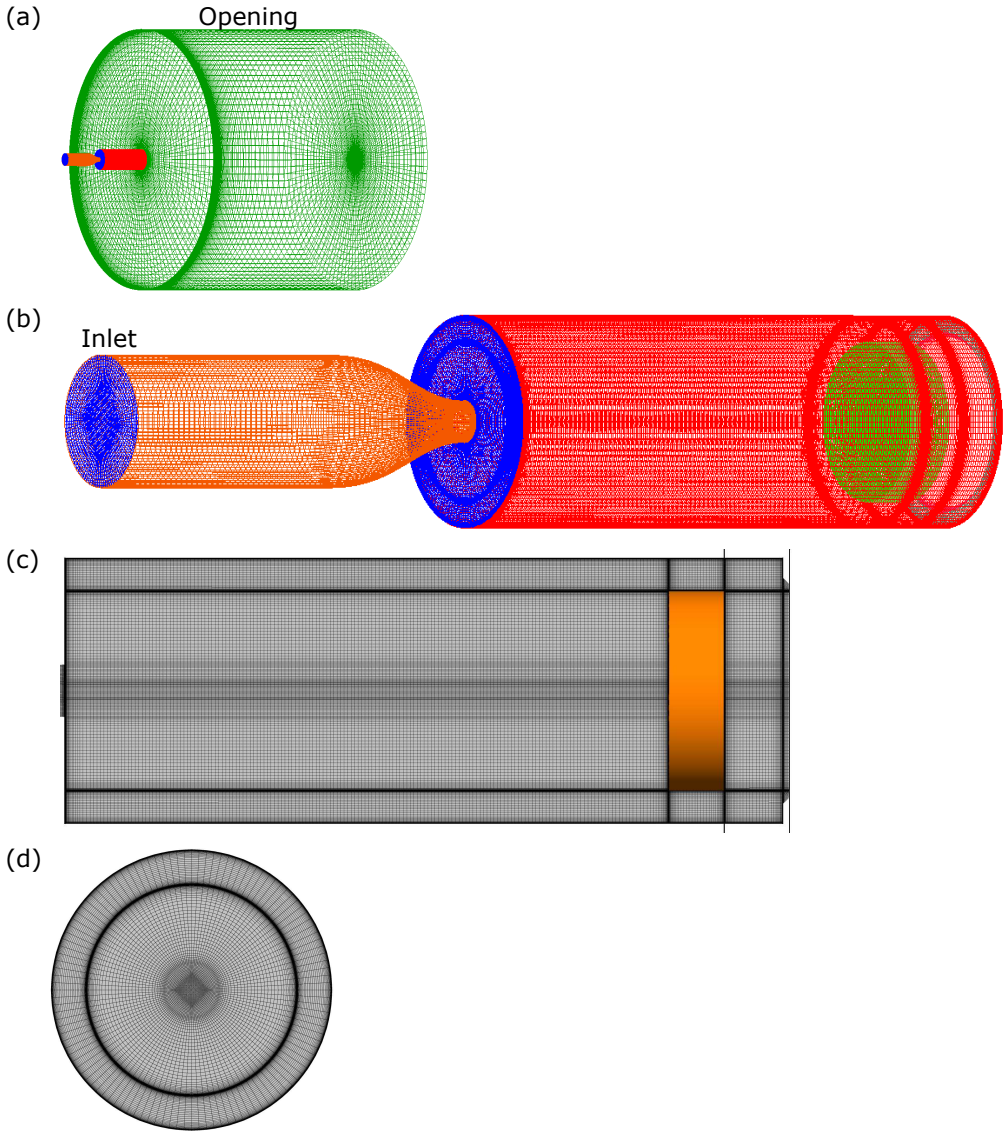

Figure 3: Mesh of the current model. (a) the whole domain, (b) detailed view of the FPJ nozzle, (c) the longitudinal plane through the nozzle and (d) the cross-sectional plane through the nozzle.

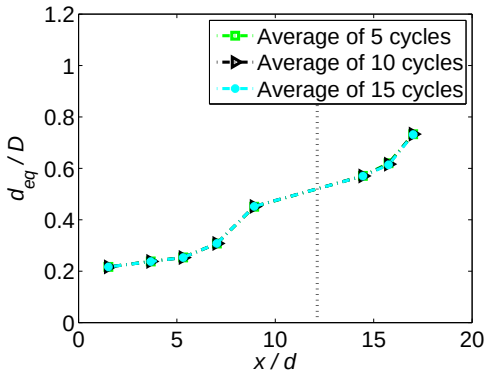

Figure 4: Axial evolution of the normalized predicted equivalent diameters of the precessing jetthrough the domain, as calculated from the average of 5, 10 and 15 cycles of precession. Refer to Figure 2 for symbols and coordinates. The vertical dashed line indicates the location of the upstream surface of the centre body.

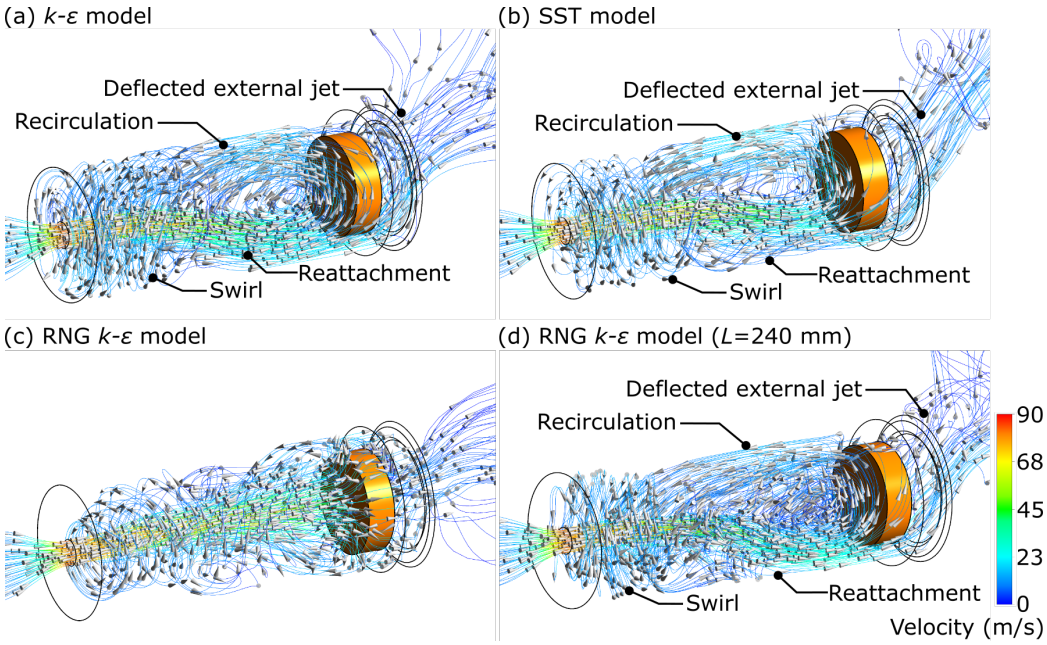

Figure 5: Three-dimensional visualisations of the predicted streamline through the FPJ nozzle with the (a) k-ε model, (b) SST model, (c) RNG k-ε model and (d) is the streamline through a longer FPJ nozzle (L_c=240 mm) predicted with RNG k-ε model.

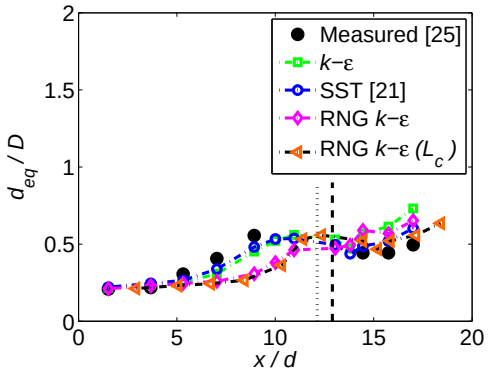

Figure 6: Axial evolution of the normalized measured and predicted equivalent diameters of the phase-averaged jet [25]. The vertical dotted and dashed lines indicate the location of the centre body's upstream surface in the conventional geometry and extended geometry (L_c=240 mm) respectively. Refer to Figure 2 for symbols and coordinates.

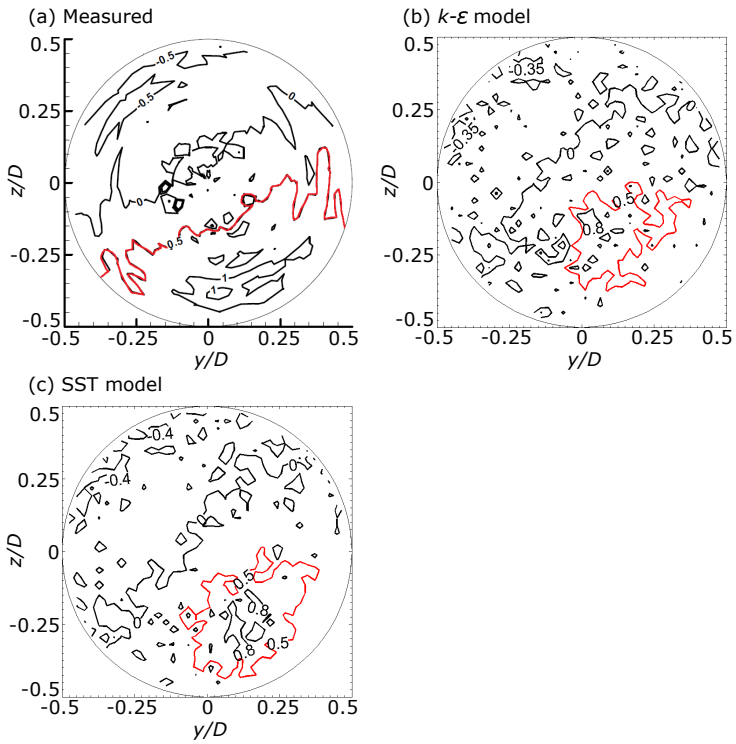

Figure 7: Cross-sectional images of the phase-averaged axial velocity contours at the transverse plane x/d=8.93 within the FPJ nozzle as obtained with: (a) the experiment [28], (b) the standard k-ε model and (c) the SST model. Data are normalized by the local centreline velocity in this plane. The red line indicates the half-width contour of the jet. Refer to Figure 2 for symbols and coordinates.

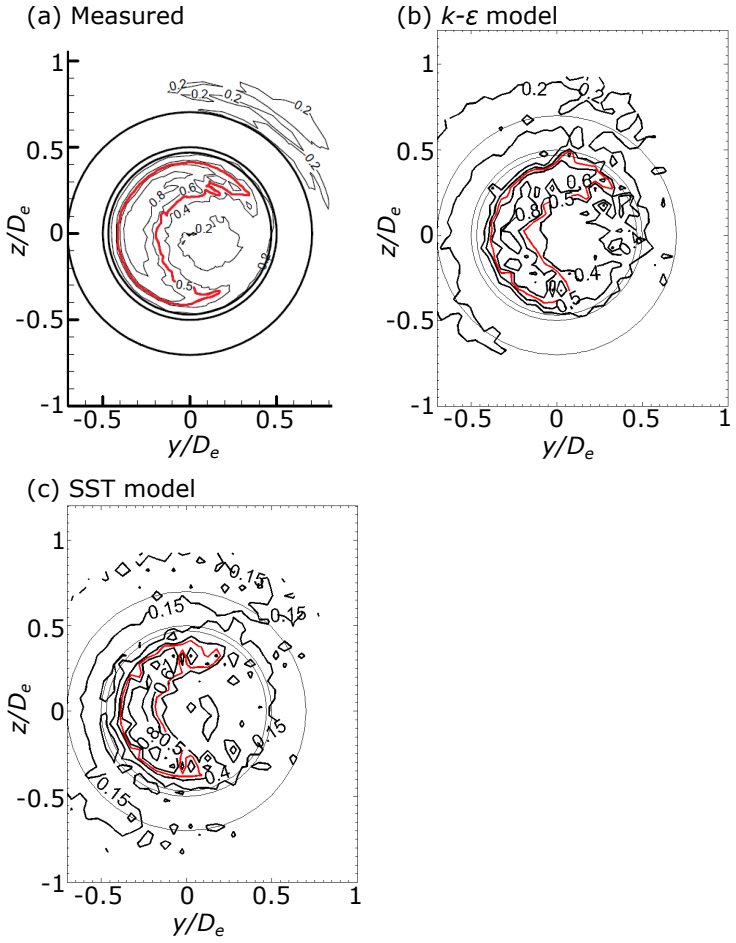

Figure 8: Phase-averaged axial velocity contours in the near external field of the FPJ nozzle, x/D_e=0.16, obtained by: (a) experiment [28], (b) the standard k-ε model and (c) the SST model. Data are normalized by the local centreline velocity in this plane. The regions enclosed by the red line indicate the area of the jet. Refer to Figure 2 for symbols and coordinates.

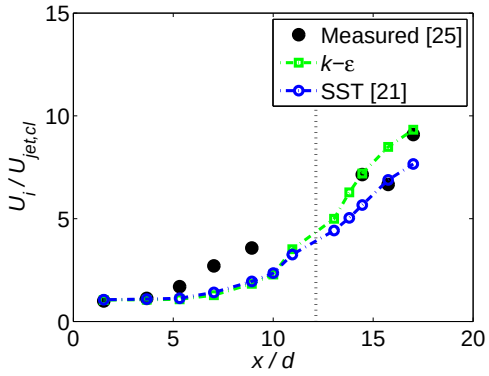

Figure 9: Measured [25] and predicted results of inverse centreline velocity decay of the phase-averaged jet. The parameter $U_{jet,cl}$ is the maximum velocity in the local plane and U_i is the bulk inlet velocity. The vertical line indicates the location of the centre body's upstream surface.

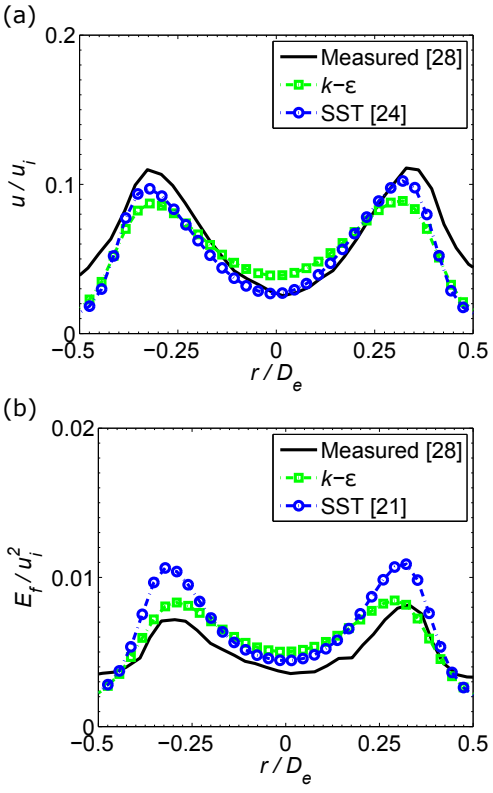

Figure 10: Measured [28] and calculated time average (a) axial velocity and (b) total fluctuation energy (E_f) profile at x'/D_e=0.16. The velocity values are normalised with the inlet velocity u_i, E_f are normalised with u_i^2 and the abscissa is normalised with the diameter of the nozzle's exit D_e.

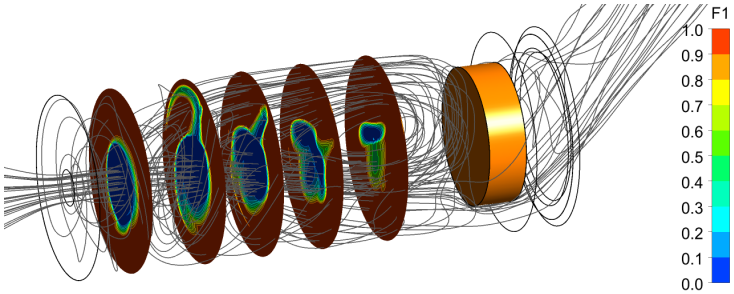

Figure 11: Contours of the value F_1 in the SST model (see Equation 16) at the five cross-section planes of x/d=1.52, 3.67, 5.32, 7.03 and 8.93, within the FPJ nozzle.

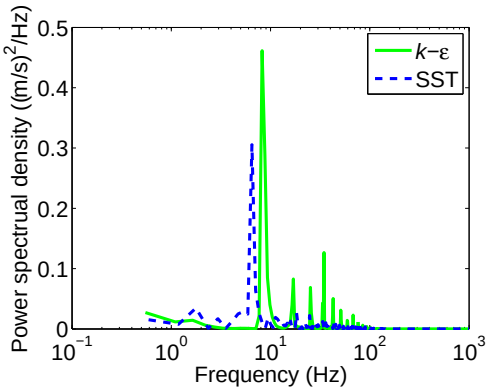

Figure 12: Predicted frequency spectrum.

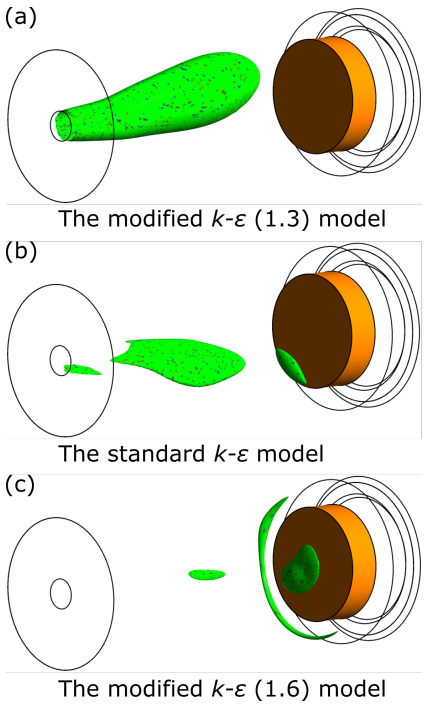

Figure 13: Iso-surface of the 200 m^2/s^2 instantaneous turbulence kinetic energy (k) predicted with (a) the modified k-ε (1.3), (b) the standard k-ε model, and (c) the modified k-ε (1.6) model.

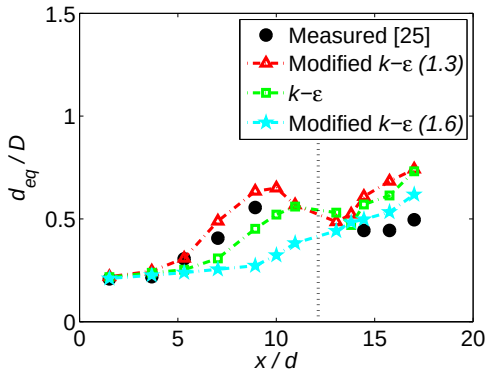

Figure 14: Axial evolution of the measured [25] and predicted equivalent diameters of the phase-averaged jet. The vertical line indicates the location of the centre body's upstream surface. Refer to Figure 2 for symbols and coordinates.

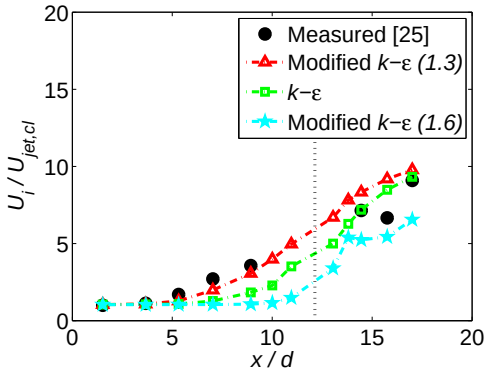

Figure 15: Measured [25] and predicted results of inverse centreline velocity decay of the phase-averaged jet. Refer to Figure 9 for symbols and coordinates.

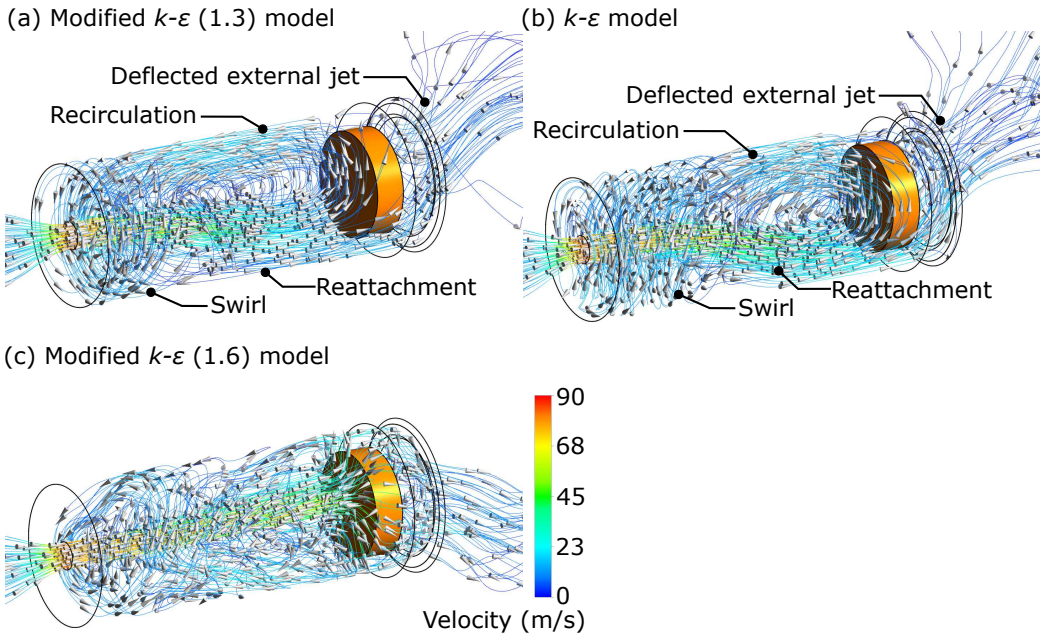

Figure 16: Three-dimensional visualisations of the predicted instantaneous streamlines through the FPJ nozzle with (a) the modified k-ε (1.3) model, (b) the standard k-ε model and (c) the modified k-ε (1.6) model.

Chapter 5

Numerical investigation on the scalar mixing of a fluidic precessing jet flow

Statement of Authorship

Title of Paper	Numerical investigation on the scalar mixing of a fluidic precessing jet flow
Publication Status	☐ Published ☐ Accepted for Publication ☑ Submitted for Publication ☐ Unpublished and Unsubmitted w ork w ritten in manuscript style
Publication Details	Chen, X., Tian, Z. F., and Nathan, G. J., 2017, "Numerical investigation on the scalar mixing of a fluidic precessing jet flow," Submitted to Journal of Fluids Engineering.

Principal Author

Name of Principal Author (Candidate)	Xiao Chen
Contribution to the Paper	Conducted literature review, developed CFD model, performed data processing and analysis, and wrote manuscript.
Overall percentage (%)	65
Certification:	This paper reports on original research I conducted during the period of my Higher Degree by Research candidature and is not subject to any obligations or contractual agreements with a third party that would constrain its inclusion in this thesis. I am the primary author of this paper.
Signature	Date 31.05.2017

Co-Author Contributions

By signing the Statement of Authorship, each author certifies that:

i. the candidate's stated contribution to the publication is accurate (as detailed above);

ii. permission is granted for the candidate in include the publication in the thesis; and

iii. the sum of all co-author contributions is equal to 100% less the candidate's stated contribution.

Name of Co-Author	Zhao Tian
Contribution to the Paper	Supervised CFD model developing, helped in data interpreting and edit manuscript.
Signature	Date 31/05/2017

Name of Co-Author	Graham Nathan
Contribution to the Paper	Supervised development of work, helped in data interpreting and edit manuscript.
Signature	Date 31/5/17

Please cut and paste additional co-author panels here as required.

Numerical investigation on the scalar mixing of a fluidic precessing jet flow

Xiao Chen, Zhao F. Tian, Graham J. Nathan*

School of Mechanical Engineering

Centre for Energy Technology (CET)

The University of Adelaide

Adelaide, South Australia, 5005

Australia

*Corresponding author. Email: graham.nathan@adelaide.edu.au.

Abstract

The first systematic numerical study of the scalar field in the external flow from a fluidic precessing jet (FPJ) nozzle, in comparison with experimental data, is reported. The simulations adopted a Hybrid-LES approach and an unsteady Shear Stress Transport (SST) model, which was previously found to give good agreement with the experimental velocity field. However, with the current numerical configuration, the SST model was found to over-predict the deflection angle of the emerging jet and to under-predict the centre-line mixing rate. The simulation with the SST model also predicts a much narrower distribution range of the pdf of the centreline concentration in the far field than the measured jet. The simulation with the Hybrid-LES approach achieves better agreement with the measured result than that with the SST model, although it is still not able to reproduce the scalar mixing of the FPJ flow well. This indicates that the simulation of the scalar field of the FPJ flow is significantly more sensitive than is the velocity field.

1 Introduction

Investigation of the scalar mixing of turbulent flows is important for applications including non-premixed combustion. Increasing the turbulent mixing will increase the molecular mixing indirectly, which causes the combustion intensity to be increased in a combustion process [1, 2]. However, predicting heat release is more complex owing to the importance of soot, whose evolution is highly non-linear. For example, lower mixing rates may sometimes be desirable since they can cause increased radiant heat transfer [3]. The fluidic precessing jet (FPJ) nozzle was invented [4] to improve heat transfer and, in turn, reduce the emissions of

NO_x through changes to the turbulent mixing for applications such as rotary kilns. These changes have been found to also increase the fuel efficiency and the quality of the product [5, 6, 7]. Some experimental measurements of the scalar field of the FPJ flow have been reported [8, 9, 10]. However, to the authors' knowledge, no numerical investigation of this flow has been reported previously. Hence the main objective of the current work is to assess the sensitivity and reliability of Computational Fluid Dynamics (CFD) methods in predicting the scalar mixing of the FPJ flow.

The modelling of the precessing jet flow is extremely challenging, owing to the highly unsteady and oscillatory nature of the precession, which increases the computational requirements over conventional jet flows. The reliability of the SST model in predicting the velocity field of the FPJ flow within and in the emerging field of the FPJ nozzle was assessed by [11]. They found the differences between their predictions and the measurements of [12] for the phase-averaged centreline velocity decay and the spreading rate to be 35.1% and 13.75%, respectively. The detailed structure of the predicted FPJ flow within the nozzle was proposed based on the critical point theory [11]. Six main vortex cores within the FPJ nozzle were identified and the vortex skeleton was developed based on the CFD simulation and previous experiments conducted by the authors' group. Their predictions of a bi-stable flow through the FPJ nozzle was also found to be consistent with experiments [13], with the solution found to converge onto one of two modes, the axial jet (AJ) and the dominant precessing jet (PJ) modes. The change of the flow structure during the mode switching process was studied numerically using an unsteady SST model [14]. This found that sufficient asymmetry within either the inflow or the initial flow field could trigger the mode switching, while the time

required for the mode switching decreases with an increase in the extent of the asymmetry [14]. However, all the above numerical investigations have reported only the velocity field within the FPJ nozzle, so that the effectiveness of the two-equation URANS models in predicting the external scalar field from this flow is still unknown.

With the rapid increase of computing power, LES methods are becoming more widely adopted to simulate scalar fields in turbulent flows. Both the velocity and scalar field of the flow in a coaxial jet mixer have been numerically studied using three LES approaches and three URANS models [15]. It was found that both the velocity and scalar field are predicted more reliably with the SST model than with the standard $k-\varepsilon$ and the Reynolds stress models. Nevertheless, a dynamic mixed LES approach was found to achieve even better agreement with the experimental data and to capture most of the flow features for this case. Similarly, an LES approach was found to give good agreement for a high-swirl number fuel injector by [16]. Good agreement with the measured results was achieved in predicting the velocity of the flow at the injector exit, the concentration of the jet in a serious of cross-sectional planes and the probability density function (pdf) at a certain position downstream from the exit. Nevertheless, full LES approaches are still too computationally intensive for many industrial scale applications. Hence Hybrid-LES methods have been adopted for some investigations [17, 18]. In Hybrid-LES approaches, an URANS model is generally employed for the near wall region, while the regions far away from wall are solved with LES. However, the reliability of Hybrid-LES approaches in predicting the scalar mixing in the FPJ flow is also unknown.

Experimental data are available to evaluate the performance of numerical mod-

els for this flow using the systematic measurements of the scalar field of the FPJ flow downstream from the nozzle exit reported by [8]. These investigations report the centreline concentration, the concentration half-width and the probability distribution function (pdf) of the centreline concentration in the far field of an FPJ flow in a confined co-flowing arrangement. It was found that the concentration decay rate of the FPJ flow in the emerging field of the nozzle exit is about four times greater than that of a free round jet [19], while it reduces suddenly at an "elbow point" (approximately at $x = 1.4\ d_{PJ}$) and the decay rate is almost constant in the region downstream from this point [10]. The effect of the co-flow velocity on the scalar field of the FPJ flow was also assessed. The ratio between the co-flow and exit velocities was found not to influence the concentration decay rate in the far field and to have only a slight effect on the spreading rate of the jet [8]. They also found that the pdf of the jet centreline concentration of the FPJ flow is broader than that for a pipe jet flow, which indicates that the range of the concentration distribution of the FPJ flow is wider.

Based on the above, given that an URANS model is sufficient to achieve reasonable agreement with the measured data in predicting the phase-averaged velocity field of the complex FPJ flow within the nozzle, the main aim of the current work is to comprehensively assess the effectiveness of two numerical simulation methods, i.e. the SST and the Hybrid-LES approaches, in predicting the resulting scalar field for a non-reacting, confined FPJ flow in a co-flow.

2 Methodology

The software CREO 2.0 and ANSYS/Design Modeler 16.5 was employed to generate a geometrically identical model of the experimental investigation of the scalar mixing of the FPJ flow reported by [8], [9] and [10].

Figure 1 presents the dimensions of the system, which comprises an FPJ nozzle confined by a parallel wall. The FPJ nozzle comprises a contraction inlet, a sudden expansion at the inlet orifice, a centre-body and a lip near to the nozzle exit. In the experiment of [10], water was adopted as the working fluid for both the co-flow and FPJ flow, while dye was injected into the FPJ flow as a marker of the scalar field. In both the experiment and the CFD model, water at 25 °C was chosen for the working fluid that was injected through the FPJ nozzle. A second fluid (called water 2) is defined for the co-flow, although its properties are identical to those of the water injected as the main FPJ flow, also to match the experiment for which the jet fluid was marked with a fluorescent dye. The velocity of the main-flow at the inlet orifice (U_{or}) was 8.8 m/s, to match the experiment, the reference co-flow velocity at the inlet plane (U_a) was 0.06 m/s, while two more co-flow velocities of 0.038 m/s and 0.11 m/s were also assessed to match the experiments. The minimum root mean square of the residuals for the convergence was set to 5×10^{-5}. A numerical study of a closely related flow showed that a time-step of 1/180th of one precession cycle is small enough to reasonably reproduce the oscillation with a two-equation URANS model [20]. Here the time-step was 0.001 s for the simulation using the SST model and 0.0001 s for the Hybrid-LES approach, corresponding to approximately 1/180th and 1/1800th of the period of each precession cycle. For the Hybrid-LES approach, the SST model

was employed for the region upstream from the exit of the FPJ nozzle, where the predicted velocity field has been validated [11], and the flow in the other region was calculated with the LES method.

Figure 2 presents the details of the present mesh, which was generated with the software ANSYS/ICEM CFD 16.5. The O-grid method was adopted, which ensures the y^+ value are less than 1 for all simulations. This structured mesh employed 8.6 million nodes.

3 Results and discussion

3.1 Cycle independence

Figure 3 presents themean centreline concentration of the FPJ flow that was calculated from 5, 10 and 15 precession cycles with mesh with 2.15 million nodes. It can be seen that the predicted centreline concentration differs little for these cases. For this reason it was deemed to have converged after 10 cycles of precession, consistent with the observation from our previous work that the cycle-to-cycle variation of the FPJ flow is small with an URANS simulation [21]. Hence all the following mean results are calculated based on the average of 10 precession cycles.

3.2 Mesh independent test

Figure 4 presents the mean centreline concentration downstream from the FPJ nozzle as predicted with three different meshes, i.e. 2.15 million, 4.3 million and 8.6 million nodes. It can be seen that the centreline concentration predicted with

2.15 million nodes is lower than that with the other two meshes at the range from $x/d_{PJ} = 1.5$ to 2, while the results that calculated with the 4.3 million nodes and 8.6 million nodes meshes are nearly converged. The 8.6 million nodes mesh was therefore adopted for all the simulations in the following sections.

3.3 Assessment of the SST model in predicting the scalar field of the FPJ flow

Figure 5 presents the mean centreline concentrations of the measured [8] and predicted FPJ flows with the co-flow velocities of $4.31 \times 10^{-3} U_{or}$, $6.8 \times 10^{-3} U_{or}$ and $12.3 \times 10^{-3} U_{or}$, using the SST model. The co-flow is entrained into the jet-core region, causing the measured centreline concentration of the jet to decay strongly [10]. While this trend has been reproduced with the SST model, the magnitudes differ greatly. The decay rate of the measured centreline concentration ($\bar{\xi}_{ja}$) reduces suddenly at an "elbow point" and $\bar{\xi}_{ja}$ decays nearly in a linear manner in the downstream region. However, for all the three flow conditions, the centreline concentrations at the "elbow points" are greatly under-predicted, although the positions of the predicted "elbow points" are close to that of the measured flows. In addition, in the region downstream from the "elbow point", the centreline concentrations of all the three simulated flows increase slightly, which is contrary to the experimental results. The differences between the measured [8] and the predicted (SST) mean centreline concentration of the three FPJ flows are 61.2%, 66.4% and 76.3%, while the positions that the maximum differences occur are all near to the "elbow points", i.e. at x=1.90 d_{PJ}, 1.97 d_{PJ} and 2.13 d_{PJ} for the flows with the co-flow velocities of $4.31 \times 10^{-3} U_{or}$, $6.8 \times 10^{-3} U_{or}$ and $12.3 \times 10^{-3} U_{or}$,

respectively.

3.4 Assessment of the Hybrid-LES approach in predicting the scalar field of the FPJ flow

Figure 6 presents the instantaneous streamlines of both the main FPJ flow and the co-flow as predicted with the SST and the Hybrid-LES approaches. The co-flow velocity for both these two cases is 0.06 m/s. The instantaneous flow enters the FPJ nozzle through the contraction inlet and reattaches to the wall of the chamber, while it precesses. A fraction of the instantaneous flow is deflected and reversed towards the inlet of the chamber from the upstream surface of the centre-body to form a swirling flow in the upstream region, while the other part of the flow leaves the chamber with a deflected angle to the nozzle axis of approximately 30 to 60°. More detailed structure of the internal FPJ flow is reported by [11]. Different from a conventional round jet, the instantaneous FPJ flow is directed at any instant toward one side of the nozzle in the region immediately downstream from the nozzle exit. The precession of this deflected jet enhances the bulk mixing between the FPJ flow and the co-flow, especially in the near field [10]. Figure 6 shows that the velocity fluctuation predicted with the Hybrid-LES approach is larger than that with the SST model. This is because LES solves a filtered form of the Navier-Stokes equations, which resolves the larger scales of motion directly and models the sub-grid-scale motions. However the URANS model solves only the averaged form of the Navier-Stokes equations. In addition, although the predicted deflected angles of the emerging jets for the two approaches are similar, it is obvious that the FPJ flow predicted with the LES method mixes more strongly with the co-flow

along the axis than is predicted with the SST model.

Figure 7 presents the iso-surface of the Q-criterion at Q = 200 s^{-2} for the instantaneous FPJ flows that predicted with the SST and the Hybrid-LES approaches downstream from the nozzle exit. Here Q is defined as:

$$Q = \frac{1}{2}(\Omega^2 - S^2) \quad , \tag{1}$$

where Ω is the vorticity and S is the strain rate [22]. The visualized turbulent structures in the two predicted FPJ flows provide further evidence that much greater range of turbulent scales were predicted with the Hybrid-LES than with the SST model, which averages the precession motion.

Figure 8 presents the cross-sectional contours of the instantaneous and mean concentration in the jets as predicted with the SST and the Hybrid-LES approaches, in comparison with the measured data [8]. It can be seen that the predicted deflection angle between the instantaneous jet and the nozzle axis is larger than that of the measured flow for both cases. This results in the mean flow having being predicted to have both a greater mean spreading and a scalar field in which the jet fluid being preferentially concentrated away from the axis. This contrasts the experimental mean image, in which the jet fluid is always most concentrated on the nozzle axis. This is particularly evident in the flow predicted with the SST model, which is much better converged than the flow predicted with the Hybrid-LES approach. The SST model predicts the jet fluid to spread in a cone toward the walls of the confining cylinder and to be preferentially concentrated close to these walls in the region downstream from $x = 4d_{PJ}$. That is, in this region, the jet concentration is greater than that near to the axis, so that it does not converge back to

the axis or mix effectively with the co-flow. The region with the lowest centreline jet concentration is found at x=2 d_{PJ}, while the concentration increases gradually along the centreline, which is consistent with the result presented in Figure 5. The Hybrid-LES approach achieves better agreement with the measured results than does the SST model. This is consistent with the Hybrid-LES method predicting more accurately the return of the precessing jet to the nozzle axis, and with greater variability in the cycle-to-cycle oscillations of the jet. The greater cycle-to-cycle variability predicted with the Hybrid-LES approach is also evident from the lower degree of convergence evident from the mean field of this flow relative to that calculated with the SST model. However, the $\bar{\xi}_{ja}$ was still under-predicted with the Hybrid-LES approach. This may due to the less cycle-to-cycle variation of the jet at the nozzle exit that predicted with the SST model.

Figure 9 presents a comparison of the measured [8] and predicted mean centreline concentration for both the SST and the Hybrid-LES approaches. It can be seen that, both the SST and the Hybrid-LES approaches over-predict the centreline concentration upstream from x=0.4 d_{PJ}, while under-predicting it in the downstream region. This is consistent with the observation from the cross sectional images (Figure 8) that the numerical approaches both over-predict the deflection angle of the emerging instantaneous jet and also under-predict the rate at which the local jet returns back to the nozzle axis. Similarly, the position of the intersection point between the emerging jet and the nozzle axis is predicted to be further upstream than that of the measured jet. The rapid centreline concentration decay upstream from x=1.8 d_{PJ} is over-predicted with both the SST and the Hybrid-LES approaches, while the centreline concentration converges back closer to the experimental values toward the downstream end of the domain. The differ-

ence between the measured [8] and calculated mean centreline concentration is 52.6% for the Hybrid-LES approach, while the maximum error occurs near to the "elbow" point, i.e. at x=2.76 d_{PJ}.

Figure 10 presents the measured [8] and predicted normalized probability distribution function (pdf) of the centreline concentration of the FPJ flow at x=12 d_{PJ}, using both the Hybrid-LES and the SST model. It can be seen that the pdf of the measured $\xi/\bar{\xi}$ is widely distributed, especially in the range from 0.5 to 1.5, which indicates the wide range of mixing length scales in the FPJ flow. For the flow predicted with the SST model, the distribution of $\xi/\bar{\xi}$ is preferentially biased near to two peaks at $\xi/\bar{\xi}$ = 0.85 and 1.2. This is consistent with the finding of [21] that the cycle-to-cycle variation of the FPJ flow that predicted with an URANS model is small, since this will distribute the scalar in the same way each cycle. That is, it suggests that the large cycle-to-cycle variability in the FPJ flow that has been observed experimentally [8] may be important in generating the measured flow-field. The Hybrid-LES approach generates a more uniform distribution in the values of $\xi/\bar{\xi}$ over the range 0.75 to 1.25, although it is still significantly narrower than the experimental distribution. This is also consistent with the greater cycle-to-cycle variability of the flow predicted with the Hybrid-LES approach than that with the SST model.

4 Conclusions

Both the SST and the Hybrid-LES approaches over-predict the angle at which the instantaneous jet is deflected from the nozzle axis as it emerges from the nozzle. This results in the jet fluid being predicted to be preferentially distributed away

from the axis throughout the measurement region experimentally, in contrast to the measured data where the highest concentration is always on the axis. The discrepancy is greater with the SST model than with the Hybrid-LES approach. An "elbow point" in the mean centreline concentration decay is predicted with both of the approaches, consistent with the experiments, although the quantitative values differ significantly. For the case with co-flow velocity of $6.8 \times 10^{-3} U_{or}$, the differences between the predicted and measured mean centreline concentration are 52.6% and 66.4% for the Hybrid-LES and the SST approaches. For the cases with two other co-flow velocities of $4.31 \times 10^{-3} U_{or}$ and $12.3 \times 10^{-3} U_{or}$, these differences are 61.2% and 76.3% for the SST approach.

The Hybrid-LES approach predicts a wider range of the $\xi/\bar{\xi}$ distribution at x=12 d_{PJ} than does the SST model, although it is still narrower than the experimental distribution. This is attributed to the Hybrid-LES predicting a significantly greater range of turbulent scales, so that the predicted precessing jet mixes more strongly with the co-flow and the cycle-to-cycle variability is predicted to be much greater than that with the SST model.

Although the Hybrid-LES approach gives better agreement with the measured data than does the SST model in predicting the jet concentration distribution downstream from the nozzle exit, especially the return of the precessing jet to the nozzle axis, both the two approaches did not reproduce the external scalar field of the FPJ flow well with the current numerical configuration. A possible reason is that the cycle-to-cycle variation of the leaving jet at the nozzle exit is predicted to be small with the SST model. Work is in progress to optimize the numerical model by increasing the variability of the deflection angle of the emerging jet, which is consistent with previous experimental observation.

5 Acknowledgement

The first author was supported by the Divisional Scholarship of the faculty of ECMS, the University of Adelaide. The authors also acknowledge the support of the Australian Research Council for Grant DP150102230.

References

[1] Buch, K. A., and Dahm, W. J., 1998. "Experimental study of the fine-scale structure of conserved scalar mixing in turbulent shear flows. part 2. sc $\approx$ 1". *Journal of Fluid Mechanics,* **364**, pp. 1–29.

[2] Pitsch, H., and Steiner, H., 2000. "Scalar mixing and dissipation rate in large-eddy simulations of non-premixed turbulent combustion". *Proceedings of the Combustion Institute,* **28**(1), pp. 41–49.

[3] Nathan, G. J., Mi, J., Alwahabi, Z. T., Newbold, G. J. R., and Nobes, D. S., 2006. "Impacts of a jet's exit flow pattern on mixing and combustion performance". *Progress in Energy and Combustion Science,* **32**(5-6), pp. 496–538.

[4] Nathan, G. J., and Luxton, R. E., 1988. Controlling the motion of a fluid jet.

[5] Manias, C. G., and Nathan, G. J., 1993. "The precessing jet gas burner: a low nox burner providing process efficiency and product quality improvements". *World Cement,* **24**(3), pp. 4–11.

[6] Manias, C. G., and Nathan, G. J., 1994. "Low nox clinker production". *World Cement,* **25**(5), pp. 54–56.

[7] Videgar, R., 1997. "Gyro-therm technology solves burner problems: The application of new gyro-therm burner technology in the durkee plant". *World Cement,* **28**, pp. 39–45.

[8] Parham, J., 2000. "Control and optimisation of mixing and combustion from a precessing jet nozzle". Thesis.

[9] Parham, J. J., Nathan, G. J., and Alwahabi, Z. T., 2001. "Quantification of mixing characteristics for the optimisation of combustion in rotary kilns". In 14th Australasian Fluid Mechanics Conference, Adelaide, Australia, pp. 10–14.

[10] Parham, J., Nathan, G., Hill, S., and Mullinger, P., 2005. "A modified thring-newby scaling criterion for confined, rapidly spreading and unsteady jets". *Combustion science and technology,* **177**(8), pp. 1421–1447.

[11] Chen, X., Tian, Z. F., Kelso, R. M., and Nathan, G. J., 2017. "The topology of a precessing flow within a suddenly expanding axisymmetric chamber". *ASME J. Fluids Eng.* 10.1115/1.4035950.

[12] Wong, C. Y., Lanspeary, P. V., Nathan, G. J., Kelso, R. M., and O'Doherty, T., 2003. "Phase-averaged velocity in a fluidic precessing jet nozzle and in its near external field". *Experimental Thermal and Fluid Science,* **27**(5), pp. 515–524.

[13] Nathan, G. J., Hill, S. J., and Luxton, R. E., 1998. "An axisymmetric 'fluidic'nozzle to generate jet precession". *Journal of Fluid Mechanics,* **370**(1), pp. 347–380.

[14] Chen, X., Tian, Z., Kelso, R., and Nathan, G., 2017. "New understanding of mode switching in the fluidic precessing jet flow". *Accepted by ASME J. Fluids Eng.*

[15] Tkatchenko, I., Kornev, N., Jahnke, S., Steffen, G., and Hassel, E., 2007. "Performances of les and rans models for simulation of complex flows in a coaxial jet mixer". *Flow, Turbulence and Combustion,* **78**(2), pp. 111–127.

[16] Cheng, L., Dianat, M., Spencer, A., and McGuirk, J. J., 2012. "Validation of les predictions of scalar mixing in high-swirl fuel injector flows". *Flow, turbulence and combustion,* **88**(1-2), pp. 143–168.

[17] Abe, K.-i., and Ohtsuka, T., 2010. "An investigation of les and hybrid les/rans models for predicting 3-d diffuser flow". *International Journal of Heat and Fluid Flow,* **31**(5), pp. 833–844.

[18] Jakirlić, S., Kadavelil, G., Kornhaas, M., Schäfer, M., Sternel, D., and Tropea, C., 2010. "Numerical and physical aspects in les and hybrid les/rans of turbulent flow separation in a 3-d diffuser". *International Journal of Heat and Fluid Flow,* **31**(5), pp. 820–832.

[19] Becker, H., Hottel, H., and Williams, G., 1967. "The nozzle-fluid concentration field of the round, turbulent, free jet". *Journal of Fluid Mechanics,* **30**(02), pp. 285–303.

[20] Guo, B., Langrish, T., and Fletcher, D., 2001. "Numerical simulation of unsteady turbulent flow in axisymmetric sudden expansions". *ASME J. Fluids Eng.,* **123**, p. 574.

[21] Chen, X., Tian, Z., and Nathan, G., 2012. "Numerical simulation of the flow within a fluidic precessing jet nozzle". In Australasian Fluid Mechanics Conference (18th: 2012: Launceston, Tasmania).

[22] Jeong, J., and Hussain, F., 1995. "On the identification of a vortex". *Journal of fluid mechanics,* **285**, pp. 69–94.

Figures

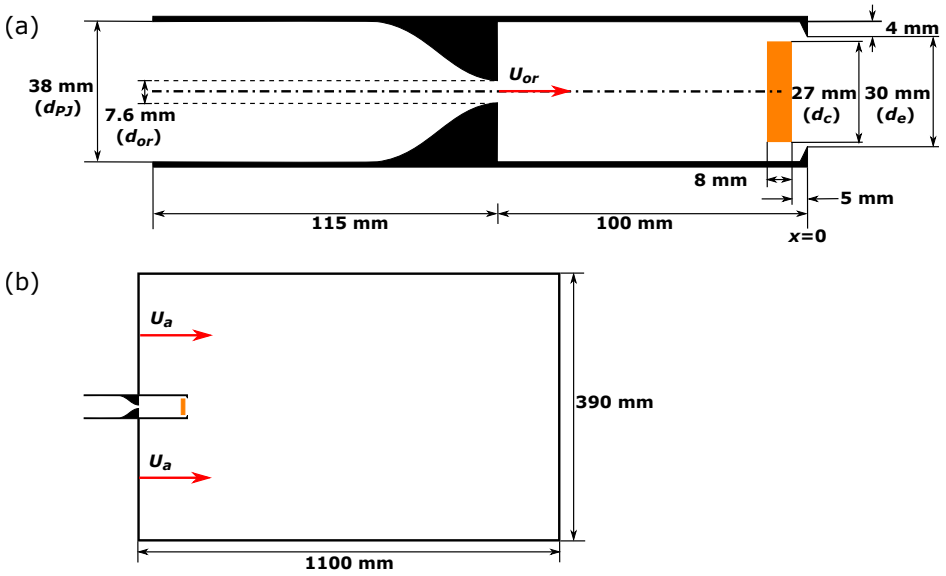

Figure 1: The dimensions of (a) the FPJ nozzle and (b) the external confinement adopted in the current simulation, where d_{PJ}, d_{or}, U_{or} and U_a are the diameters of the nozzle chamber, diameter of the nozzle's inlet, nozzle's inlet velocity and co-flow velocity, respectively.

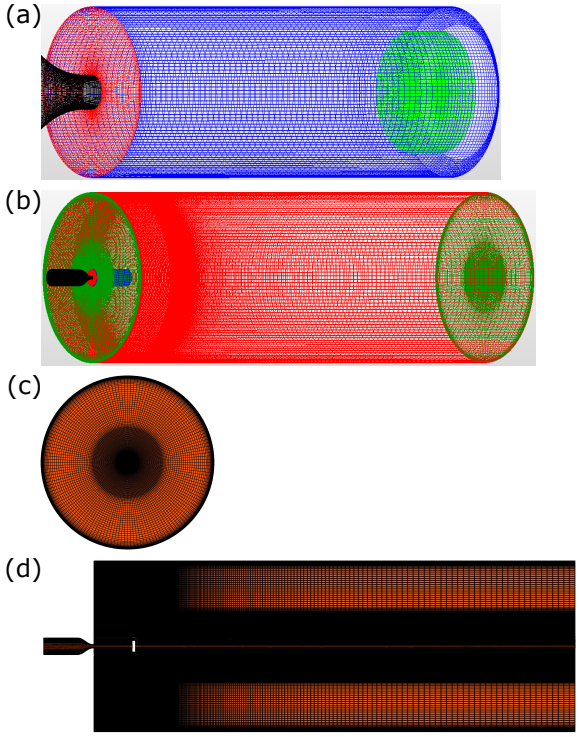

Figure 2: Mesh of the model. (a) The FPJ nozzle, (b) the whole fluid domain, (C) the cross-sectional plane and (d) the longitudinal plane through the whole domain.

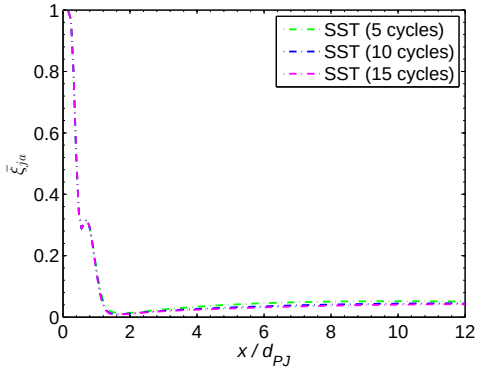

Figure 3: Mean centreline concentration of the predicted precessing jet for the assessment of convergence for the cases of 5, 10 and 15 precession cycles, where the ξ_{ja} is the centreline concentration. Refer to Figure 1 for other symbols and coordinates.

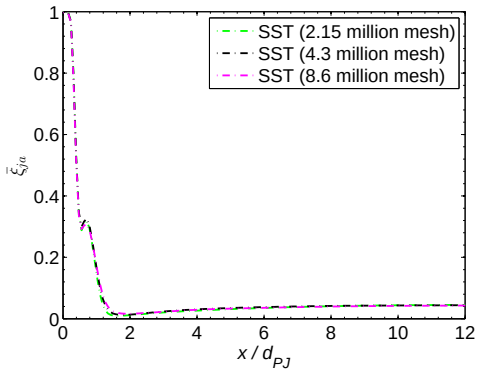

Figure 4: Mean centreline concentrations of the precessing jet flow for the assessment of convergence for the cases predicted with 2.15, 4.3 and 8.6 million nodes. Refer to Figure 1 for other symbols and coordinates

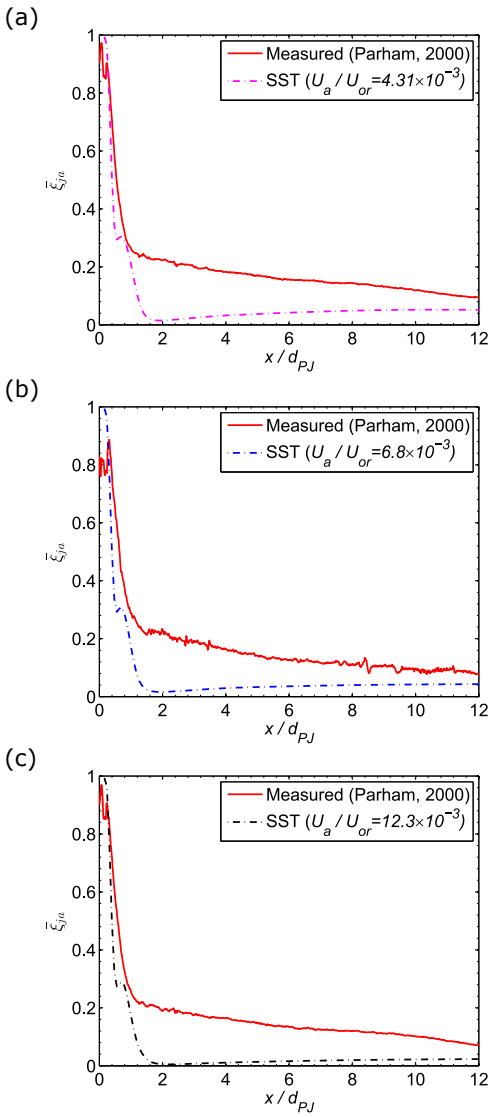

Figure 5: Measured [8] and predicted mean centreline concentration of the FPJ flow with co-flow velocities of (a) $4.31 \times 10^{-3} U_{or}$, (b) $6.8 \times 10^{-3} U_{or}$ and (c) $12.3 \times 10^{-3} U_{or}$. Refer to Figure 1 for other symbols and coordinates.

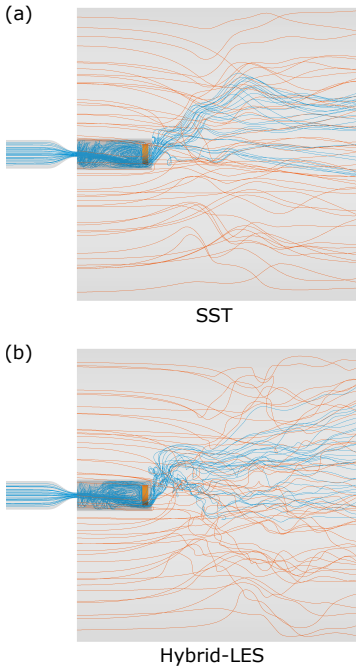

Figure 6: Visualisations of the instantaneous streamlines through the FPJ nozzle and the external co-flow as predicted with (a) the SST and (b) the Hybrid-LES approaches.

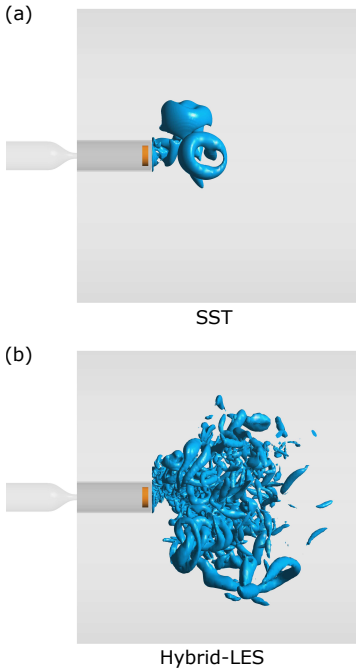

Figure 7: Iso-surface of the Q-criterion at $Q = 200\ s^{-2}$ in the region downstream from the nozzle exit for the instantaneous FPJ flows as predicted with (a) the SST and (b) the Hybrid-LES approaches. Refer to Equation 1 for the definition of Q.

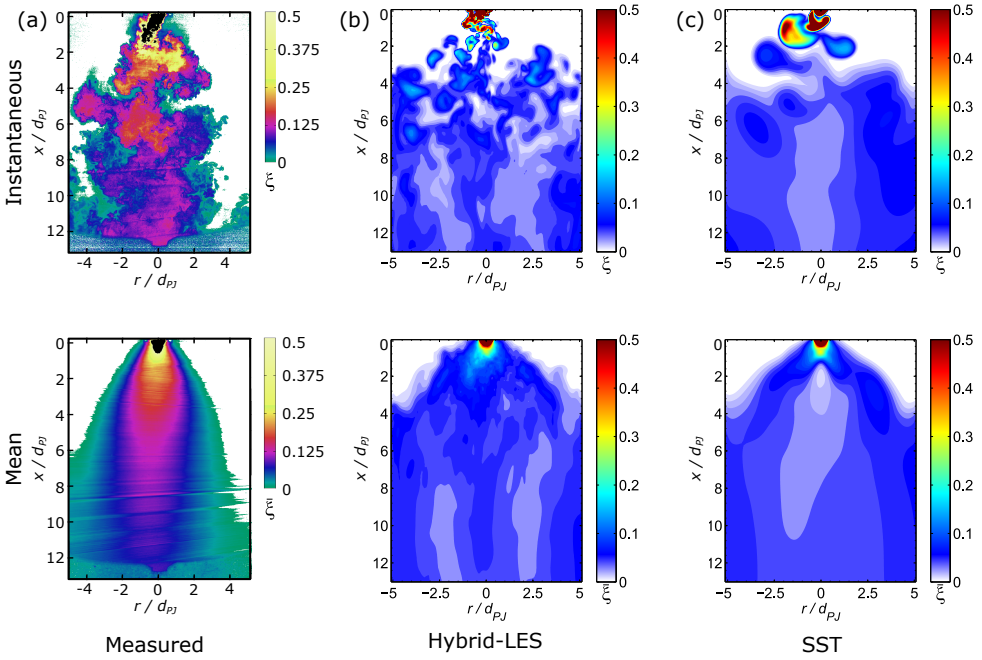

Figure 8: Cross-sectional instantaneous and mean concentration contours of the FPJ flows that were (a) measured [8] and predicted with (b) the Hybrid-LES and (c) the SST approaches.

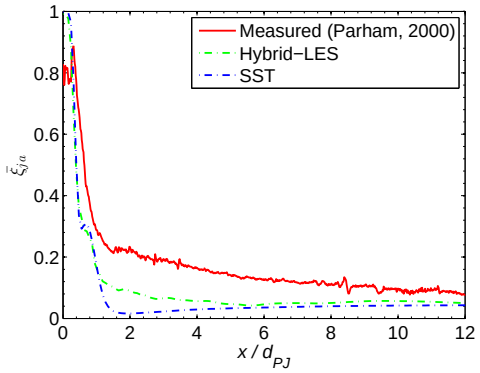

Figure 9: Measured [8] and predicted mean centreline concentrations. Refer to Figure 1 for symbols and coordinates.

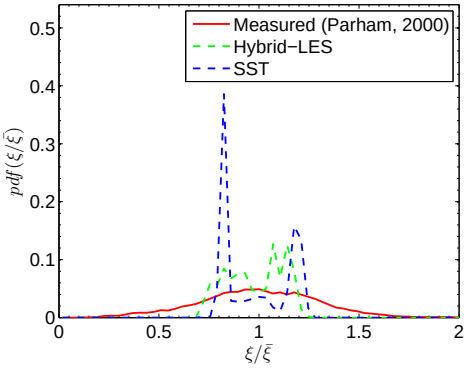

Figure 10: Measured [8] and predicted probability distribution function (pdf) of the concentration on the jet axis (ξ) that is normalized by the local mean concentration ($\bar{\xi}$) at $x = 12\ d_{PJ}$. Here the predicted pdf data was based on the result of 10 precession cycles. Refer to Figure 1 for symbols and coordinates.

Chapter 6

The topology of a precessing flow within a suddenly expanding axisymmetric chamber

Statement of Authorship

Title of Paper	The Topology of a Precessing Flow Within a Suddenly Expanding Axisymmetric Chamber
Publication Status	☐ Published ☑ Accepted for Publication ☐ Submitted for Publication ☐ Unpublished and Unsubmitted w ork w ritten in manuscript style
Publication Details	Chen, X., Tian, Z. F., Kelso, R. M., and Nathan, G. J., 2017, "The Topology of a Precessing Flow Within a Suddenly Expanding Axisymmetric Chamber," Journal of Fluids Engineering, 139(7), pp. 071201-071201-071210.

Principal Author

Name of Principal Author (Candidate)	Xiao Chen
Contribution to the Paper	Conducted literature review, developed CFD model, performed data processing and analysis, and wrote manuscript.
Overall percentage (%)	65
Certification:	This paper reports on original research I conducted during the period of my Higher Degree by Research candidature and is not subject to any obligations or contractual agreements with a third party that would constrain its inclusion in this thesis. I am the primary author of this paper.
Signature	Date: 31.05.2017

Co-Author Contributions

By signing the Statement of Authorship, each author certifies that:

i. the candidate's stated contribution to the publication is accurate (as detailed above);

ii. permission is granted for the candidate in include the publication in the thesis; and

iii. the sum of all co-author contributions is equal to 100% less the candidate's stated contribution.

Name of Co-Author	Zhao Tian
Contribution to the Paper	Supervised CFD model developing, helped in data interpreting and edit manuscript.
Signature	Date: 31/05/2017

Name of Co-Author	Richard Kelso
Contribution to the Paper	Helped in the development of vortex skeleton.
Signature	Date: 31. 5 . 2017

Name of Co-Author	Graham Nathan		
Contribution to the Paper	Supervised development of work, helped in data interpreting and edit manuscript.		
Signature		Date	31/5/17

Please cut and paste additional co-author panels here as required.

Chen, X., Tian, Z.F., Kelso, R.M. and Nathan, G.J. (2017). The topology of a precessing flow within a suddenly expanding axisymmetric chamber. *Journal of Fluids Engineering*, 139(7), 071201 (10 pages)

Chapter 7

New understanding of mode switching in the fluidic precessing jet flow

Statement of Authorship

Title of Paper	New Understanding of Mode Switching in the Fluidic Precessing Jet Flow
Publication Status	☐ Published ☑ Accepted for Publication ☐ Submitted for Publication ☐ Unpublished and Unsubmitted w ork w ritten in manuscript style
Publication Details	Chen, X., Tian, Z. F., Kelso, R. M., and Nathan, G. J., 2017, "New Understanding of Mode Switching in the Fluidic Precessing Jet Flow," Journal of Fluids Engineering, 139(7), pp. 071102-071102-071110.

Principal Author

Name of Principal Author (Candidate)	Xiao Chen
Contribution to the Paper	Conducted literature review, developed CFD model, performed data processing and analysis, and wrote manuscript.
Overall percentage (%)	65
Certification:	This paper reports on original research I conducted during the period of my Higher Degree by Research candidature and is not subject to any obligations or contractual agreements with a third party that would constrain its inclusion in this thesis. I am the primary author of this paper.
Signature	Date: 31.05.2017

Co-Author Contributions

By signing the Statement of Authorship, each author certifies that:

i. the candidate's stated contribution to the publication is accurate (as detailed above);

ii. permission is granted for the candidate in include the publication in the thesis; and

iii. the sum of all co-author contributions is equal to 100% less the candidate's stated contribution.

Name of Co-Author	Zhao Tian
Contribution to the Paper	Supervised CFD model developing, helped in data interpreting and edit manuscript.
Signature	Date: 31/05/17

Name of Co-Author	Richard Kelso
Contribution to the Paper	Helped in the development of vortex skeleton.
Signature	Date: 31.05.2017

Name of Co-Author	Graham Nathan		
Contribution to the Paper	Supervised development of work, helped in data interpreting and edit manuscript.		
Signature		Date	31/5/19

Please cut and paste additional co-author panels here as required.

Chen, X., Tian, Z.F., Kelso, R.M. and Nathan, G.J. (2017). New understanding of mode switching in the fluidic precessing jet flow. *Journal of Fluids Engineering*, 139(7), 071102 (10 pages)

Chapter 8

Conclusions and Future Work

8.1 Conclusions

The precessing flow generated by a suddenly expanding axisymmetric nozzle has been investigated. The overall objective of this work is to better understand the strengths and limitations of the best established two-equation URANS methods in modelling the complex and unsteady FPJ flow and to further understand the flow mechanism. Therefore, this thesis mainly contains two part of compositions. Firstly, the reliability of the adopted CFD approaches in predicting both the velocity and the scalar field of the FPJ flow was assessed systematically (Chapter 4 and Chapter 5). The unsteady SST model, which achieved good qualitative and reasonable quantitative agreement with measured internal velocity field, was then chosen for the development of the topology model of the flow structure (Chapter 6) and the investigation of the mode switching phenomenon of the FPJ flow (Chapter 7).

8.1.1 Reliability of numerical approaches in predicting the FPJ flow

The velocity field of the FPJ flow within and in the emerging field of the nozzle was simulated with five two-equation URANS models, namely the SST model, the standard k-ε model, the RNG k-ε model, the modified k-ε (1.3) model and the modified k-ε (1.6) model.

A strong correlation was found between the extent to which any of the adopted two-equation URANS models reproduce the four qualitative features associated with the FPJ flow and the extent to which they reproduce the phase-averaged rate of spread and decay of the local jet within the chamber. This highlights the importance of reproducing these features as a requisite to reasonable modelling of the FPJ flow. The SST model, the standard k-ε model and the modified k-ε (1.3) model yield good qualitative agreement with both the phase-averaged flows measured experimentally and the key instantaneous features observed from flow visualisation. Among these three models, the spreading and decay rate of the

phase-averaged jet are simulated most accurately with the modified k-ε (1.3) model, while it failed to reproduce well the jet in the emerging field. Both the standard k-ε model and the SST model achieved the best overall performance in predicting the FPJ flow among the five two-equation URANS models assessed in the current work, although they did not reproduce the flow perfectly, especially in the emerging field. This may because that the pressure gradients within and near to the exit of the chamber are too complex for a single set of constants in the URANS models to reliably reproduce all regions of the flow through it.

The SST model and the Hybrid-LES approaches were chosen to simulate the external scalar field of the FPJ flow. For the Hybrid-LES approach, the SST model was adopted for the simulation of the flow upstream from the nozzle exit, while LES method was employed for the other region. The predicted results were compared directly against the measured data from the work of Parham (2000).

It was found that the predicted jet fluid is preferentially distributed away from the axis throughout the measurement region, in contrast to the measured data where the highest concentration is always on the axis. This is because that the angle at which the instantaneous jet is deflected from the nozzle axis as it emerges from the nozzle is over-predicted with both the two approaches, while the discrepancy is greater with the SST model than with the Hybrid-LES approach. This is consistent with the result of velocity field simulation that the emerging jet has not been reproduced well with the SST model, while this discrepancy was further amplified in the simulation of external scalar field. Nevertheless, the "elbow point" in the mean centreline concentration decay was predicted with both the two approaches, which is consistent with the measurement. The overall differences between the measured mean centreline concentration and that predicted with the SST model are 61.2%, 66.4% and 76.3% for the cases with co-flow velocities of $4.31 \times 10^{-3} U_{or}$, $6.8 \times 10^{-3} U_{or}$ and $12.3 \times 10^{-3} U_{or}$, respectively. Better agreement in predicting the mean centreline concentration for the case with co-flow velocity of $6.8 \times 10^{-3} U_{or}$ was achieved with the Hybrid-LES approach, with a difference of 52.6%.

The Hybrid-LES approach predicts a wider range of the $\xi/\bar{\xi}$ distribution at x=12 d_{PJ} than does the SST model, although it is still narrower than the experimental distribution. This is attributed to that the Hybrid-LES predicted a greater range of turbulent scales of the jet, which leads to a stronger mixing with the co-flow and a relatively greater cycle-to-cycle

variability than that predicted with the SST model.

Neither of the SST and the Hybrid-LES approaches reproduced the external scalar field of the FPJ flow well under the current numerical configuration. This may due to the under-predicted cycle-to-cycle variation of the emerging jet for both the two approaches. However, both the SST model and the standard k-ε model demonstrated the capability to reproduce the mean value and periodic components of the internal velocity field of the precessing jet, which is important to the further investigations of the flow structure within the nozzle chamber and the mode switching phenomenon of the FPJ flow.

8.1.2 Topological model of the structure of the FPJ flow

The unsteady SST model, which showed good qualitative and reasonable quantitative agreement against measured data in predicting the internal velocity field of the FPJ flow, was chosen for the study of the internal flow structure. Based on the results of both the previous experiments and the CFD model, the first complete topological model of the ensemble-averaged structure of the FPJ flow within the nozzle chamber has been derived using the critical point method.

Six main vortex cores were identified (refer to Figure 18 in Chapter 6 for vortex cores mentioned in this section). The dominant vortex within the chamber is a loop vortex (Vortex Core A) that originates at the inlet orifice as a dominant stream-wise vortex positioned asymmetrically within the shear layer of the reattaching jet, undergoes a loop upstream from the centre-body and terminates at a focus on the wall of the chamber. The presence of one dominant vortex within the jet, instead of a pair of symmetrical, counter-rotating steam-wise vortices, is consistent with the azimuthal pressure field and the jet precession. The presence of the "loop" upstream from the centre-body is consistent with the generation of a reverse flow by the presence of the centre-body.

Two vortex cores are connected to the dominant vortex, termed Vortex Cores B and C. Vortex Core B is deduced to be driven by the interaction of the dominant flow with the entrained ambient flow that is induced upstream into the chamber around the centre body. Vortex Core C is driven by interaction of the dominant flow with the well-known upstream swirling flow that has been observed consistently in experimental investigations. The final vortex core within the chamber, Vortex Core D, is an annular vortex. Vortex Core D is similar

to that which surrounds any reattaching jet within a cylinder, but is asymmetrical due to the asymmetry of the instantaneous flow-field.

Two other vortex cores are found in the region downstream from the centre-body, although one also extends into the upstream region. The vortex loop that is found within the induced jet that extends into the external field at one end (vortex F), also extends into the chamber and forms a loop upstream from the centre-body. Each end of the loop of the final vortex (Vortex Core E) terminates as a focus on the downstream face of the centre body, consistent with the gradients in the emerging jet, which turn the jet across the face of the centre-body.

It is also found that all the vortex cores are associated with the asymmetry of the FPJ flow. Hence, the flow has a series of inter-locking features that are all mutually independent. Their collective features are responsible for driving the FPJ flow to precess.

8.1.3 Investigation of the mode switching phenomenon of the FPJ flow

The mode switching phenomenon of the bi-stable FPJ flow was studied systematically for the first time using the unsteady SST model. Three methods to trigger the mode switch were used, namely imposing a continuous axial perturbation onto part of the inlet flow, imposing a continuous swirling component to the inlet flow and adopting a slightly asymmetric initial flow field. The change of the flow structure during the mode switching process was also reported.

It was found that sufficient asymmetry within either the inflow or the initial flow field is necessary to trigger the flow to switch from the AJ to the PJ modes in an URANS simulation. Furthermore, the time required to trigger the mode switching decreases with an increase in the extent of the imposed asymmetry. This, together with the experimental observation that the mode switching is a rare event, implies that sufficient asymmetry is also needed within the instantaneous flow to generate mode switching for a real flow. It also suggests that the converse is also likely to apply, that is, that the natural FPJ flow will occasionally generate an axisymmetric flow as an alternative rare event, causing the flow to switch back to the AJ mode again, although direct tests are required to verify this.

The changes to the flow structure during the transition process from the AJ to the PJ modes can be divided into four stages (refer to Figures 12-15 in Chapter 7 for vortex cores

mentioned in this section):

- A dominant, and asymmetric Vortex Core A is generated within the jet in the first stage, which originates at the nozzle inlet and terminates as a focus on the upstream surface of the centre-body. Three approximately symmetrical ring-shaped vortex cores are also generated at successive axial distances between the inlet and the exit plane (Vortex Cores D, C and E).

- In the second stage, Vortex Core C, which is found upstream from the centre-body, is stretched and distorted by the bias of the primary jet, while the embedded Vortex Core A connects to Vortex Core C. Due to the reversed flow, two new vortex cores (A1 and B) are then generated in the region opposite to the bias of the primary jet. Both of these two vortex cores originate from the chamber wall and connect to Vortex Core C. In addition, the ring-shaped Vortex Core E downstream from the centre-body is distorted and broken into two vortex cores (E1 and E2) due to the asymmetry in the emerging jet. One ends of these two vortex cores originate at the downstream surface of the centre-body, while the other ends extend to infinity.

- The primary jet reattaches to the wall of the chamber in the third stage, which causes Vortex Core C (upstream from the centre-body) to break. Part of the original Vortex Core C merges with the embedded Vortex Core A, while the other part moves to the most upstream region to terminate as a focus on the chamber wall.

- Finally, the loop Vortex Core F is generated with the flow that is induced from the downstream region of the centre-body. The two ends of this vortex are deduced to terminate as two foci at the exit of the chamber.

It is found that the rates of spreading and maximum axial velocity of the jet in cross-sectional planes within the nozzle increase gradually during the mode switching process. This is consistent with expectation, because increased streamline curvature is typically associated with increased velocity decay.

Consistent with a similar swirling flow (Guo et al. 2002), the predicted precession direction is found to be opposite to that of the imposed swirl at the contraction inlet. Moreover, an increase in the swirl number at the nozzle inlet leads to a decrease of the precession

frequency. This understanding, together with that of the method used to trigger the mode switching can be used to design improved nozzles for industrial applications and to guide future numerical investigations on reacting and non-reacting FPJ flows.

8.2 Future Work

Further understanding on the mechanism of the precessing jet flow is provided in this thesis. Some potential researching topics of the FPJ flow are then raised based on the findings of this work.

8.2.1 Simulating the FPJ flow with an LES approach

Five two-equation URANS models were chosen to simulate the velocity field of the FPJ flow. Good qualitative and reasonable quantitative agreement against the measured result jet was achieved by using both the SST and the k-ε models in the current work. An LES method, which is able to resolve large scale eddies, can be adopted to further improve the numerical model in the future work. Moreover, simulation using an LES method will provide more details on the instantaneous FPJ flow.

8.2.2 Effect of fluctuation in the flow on the scalar field simulation

The scalar concentration distribution downstream the nozzle exit has not been reproduced well with both the SST and the Hybrid-LES approaches in the current work. This may be due to the small cycle-to-cycle variation of the predicted flow within the FPJ nozzle. Hence the effect of the flow fluctuation on the accuracy of the scalar field simulation can be assessed in a further investigation. It is expected that imposing random perturbations to the inflow will increase the variability of the deflection angle of the emerging jet, which is consistent with previous experimental observation.

8.2.3 Sensitivity of geometric configurations on the structure of the FPJ flow

To match the previous experiments, the structure of the flow generated with only one typical FPJ nozzle was assessed in the current work. Hence the sensitivity of the geometric parameters, such as the position of the centre-body and the ratio between the length and the diameter of the nozzle chamber (L/D), on the flow structure is worth further investigation.

In addition, the structure of the flow through the FPJ nozzles with a pipe inlet and an orifice inlet could be assessed in future studies to reveal the effect of the inlet geometry on the flow structure.

8.2.4 Effect of the asymmetries on the mode switching time

It was found in this study that an increase in the extent of asymmetry in either the inflow or the initial flow field leads to a faster mode switching of the predicted FPJ flow. Further experimental works can be conducted to quantitatively study the relationship between the extent of asymmetry and the time required for mode switching of the FPJ flow, which contributes to the design of the nozzle. A parameter that describes the extent of asymmetry of the FPJ flow will need to be introduced. Other than the imposed asymmetry, the geometric parameters of the FPJ nozzle and the Reynolds number of the inflow are also expected to influence the mode switching time of the FPJ flow.

8.2.5 Study of the mode switching process (from the PJ to the AJ modes)

Three methods to trigger the FPJ flow to switch from the AJ to the PJ modes were assessed in Chapter 7, namely imposing random perturbations to the inflow, imposing tangential velocity component to the inflow and adopting an asymmetric initial flow field. It was indicated in the work of Nathan et al. (1998) that the mode switching is intermittent, however the switching process of the flow from the PJ to the AJ modes has not been investigated in the current work, which is of fundamental significance to the mechanism of the bi-stable FPJ flow. Hence a possible future work can be conducted on the assessment of the methods to trigger the FPJ flow to switch from the PJ to the AJ modes and the change of the flow structure during this process.

8.2.6 Modelling a reacting FPJ flow

While a number of experimental data, in both the non-reacting and reacting condition, is available from the author's group, the current study considers only simulations of non-reacting FPJ flow. Further research can be conducted on the simulation of a reacting FPJ flow, provided that reasonable agreement against the measured results is achieved in predicting the scalar field of the jet.

References

Abbas, T., Costen, P., Lockwood, F. & Romo-Millares, C. (1993), 'The effect of particle size on no formation in a large-scale pulverized coal-fired laboratory furnace: measurements and modeling', *Combustion and Flame* **93**(3), 316–326.

Abe, K.-i. & Ohtsuka, T. (2010), 'An investigation of LES and Hybrid LES/RANS models for predicting 3-D diffuser flow', *International Journal of Heat and Fluid Flow* **31**(5), 833–844.

ANSYS Academic Research (2015), Release 16.1. Help System, ANSYS CFX-Slover Theory Guide, ANSYS, Inc.

Bearman, P. & Wadcock, A. (1973), 'The interaction between a pair of circular cylinders normal to a stream', *Journal of Fluid Mechanics* **61**(03), 499–511.

Becker, H., Hottel, H. & Williams, G. (1967), 'The nozzle-fluid concentration field of the round, turbulent, free jet', *Journal of Fluid Mechanics* **30**(02), 285–303.

Bosch, G. & Rodi, W. (1998), 'Simulation of vortex shedding past a square cylinder with different turbulence models', *International journal for numerical methods in fluids* **28**(4), 601–616.

Cafiero, G., Ceglia, G., Discetti, S., Ianiro, A., Astarita, T. & Cardone, G. (2014), 'On the three-dimensional precessing jet flow past a sudden expansion', *Experiments in Fluids* **55**(2), 1–13.

Ceglia, G., Cafiero, G. & Astarita, T. (2017), 'Experimental investigation on the three-dimensional organization of the flow structures in precessing jets by tomographic piv', *Experimental Thermal and Fluid Science* **89**(Supplement C), 166–180.
URL: *http://www.sciencedirect.com/science/article/pii/S0894177717302364*

Cheng, L., Dianat, M., Spencer, A. & McGuirk, J. J. (2012), 'Validation of les predictions of scalar mixing in high-swirl fuel injector flows', *Flow, turbulence and combustion* **88**(1-2), 143–168.

Chigier, N. A. (1981), *Energy, combustion, and environment*, McGraw-Hill College.

Dunham, D., Spencer, A., McGuirk, J. J. & Dianat, M. (2009), 'Comparison of unsteady

reynolds averaged navier-stokes and large eddy simulation computational fluid dynamics methodologies for air swirl fuel injectors', *Journal of Engineering for Gas Turbines and Power-Transactions of the Asme* **131**(1).

URL: *¡Go to ISI¿://WOS:000265841100005*

Eaton, A. M., Smoot, L. D., Hill, S. C. & Eatough, C. N. (1999), 'Components, formulations, solutions, evaluation, and application of comprehensive combustion models', *Progress in Energy and Combustion Science* **25**(4), 387–436.

URL: *http://www.sciencedirect.com/science/article/pii/S0360128599000088*

El-Behery, S. M. & Hamed, M. H. (2011), 'A comparative study of turbulence models performance for separating flow in a planar asymmetric diffuser', *Computers & Fluids* **44**(1), 248–257.

URL: *http://www.sciencedirect.com/science/article/pii/S0045793011000168*

England, G., Kalt, P. A. M., Nathan, G. J. & Kelso, R. M. (2010), 'The effect of density ratio on the near field of a naturally occurring oscillating jet', *Experiments in Fluids* **48**(1), 69–80.

Escue, A. & Cui, J. (2010), 'Comparison of turbulence models in simulating swirling pipe flows', *Applied Mathematical Modelling* **34**(10), 2840–2849.

URL: *http://www.sciencedirect.com/science/article/pii/S0307904X09004259*

FCT Combustion Pty. Ltd (2016), 'Gyro-therm kiln burner MKII', http://fctcombustion.com/products/burners/gyro-therm/. Accessed: 29-08-2016.

Frischer, T., Studnicka, M., GARTNER, C., Tauber, E., Horak, F., Veiter, A., Spengler, J., Kuhr, J. & Urbanek, R. (1999), 'Lung function growth and ambient ozone: a three-year population study in school children', *American journal of respiratory and critical care medicine* **160**(2), 390–396.

Guo, B., Langrish, T. A. G. & Fletcher, D. F. (2002), 'Cfd simulation of precession in sudden pipe expansion flows with low inlet swirl', *Applied Mathematical Modelling* **26**(1), 1–15.

Guo, B., Langrish, T. & Fletcher, D. (2001), 'Numerical simulation of unsteady turbulent flow in axisymmetric sudden expansions', *ASME J. Fluids Eng.* **123**, 574.

Gupta, A. & Kumar, R. (2007), 'Three-dimensional turbulent swirling flow in a cylinder: Experiments and computations', *International Journal of Heat and Fluid Flow* **28**(2), 249–261.

Heathcote, S. & Gursul, I. (2007), 'Jet switching phenomenon for a periodically plunging airfoil', *Physics of Fluids* **19**(2), 027104.
URL: *http://scitation.aip.org/content/aip/journal/pof2/19/2/10.1063/1.2565347*

Hill, S. (1992), A precessing jet from an axi-symmetric nozzle utilising an abrupt expansion, Internal report, The University of Adelaide, Department of Mechanical Engineering, Adelaide, South Australia, Australia.

Hill, S., Nathan, G. & Luxton, R. (1992), Precessing and axial flows following a sudden expansion in an axisymmetric nozzle, *in* '11th Australasian Fluid Mechanics Conference, The University of Tasmania, Hobart, Australia'.

Hill, S., Nathan, G. & Luxton, R. (1995), Precession in axisymmetric confined jets, *in* '12th Australiasian Fluid Mechanics Conference', p. 135138.

Houghton, J. (1996), *Climate change 1995: the science of climate change*, Vol. 19390, Cambridge Univ Pr.

Hussain, A. K. M. F. & Reynolds, W. C. (1970), 'The mechanics of an organized wave in turbulent shear flow', *Journal of Fluid Mechanics* **41**(02), 241–258.

Jakirlić, S., Kadavelil, G., Kornhaas, M., Schäfer, M., Sternel, D. & Tropea, C. (2010), 'Numerical and physical aspects in les and hybrid les/rans of turbulent flow separation in a 3-d diffuser', *International Journal of Heat and Fluid Flow* **31**(5), 820–832.

Jenkins, B., Nathan, G. & Manias, C. (1995), Modelling of precessing burners and their application to rotary alumina kilns, *in* 'Proceedings of the Third International Conference on Combustion Technologies for a Clean Environment, Centro Cultural de Balem, Lisbon, Portugal', pp. 45–53.

Jhun, I., Coull, B. A., Zanobetti, A. & Koutrakis, P. (2015), 'The impact of nitrogen oxides concentration decreases on ozone trends in the usa', *Air Quality, Atmosphere & Health* **8**(3), 283–292.

Jones, K., Dohring, C. & Platzer, M. (1998), 'Experimental and computational investigation of the knoller-betz effect', *AIAA journal* **36**(7), 1240–1246.

Kelso, R. (2001), A mechanism for jet precession in axisymmetric sudden expansions, *in* '14th Australasian Fluid Mechanics Conference', p. 829832.

Kelso, R. M., Lim, T. & Perry, A. (1996), 'An experimental study of round jets in cross-flow', *Journal of fluid mechanics* **306**, 111–144.

Kelso, R. & Smits, A. (1995), 'Horseshoe vortex systems resulting from the interaction between a laminar boundary layer and a transverse jet', *Physics of Fluids (1994-present)* **7**(1), 153–158.

Kim, H. (1988), 'Investigation of the flow between a pair of circular cylinders in the flopping regime', *Journal of Fluid Mechanics* **196**, 431–448.

Lavigne, E., Villeneuve, P. J. & Cakmak, S. (2012), 'Air pollution and emergency department visits for asthma in windsor, canada', *Canadian Journal of Public Health/Revue Canadienne de Sante'e Publique* pp. 4–8.

Lee, S. (2009), Study of a naturally oscillating triangular-jet flow, Thesis.

Lee, S. K. & Lanspeary, P. V. (n.d.), On flow structure in an oscillating-triangular-jet nozzle: Conditionally-averaged wall pressure, *in* '16th Australasian Fluid Mechanics Conference (AFMC)', School of Engineering, The University of Queensland, pp. 451–455.

Löhner, R. (2008), *Applied computational fluid dynamics techniques: an introduction based on finite element methods*, John Wiley & Sons, Hoboken, NJ, book section 1, p. 1.

Luxton, R. & Nathan, G. (1988), 'Mixing of fluids'. Australian Patent Office (Patent Application No. 16235/88, International Patent Application No. PCT/AU88/00114).

Luxton, R., Nathan, G. & Ltd., L. P. (1991), 'Controlling the motion of a fluid jet'. USA Letters Patent, No. 5,060,867.

Mahbub Alam, M., Moriya, M. & Sakamoto, H. (2003), 'Aerodynamic characteristics of two side-by-side circular cylinders and application of wavelet analysis on the switching phenomenon', *Journal of Fluids and Structures* **18**(34), 325–346.
URL: *http://www.sciencedirect.com/science/article/pii/S0889974603001075*

Manias, C., Balendra, A. & Retallack, D. (1996), 'New combustion technology for lime production', *World cement* **27**(12), 34–39.

Manias, C. G. & Nathan, G. J. (1993), 'The precessing jet gas burner: a low nox burner providing process efficiency and product quality improvements', *World Cement* **24**(3), 4–11.

Manias, C. G. & Nathan, G. J. (1994), 'Low nox clinker production', *World Cement* **25**(5), 54–56.

Menter, F. (1996), 'A comparison of some recent eddy-viscosity turbulence models', *Journal of Fluids Engineering* **118**(3), 514–519.

Menter, F., Kuntz, M. & Langtry, R. (2003), 'Ten years of industrial experience with the sst turbulence model', *Turbulence, Heat and Mass Transfer* **4**, 625–632.

Menter, F. R. (1992), 'Performance of popular turbulence model for attached and separated adverse pressure gradient flows', *AIAA Journal* **30**(8), 2066–2072.

Mi, J. & Nathan, G. (2000), Precession strouhal numbers of a self-excited precessing jet, *in* 'Proceedings of Symposium on Energy Engineering in the 21st Century, Hong Kong', pp. 1609–1614.

Mi, J., Nathan, G. & Hill, S. (1999), Frequency characteristics of a self-excited precessing jet nozzle, *in* 'Eighth Asian Congress of Fluid Mechanics', Asian Fluid Mechanics Committee, International Academic Publishers, p. 755758.

Morel, T. (1975), 'Comprehensive design of axisymmetric wind tunnel contractions', *Journal of Fluids Engineering* **97**(2), 225–233.

Morse, A. (1977), Axisymmetric turbulent shear flows with and without swirl, Thesis.

Nagano, Y. & Itazu, Y. (1997), 'Renormalization group theory for turbulence: Assessment of the yakhot-orszag-smith theory', *Fluid Dynamics Research* **20**(1), 157–172.

Nathan, G. (1988), The enhanced mixing burner, Thesis.

Nathan, G. J., Hill, S. J. & Luxton, R. E. (1998), 'An axisymmetric fluidicnozzle to generate jet precession', *Journal of Fluid Mechanics* **370**(1), 347–380.

Nathan, G. J., Mi, J., Alwahabi, Z. T., Newbold, G. J. R. & Nobes, D. S. (2006), 'Impacts of a jet's exit flow pattern on mixing and combustion performance', *Progress in Energy and Combustion Science* **32**(5-6), 496–538.

URL: *http://www.sciencedirect.com/science/article/pii/S0360128506000323*

Nathan, G. & Luxton, R. (1992*a*), The flow field within an axi-symmetric nozzle utilising a large abrupt expansion, *in* 'International Conference on Experimental Fluid Mechanics (1st: 1991: Chengdu, China)'.

Nathan, G. & Luxton, R. (1992*b*), 'Mixing enhancement by a self-exciting, asymmetric precessing flow-field', *In Transport Phenomena in Heat and Mass Transfer* . (ed. J. A. Reizes), vol. 2, pp. 1297-1307. Elsevier.

Nathan, G., Luxton, R., Balendra, S., Williams, G. & Manias, C. (1990), A preliminary assessment of the enhanced mixing burner in a cement kiln. Internal Report, The University of Adelaide, Department of Mechanical Engineering and Adelaide Brighton Cement Ltd.

Nathan, G., Nobes, D., Mi, J., Schneider, G., Newbold, G., Alwahabi, Z., Luxton, R. & King, K. (1997), 'Exploring the relationship between mixing, radiation and nox emissions from natural gas flames'.

Nathan, G. & Rapson, D. (1995), Simulataneous optimisation of heat transfer profile and nox emissions in a cement kiln, *in* 'The Australian Symposium on Combustion', The Combustion Institute (Australia).

Newbold, G. (1998), *Mixing and combustion in precessing jet flows*, University of Adelaide, Department of Mechanical Engineering.

Nobes, D. S. (1997), The generation of large-scale structures by jet precession, Thesis.

Orfanoudakis, N., Hatziapostolou, A., Krallis, K., Mastorakos, E., Sardi, K., Pavlou, D. & Vlachakis, N. (2005), 'Design, evaluation measurements and modelling of a small swirl stabilised laboratory burner', *IFRF Web Journal* (200510).

Parham, J. (2000), Control and optimisation of mixing and combustion from a precessing jet nozzle, Thesis.

Parham, J., Nathan, G., Hill, S. & Mullinger, P. (2005), 'A modified thring-newby scaling criterion for confined, rapidly spreading and unsteady jets', *Combustion science and technology* **177**(8), 1421–1447.

Perry, A. & Chong, M. (1987), 'A description of eddying motions and flow patterns using critical-point concepts', *Annual Review of Fluid Mechanics* **19**(1), 125–155.

Perry, A. & Chong, M. (1993), *Topology of flow patterns in vortex motions and turbulence*, Springer, pp. 339–361.

Perry, A. & Hornung, H. (1984), 'Some aspects of three-dimensional separation. ii-vortex skeletons', *Zeitschrift fur Flugwissenschaften und Weltraumforschung* **8**, 155–160.

Perry, A., Lim, T. & Chong, M. (1980), 'The instantaneous velocity fields of coherent structures in coflowing jets and wakes', *Journal of fluid Mechanics* **101**(02), 243–256.

Pope, S. (1978), 'An explanation of the turbulent round-jet/plane-jet anomaly', *AIAA Journal* **16**(3), 279–281.

Pride, K. R., Peel, J. L., Robinson, B. F., Busacker, A., Grandpre, J., Bisgard, K. M., Yip, F. Y. & Murphy, T. D. (2015), 'Association of short-term exposure to ground-level ozone and respiratory outpatient clinic visits in a rural location sublette county, wyoming, 20082011', *Environmental Research* **137**, 1–7.

URL: *http://www.sciencedirect.com/science/article/pii/S0013935114003971*

Ruprecht, A., Helmrich, T. & Buntic, I. (2004), Very large eddy simulation for the prediction of unsteady vortex motion, *in* 'Modelling Fluid Flow', Springer, pp. 229–246.

Schultz, M. G., Akimoto, H., Bottenheim, J., Buchmann, B., Galbally, I. E., Gilge, S., Helmig, D., Koide, H., Lewis, A. C. & Novelli, P. C. (2015), 'The global atmosphere watch reactive gases measurement network', *Elementa: Science of the Anthropocene* **3**(1), 000067.

Shur, M. L., Strelets, M. K., Travin, A. K. & Spalart, P. R. (2000), 'Turbulence modeling in rotating and curved channels: Assessing the spalart-shur correction', *AIAA Journal* **38**(5), 784–792.

Smagorinsky, J. (1963), 'General circulation experiments with the primitive equations: I. the basic experiment*', *Monthly weather review* **91**(3), 99–164.

Smirnov, P. E. & Menter, F. R. (2009), 'Sensitization of the sst turbulence model to rotation and curvature by applying the spalartshur correction term', *Journal of Turbomachinery* **131**(4), 041010–041010. 10.1115/1.3070573.

Smith, E., Nathan, G. & Dally, B. (2003), Range of validity of a modified k-epsilon model of the non-reacting flow from a precessing jet nozzle, *in* 'Third International Conference on CFD in the Minerals and process industries'.

Teodorovich, E. (1994), 'On the yakhotorszag theory of turbulence', *Fluid dynamics* **29**(6), 770–779.

Tian, Z. F., Tu, J. Y., Yeoh, G. H. & Yuen, R. K. K. (2007), 'Numerical studies of indoor airflow and particle dispersion by large eddy simulation', *Building and Environment* **42**(10), 3483–3492.

URL: *http://www.sciencedirect.com/science/article/pii/S0360132306003829*

Tian, Z. F., Witt, P. J., Yang, W. & Schwarz, M. P. (2011), 'Numerical simulation and validation of gas-particle rectangular jets in crossflow', *Computers & Chemical Engineering* **35**(4), 595–605.

Tkatchenko, I., Kornev, N., Jahnke, S., Steffen, G. & Hassel, E. (2007), 'Performances of les and rans models for simulation of complex flows in a coaxial jet mixer', *Flow, Turbulence and Combustion* **78**(2), 111–127.

Townsend, A. R. & Howarth, R. W. (2010), 'Fixing the global nitrogen problem', *Scientific*

American **302**(2), 64–71.

Tu, J., Yeoh, G. H. & Liu, C. (2008), *Computational fluid dynamics: a practical approach*, Butterworth-Heinemann, Boston, book section 1, p. 2.

UNEP & WHO (2011), Integrated assessment of black carbon and tropospheric ozone, Report, Nairobi.

US EPA (1999), Nitrogen oxides, why and how they are controlled, Report, Research Triangle Park, NC.

US EPA (2010), Our nation's air: status and trends through 2008, Report, Research Triangle Park, NC.

Versteeg, H. & Malalasekera, W. (2007), *An introduction to computational fluid dynamics: the finite volume method*, Prentice Hall.

Videgar, R. (1997), 'Gyro-therm technology solves burner problems: The application of new gyro-therm burner technology in the durkee plant', *World Cement* **28**, 39–45.

Wang, X. H. & Wu, F. (1993), 'One modification to the yakhot-orszag calculation in the renormalization-group theory of turbulence', *Physical Review E* **48**(1), R37.

Wegner, B., Maltsev, A., Schneider, C., Sadiki, A., Dreizler, A. & Janicka, J. (2004), 'Assessment of unsteady rans in predicting swirl flow instability based on les and experiments', *International Journal of Heat and Fluid Flow* **25**(3), 528–536.
URL: *http://www.sciencedirect.com/science/article/pii/S0142727X04000268*

Wespes, C., Hurtmans, D., Emmons, L. K., Safieddine, S., Clerbaux, C., Edwards, D. P. & Coheur, P.-F. (2016), 'Ozone variability in the troposphere and the stratosphere from the first 6 years of iasi observations (20082013)', *Atmospheric Chemistry and Physics* **16**(9), 5721–5743.

WHO (2006), Who air quality guidelines for particulate matter, ozone, nitrogen dioxide and sulfur dioxide, Report, Geneva.

Wong, C., Nathan, G. & Kelso, R. (2008), 'The naturally oscillating flow emerging from a fluidic precessing jet nozzle', *Journal of Fluid Mechanics* **606**(1), 153–188.

Wong, C. Y. (2004), The flow within and in the near external field of a fluidic precessing jet nozzle, Thesis.

Wong, C. Y., Lanspeary, P. V., Nathan, G. J., Kelso, R. M. & O'Doherty, T. (2003), 'Phase-averaged velocity in a fluidic precessing jet nozzle and in its near external field', *Experi-*

mental Thermal and Fluid Science **27**(5), 515–524.

Wong, C. Y., Nathan, G. J. & O'Doherty, T. (2004), 'The effect of initial conditions on the exit flow from a fluidic precessing jet nozzle', *Experiments in Fluids* **36**(1), 70–81.

Xu, M., Mi, J. & Li, P. (2011), 'Large eddy simulation of an initially-confined triangular oscillating jet', *Flow, Turbulence and Combustion* pp. 1–20.

Appendix A

Publications arising from this thesis

Chen, X., Tian, Z.F. and Nathan, G.J. (2012). Numerical simulation of the flow within a fluidic precessing jet nozzle. In P.A. Brandner and B.W. Pearch (Eds.) *Proceedings of the 18th Australasian Fluid Mechanics Conference,* Launceston, Australia, 3-7 December, 2012. (4 pages)

Effect of turbulent Schmidt number on the scalar field simulation of a fluidic precessing jet flow

†Xiao Chen, *Zhao Feng Tian and Graham 'Gus' Nathan

[1]Center for Energy Technology,
The School of Mechanical Engineering
The University of Adelaide, Adelaide, SA 5005, Australia

*Presenting author, † Corresponding author: xiao.chen01@adelaide.edu.au

Abstract

A preliminary numerical study of the external scalar field of a fluidic precessing jet (FPJ) flow is reported. The unsteady Shear Stress Transport (SST) model, which showed generally good agreement with the measured velocity field of flows within a FPJ nozzle, despite some discrepancies, was adopted to assess the effect of the turbulent Schmidt number, Sc_t, on the simulated scalar field. The simulated jet axis concentrations with three turbulent Schmidt number values, Sc_t =0.5, 0.9 and 1.3 have been compared with the measured results in the literature. It is found that the SST model over-predicts the centreline concentration of the jet in the near field downstream from the exit of the FPJ nozzle, while under-predicts it in the far field. An increase in Sc_t number causes the simulated jet to be more distributed away from the axis of the confinement, which is in contrast to the measured data. The best agreement with the measured result was achieved by adopting a Sc_t number of 0.5. However, due to the complexity of the FPJ flow, it is not feasible for a two-equation URANS model to reliably reproduce the scalar field by simply adjusting the turbulent Schmidt number.

Keywords: scalar mixing, turbulent Schmidt number, CFD, URANS

Introduction

A fluidic precessing jet (FPJ) nozzle, which has been employed in industrial rotary kilns was proposed by Nathan [1] to generate the FPJ flow. Numerous previous investigations of the flows within the FPJ nozzle have conducted by experimental measurements [2, 3], analytical method [4] and recently computational fluid dynamics (CFD) [5, 6]. Compared with the many studies of flows within the FPJ nozzle, the study of scalar mixing downstream the FPJ nozzle is much less. Parham [7] and Parham et al. [8] measured the scalar field downstream the FPJ nozzle using a two colour planar laser-induced fluorescence technique. In these studies, the effects of co-flow, confinement and a shaping jet on the mixing characteristics are investigated. Nevertheless, a reliable CFD model of the scalar field downstream the FPJ nozzle is still lacking. Hence the main objective of this paper is to preliminarily assess the feasibility of the unsteady Reynolds-Averaged Navier-Stokes (URANS) turbulence model in predicting the scalar field of the FPJ flow.

In the previous CFD studies of the flows within the FPJ nozzle [5, 6] conducted in the authors' group, the authors have assessed the performance of the Shear Stress Transport (SST) model in modeling the turbulent flows within the FPJ nozzle. The SST model achieves reasonable agreement with the measured mean axial velocity profiles for pipe and contraction inlets [6], and the measured centerline velocity decay and equivalent diameters of the phase-averaged precessing jet for the contraction inlet case despite some discrepancies [5]. Therefore the current CFD model of the scalar field downstream the FPJ nozzle is based on the SST model.

When applying the URANS models for the scalar field simulation, the turbulent Schmidt number (Sc_t), which is defined as the ratio of the turbulent eddy viscosity (μ_t) and the turbulent diffusivity (Γ_t), was found to have great influence on the simulated turbulent mixing [9]. In a numerical simulation of a jet in a cross-flow simulated with the standard k-ε model [10], the range of the turbulent Schmidt number, from 0.5 to 0.9, was found to have slight influence on the simulated temperature field. In another study of temperature field in a cross-flow [11], it was also found that the simulated temperature distribution is not sensitive to the turbulent Schmidt number. However, it is found that the turbulent Schmidt number has a significant influence on the simulated scalar mixing and Sc_t =0.2 is recommended for the simulation of a jet in a cross-flow [11]. Nevertheless, how the turbulent Schmidt number will influence the simulated scalar mixing of a FPJ flow is unclear.

The main aim of the current paper is to assess the effect of turbulent Schmidt number on the simulated scalar field in a flow downstream a FPJ nozzle. The FPJ flow investigated in [7, 8] are simulated using the SST model. The simulated jet concentration based on the turbulent Schmidt number, Sc_t =0.9, is compared with measured values reported in [7]. The default value of the turbulent Schmidt number is normally set as 0.9 (e.g. in ANSYS/CFX and ANSYS/FLUENT). A lower Sc_t number of 0.5 is tested in the current study following the work [10], and a larger Sc_t number of 1.3 is also tested.

Numerical Model

ANSYS/Designmodeler 16.5 was used to generate the 3-dimensional CFD geometry. Figure 1 illustrates geometric configuration of the CFD domain that includes an FPJ nozzle with a contraction inlet and a confinement. This geometry is identical to the configuration in the experimental studies [7]. The confinement is a cylindrical domain which has a diameter of 390 mm and a length of 1100 mm. The FPJ nozzle has a length of 115 mm from the main flow inlet to the exit of the contraction and 110 mm from the contraction exit to the nozzle exit. The inner diameter of the FPJ nozzle is 38 mm and the diameter of the center body is 27 mm. More details of the FPD nozzle can be found in the literature [7].

Figure 2 presents the details of the CFD mesh that was generated with the software ANSYS/ICEM CFD 16.5. The O-grid method was adopted to generate the structured mesh to

ensure the mesh quality, especially in the near wall region, which makes the y+ values to be less than 1. A mesh independent test has been conducted and a final mesh of 8.6 million nodes is used for the study.

The CFD software ANSYS/CFX 16.5 was adopted for the simulations. The flow of the CFD model is a multiple component fluid that includes two fluids. Water at 25 °C was employed as the first fluid (fluid1). A second fluid (termed as fluid2 in the model) is used for the co-flow, while its properties are exactly the same as those of the fluid1 at the main inlet. This numerical approach matches the experiment [7,8] in which the jet fluid was water marked with a fluorescent dye. The dye in the experiment is with very low concentration and its effects on the water dynamic properties can be neglected. At the main flow inlet (see Figure 1b), mass fraction of fluid1 is 1, i.e. the mass fraction of fluid2 is 0. At the co-flow inlet, mass fraction of fluid1 is 0 and the mass fraction of fluid2 is 1.

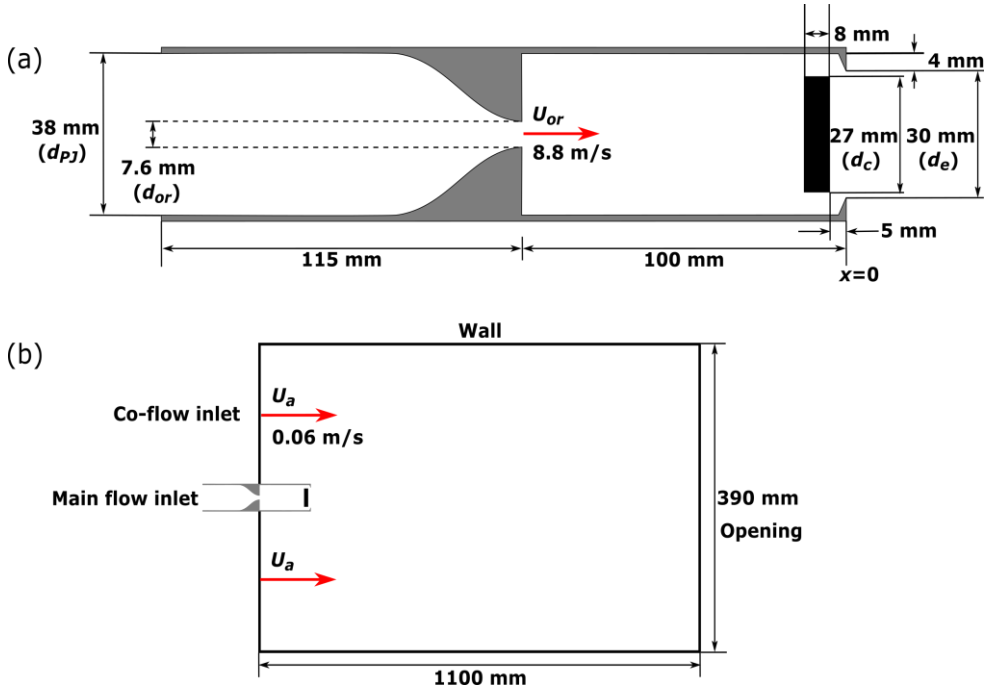

Figure 1: The geometric configurations of (a) the FPJ nozzle and (b) the whole fluid domain. Here d_{PJ}, d_{or}, U_{or} and U_a are the diameter of the nozzle, diameter of the inlet orifice, the inlet velocity at the orifice and the co-flow velocity, respectively.

For multi-component gases, the continuity equation and momentum equation after Reynolds averaging [12] are given as below:

$$\nabla \cdot U = 0 \tag{1}$$

$$\frac{\partial(\rho U)}{\partial t} + \nabla \cdot (\rho UU) = -\nabla p + \nabla \cdot \left\{ \mu \left[\nabla U + (\nabla U)^T \right] - \rho \overline{UU} \right\} + S_M \tag{2}$$

here U is the mean velocity vector, P the mean pressure, S_M the external momentum source, and ρ the mixture density that is calculated as:

$$\rho = \sum_{I=1}^{Nc} Y_I \rho_I \tag{3}$$

where ρ_I is the density of the component I. *Nc* is the number of modelled species in the mixture, and Y_I is the mass fraction of the species I that is solved by the following equation:

$$\frac{\partial(\rho Y_I)}{\partial t} + \nabla \cdot (\rho U Y_I) = \nabla \cdot (\Gamma_{I.eff} \nabla Y_I) + S_I \quad (4)$$

here S_I is the source term of the species. The effective diffusion coefficient of species I, $\Gamma_{I.eff}$, in Equation 4 is calculated as [12]:

$$\Gamma_{I.eff} = \Gamma_I + \frac{\mu_t}{Sc_t}, \quad (5)$$

Where Γ_I is the molecular diffusion coefficient of species, $\Gamma_I = \rho_I D_I$, D_I the kinematic diffusivity of the species I, μ_t the turbulent viscosity.

The root mean square (r.m.s) residuals are all under 5 x 10^{-5}. The high resolution scheme and the second order backward Euler scheme were adopted for the advective and transient terms, respectively.

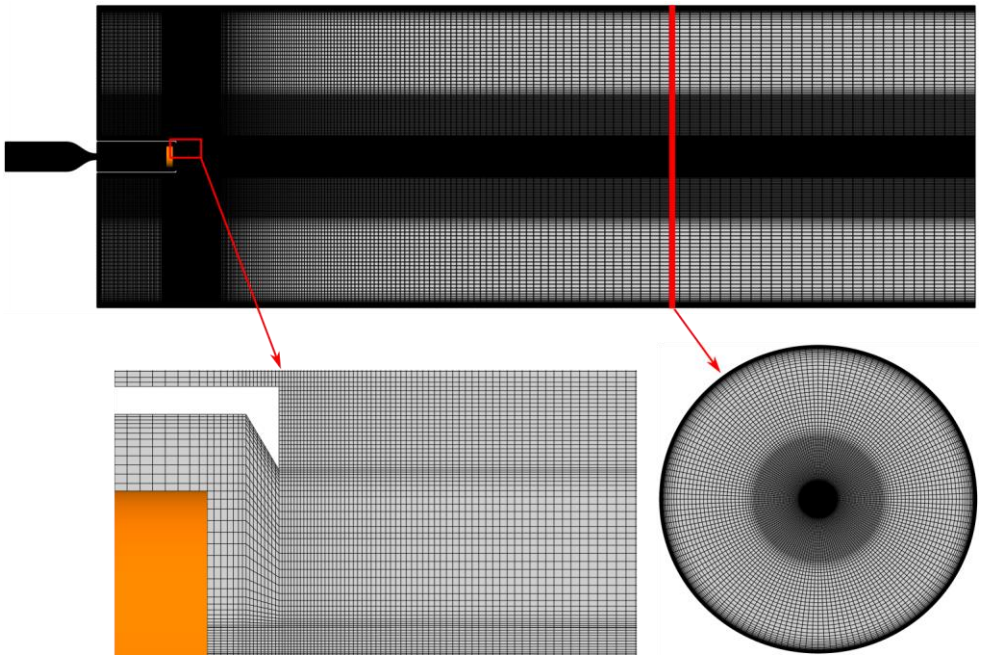

Figure 2: Mesh of the CFD model.

Preliminary Results and Discussion

Figure 3 compares the measured [7] and simulated instantaneous concentration of the jet on a cross-sectional plane downstream the nozzle exit with the Sc_t value of 0.5, 0.9 and 1.3, respectively. It can be seen that the small eddies and scalar concentration fluctuation in the measured instantaneous flow have not been reproduced with any of the three URANS approaches. The three simulated deflected angles between the instantaneous jets and the nozzle axis (indicated as the dashed lines) are similar, although they all appear to be larger than the measured data. It is observed that the value of Sc_t does not have a significant influence on the simulated flows within the FPJ nozzle. This observation can be explained by reviewing equations 1-4 and the inlet conditions in the flow. The turbulent Schmidt number is

only incorporated in Equations 4, which describes the transport of mass fraction of species. That is, it influences only the mixture density (Equation 3) and then the mixture flow field (Equations 1 and 2). If there is no mixing process, i.e. the mass fraction of a species is 1, the change of Sc_t will effect neither the mixture density nor the mixture species field. In the current case, the mass fraction of fluid1 is 1 at the main flow inlet and is nearly 1 anywhere inside the FPJ nozzle, except in a small region near to the nozzle exit where the mixture in the emerging field can be entrained into the FPJ nozzle. Nevertheless, as shown in Figure 4, the mass fraction of the mixture entrained into the FPJ nozzle exit region is very small and can be neglected.

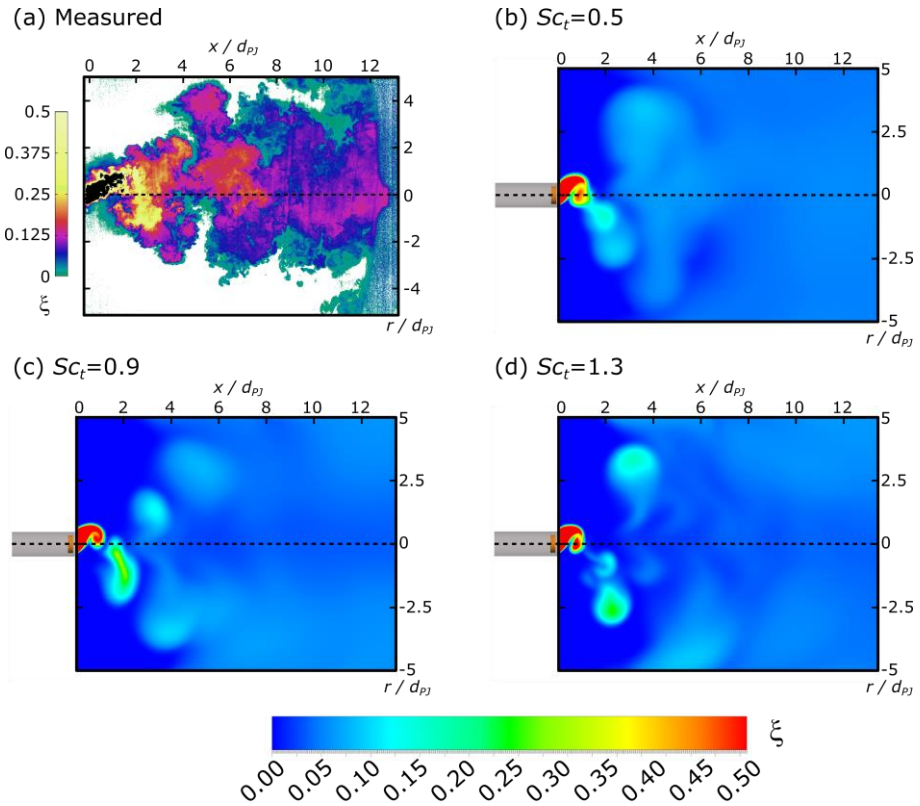

Figure 3: Instantaneous concentration cross-sectional contours of the FPJ flows that were (a) measured [7] and simulated using the SST model with the Sc_t value of (b) 0.5, (c) 0.9 and (d) 1.3.

The effect of the turbulent Sc_t number on the mixing process within the external flow is more pronounced than within the chamber, as is shown in Figure 3b-d. It can be seen that when the turbulent Sc_t number increases from 0.5 to 1.3, the diffusion of the fluid1 in the external flow decreases, leading to higher conentration of fluid1 in some flow vortexes. This can be explained by looking at Equation 5, when the turbulent Sc_t number increases, the effective diffusion coefficient of species I decreases, leading to lower diffusion of fluid1 as shown in Equation 4.

Figure 5 compares the measured [7] and simulated centreline concentration with three turbulent Schmidt numbers, namely, Sc_t = 0.5, 0.9 and 1.3. The measured centerline concentration of the jet exhibits a fast decay in the region from the FPJ exit (x/d_{PJ}=0) to an

"elbow point" (x/d_{PJ}≈1.4). At the "elbow point", the decay rate suddenly decreases and is nearly constant downstream from that point. This trend has been simulated with all the three models, however, the distance between the "elbow point" and the nozzle exit is over-predicted. For all CFD cases, the centreline jet concentration is over-predicted in the emerging field (say x/d_{PJ}<0.5) and is under-predicted in the region downstream from about x/d_{PJ}=1, especially in the region near to the "elbow point".

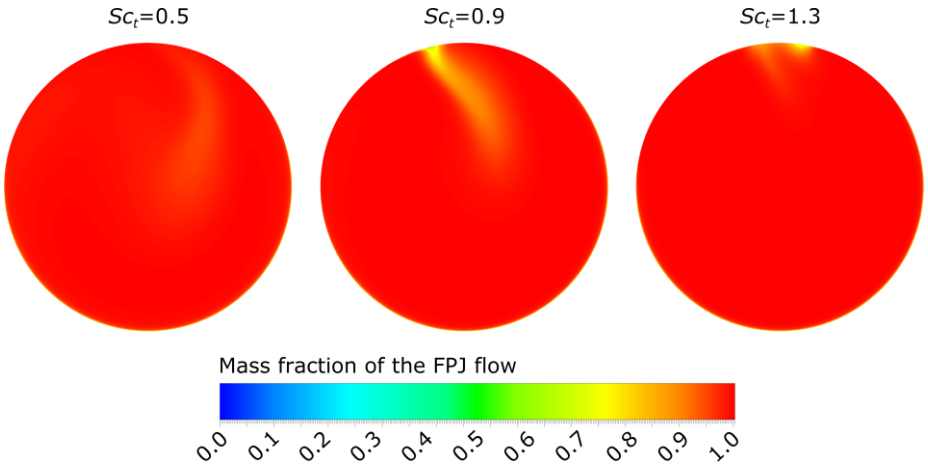

Figure 4: Instantaneous concentration contours of the Fluid1 on the nozzle exit (x=0) that were simulated using the SST model with the Sc_t value of 0.5, 0.9 and 1.3.

Figure 5 also shows that a decrease in Sc_t number leads to a decrease in centreline concentration, indicating a higher simulated mixing in the near field (x/d_{PJ}<0.5). This is consistent with Equations 4 and 2 that a decrease in Sc_t number causes the effective diffusivity to increase, hence improves the simulated scalar mixing. However in the far field (x/d_{PJ}>1), model with the lowest Sc_t number (Sc_t=0.5) simulated the highest centreline jet concentration. One possible reason is that, based on the observation of the simulated instantaneous jet concentration, the jet flow was simulated to be distributed preferentially in the near wall region as the increase of Sc_t number. Although the best agreement against the measured data was achieved by adopting a turbulent Schmidt number of 0.5, this model greatly under-predicts the centreline concentration of the jet in the region near to the "elbow point" (x/d_{PJ}≈1.4). This implies that the mechanism is not one of "turbulent" diffusion, but is rather controlled by the exit angle of the emerging jet, which is a function of large scale turbulent flow features.

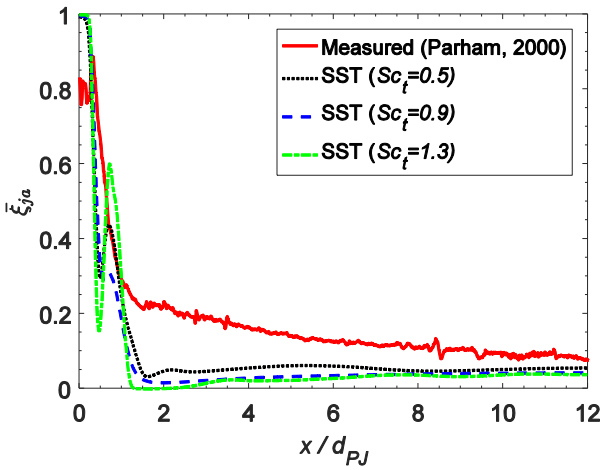

Figure 5: Measured [7] and simulated mean centerline concentration of the jet.

Summary

A decrease in Sc_t number causes the centreline concentration of the FPJ flow to decrease in the emerging field and increase in the far field. However, all the three approaches are found to over-predict the centreline concentration of the jet in the emerging field downstream the exit of the FPJ nozzle while under-predict it in the far field. This is due to large-scale features of the turbulent flow rather than to small scale "diffusion" processes, which are modelled by the turbulent Schmidt number. For this reason, the level of disagreement between the measured and predicted values of the scale field is not improved by changes to the turbulent Schmidt number. Indeed, the trends are opposite to what would be expected.

The flow in the far field of the confined, co-flowing turbulent FPJ flow is simulated to be distributed mostly in the region near to the wall of the confining cylinder, while the measured jet is preferentially distributed near to the axis. This discrepancy between the simulated and measured scalar field may be attributed to the over-predicted angle of the jet emerging from the FPJ nozzle.

Acknowledgements

The first author was supported by the Divisional Scholarship of the faculty of ECMS, the University of Adelaide. The authors gratefully acknowledge the support of the Australian Research Council through Grant DP150102230.

References

[1] Nathan, G., 1988, "The enhanced mixing burner." PhD Thesis, the University of Adelaide.
[2] Nathan, G., Hill, S., and Luxton, R., 1998, "An axisymmetric 'fluidic'nozzle to generate jet precession," Journal of Fluid Mechanics, 370, pp. 347-380.
[3] Wong, C., Lanspeary, P., Nathan, G., Kelso, R., and O'Doherty, T., 2003, "Phase-averaged velocity in a fluidic precessing jet nozzle and in its near external field," Experimental Thermal and Fluid Science, 27(5), pp. 515-524.
[4] Kelso, R., 2001, "A mechanism for jet precession in axisymmetric sudden expansions." In the Proceeding of 14th Australasian Fluid Mechanics Conference, pp. 829-832.

Appendix B

Confirmation of the hypothesised vortex region

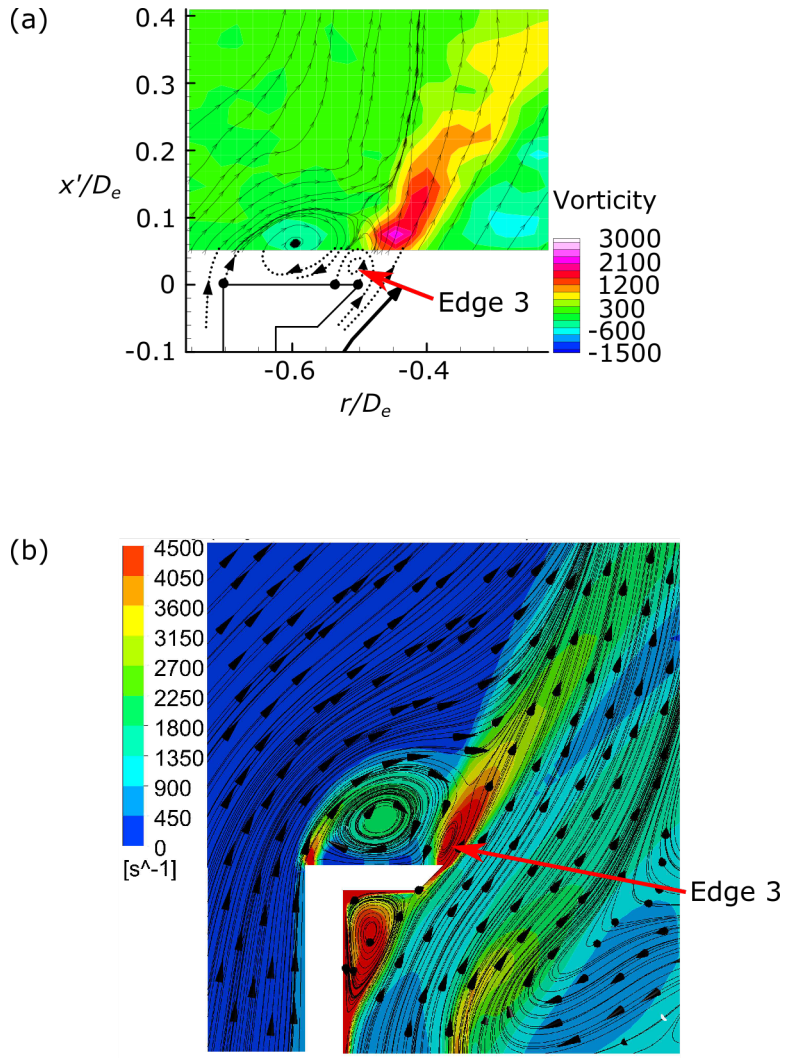

Figure B.1: Comparison of the streamline in the emerging field of the FPJ flow. (a) Hypothesised streamline based on the experimental result (Wong 2004), (b) predicted with the SST model.